



**SELECTIVELY TUNING A BUCKLED SI/SIO₂ MEMBRANE MEMS
THROUGH JOULE HEATING ACTUATION AND MECHANICAL
RESTRICTION**

THESIS

Kyle K. Ziegler, Second Lieutenant, USAF

AFIT-ENG-14-M-88

**DEPARTMENT OF THE AIR FORCE
AIR UNIVERSITY**

AIR FORCE INSTITUTE OF TECHNOLOGY

Wright-Patterson Air Force Base, Ohio

DISTRIBUTION STATEMENT A:
APPROVED FOR PUBLIC RELEASE; DISTRIBUTION UNLIMITED.

The views expressed in this thesis are those of the author and do not reflect the official policy or position of the United States Air Force, Department of Defense, or the United States Government.

This material is declared a work of the U.S. Government and is not subject to copyright protection in the United States.

AFIT-ENG-14-M-88

SELECTIVELY TUNING A BUCKLED SI/SIO₂ MEMBRANE MEMS THROUGH
JOULE HEATING ACTUATION AND MECHANICAL RESTRICTION

THESIS

Presented to the Faculty

Department of Electrical and Computer Engineering

Graduate School of Engineering and Management

Air Force Institute of Technology

Air University

Air Education and Training Command

In Partial Fulfillment of the Requirements for the
Degree of Master of Science in Electrical Engineering

Kyle K. Ziegler, BSME

Second Lieutenant, USAF

March 2014

DISTRIBUTION STATEMENT A:
APPROVED FOR PUBLIC RELEASE; DISTRIBUTION UNLIMITED.

Abstract

Springs are a widely utilized component in the Microelectromechanical systems (MEMS) industry, especially in inertial devices. Many of these devices rely on the restoring forces of springs to return the device, such as in an accelerometer, to equilibrium. By adding external springs with negative spring constant behavior, the total spring constant can be modified. Previous work at AFIT investigated the spring characteristics of a buckled MEMS Si/SiO₂ membrane. This research expanded on previous work and attempted to modify the spring in two ways. First, a Ti/Au meander resistor was deposited atop the membrane in an effort to actuate the membrane and change the spring constant. Secondly, a series of overhanging cantilevers were attached to the bulk substrate surrounding the membrane in an effort to restrict the membrane deflection to the negative stiffness region. Membrane buckling was investigated through Finite Element analysis (FEA) and analytical equations. Deflections were measured using an interferometric microscope (IFM) and force/deflection measurements were captured using a unique measurement scheme. The results concluded that by introducing a thermal stress, the membrane could be actuated with a corresponding 300% increase in spring constant. Additionally, the overhanging beams restricted the membrane deflection by up to 30%, but, because of a lack in beam stiffness, failed to restrict the membrane to the negative stiffness region.

Dedicated to the Memory of Gene and Dave...

A Great American farmer,

And a Great American Hero...

Acknowledgments

Special thanks to all the fine gentlemen in the MEMS lab. I spent 18 months with a group of excellent mentors to whom I hope to model myself after. To the “Captains Three” (B, Raj, and Carlos/Ed) for teaching me to persevere and stand strong to your beliefs when the world seems to be out to get you. To Chris, for your subtle humor, admirable work ethic, and generally good advice. To Richie for teaching me to not take things too seriously and that sometimes “meh, it’s good enough.” To Dan “the man” for hittin’ the weights with me, and being an excellent mentor. To Ryan, my roommate through this ordeal, for your support, for being in my cycling “gang,” and for the good times we shared. I also want to extend my thanks to Tristan, Kronos and TJ for their support. Finally, to my parents and brothers for molding me into the person that I am today.

I want to thank the cleanroom technicians Tom “big dawg” and Rich for their help and technical assistance, and for their extraordinary stories, in particular, the Alaskan grizzly bear that was “like 25 feet long.” Thanks to the expert technicians at AFRL, Andy, Jason, and Doug, for their superb help with my research, specifically, etching, deposition, and dicing. I also want to thank my committee members and my advisor Dr. Coutu for their help.

Most of all I want to thank my Texas girl, Karlie, your love and support motivates me and enables me to conquer any challenge. You always listen to my gripes and keep my spirits high. Without you this would not have been possible.

Kyle K. Ziegler

Table of Contents

	Page
Abstract.....	iv
Acknowledgments.....	v
List of Figures.....	x
List of Tables.....	xv
List of Equations.....	xvi
I. Introduction.....	1
Background.....	1
Justification.....	1
Problem statement.....	3
Buckled structures.....	4
Scope.....	5
Assumptions.....	6
Summary.....	7
II. Background.....	8
Introduction.....	8
Semiconductors.....	8
MEMS Overview.....	9
MEMS Fabrication.....	11
Surface micromachining.....	12
Bulk Micromachining.....	14
Hybrid Process for this Research.....	15
Residual Stress.....	15
Buckling.....	17
Bistability.....	25
Realized Applications of Bistability.....	26
Transverse Actuation and Spring Constant.....	31
Linear Regressive Spring Characteristics.....	32
Belleville Washer.....	33
Finite Element Methods Background.....	36
Heat Transfer.....	37
Heat Transfer Methods.....	37
Related Joule Heating Based Research.....	38
Summary.....	43

III. Methodology	45
Chapter Overview	45
Design	45
Resistor Design	46
Beam Design	48
Fabrication	50
Resistor Fabrication.....	51
Beam Fabrication	52
Backside Etch Process.....	54
Finite Element Methods Process.....	55
Generating an Appropriate Mesh (Mesh Convergence Study)	56
Simulating Buckling.....	57
Test Fixture for Load/Deflection Measurements	59
Experimental Methods	61
Zygo [®] Optical Surface Profilometer	61
Thermal Probe Station.....	63
Summary	65
IV. Results.....	66
Chapter Overview	66
Analytic Modeling	67
Results of Simulation Scenarios	70
Simulated Membrane Buckling.....	70
Electro-Thermal FEA.....	72
Thermal Actuation Experimental Results	77
Actuation Measurements.....	77
Force/Deflection Estimation using Measure Deflection Data.....	81
Thermal Stage Testing	83
Negative Stiffness Isolation Results.....	84
Optical imaging	84
Interferometric imaging force/deflection measurements	86
Force/deflection measurements.....	87
Summary	89
V. Analysis.....	91
Introduction	91
Model and Experimental Data Comparison.....	91
Resistor Failure During Experimentation	94
Negative Stiffness Isolation Cantilever Analysis.....	97
Summary	98
VI. Conclusions and Recommendations	99

Chapter Overview	99
Conclusions of Research	99
Significance of Research	101
Recommendations for Future Research	102
Membrane geometry and actuation speed	102
Reliable Force Testing	103
Negative Stiffness Restriction	103
Summary	103
Appendix A: Possible Applications	105
Appendix B: Mask Design	108
Appendix C: Modal Analysis	112
Appendix D: Visual Bibliography	114
Appendix E: Process Followers	115
References	119

List of Figures

Figure	Page
1. Projected growth of the MEMS industry [4].	2
2. Scanning electron microscope image (SEM) of a MEMS hinge (a) [20]. Rotary electrostatic motor (b) [21].	10
3. Surface micromachining process illustrating the formation of a cantilever beam. (a) Photoresist spin coating. (b) Photoresist exposure to desired mask pattern. (c) Film deposition. (d) Beam geometric shaping through another photolithographic process. (e) Sacrificial layer etch.	13
4. (a) Isotropic etching of silicon. (b) anisotropic etching of two different crystal oriented silicon substrates. Modified from [31].	14
5. A slender column showing buckling when exposed to an external axial load [42]. .	17
6. (a) membrane with compressive buckling stress shown. (b) cross-section of the buckled membrane with upper and lower equilibrium states (superimposed on lower plate diagram) ©IEEE 1994 [45].	18
7. The equilibrium path of the center of the membrane under an increasing load. Y-axis indicates center out-of-plane deflection. Modified from [50].	19
8. Computer generated three dimensional profile of a buckled membrane.	20
9. Total strain energy with reference to the center deflection. Multiple lines showing increased compressive loading illustrate how the distinct low energy states are formed ©IEEE 1994 [45].	24
10. The ball-on-the-hill analogy demonstrating the concept of equilibrium states [53].	25
11. Three sequential cross-sectional diagrams which illustrate the snap through phenomenon in beams and membranes © IEEE 2004 [9].	26
12. Schematic representation of the proposed nonvolatile memory cell. Features include, spacer (S), beam (B), substrate (SUB), and lateral electrodes (L) ©IEEE 1990 [55].	27
13. Bistable snapping microactuator. Bistability equilibrium position is caused by the tension band applying a compressive force to the beams, and the beams resisting the bending. The low energy state created by this effect is similar to what occurs during buckling ©IEEE 1994 [57].	29

14. Bistable microvalve actuated by resistive heating [58]. The buckled membrane is used to physically close the inlet of the valve. The resistive heater is used to actuate the membrane with heat pulses.....	29
15. Microvalve with pneumatically coupled membranes. The membrane is used to close and open the fluid valve. When one membrane is actuated downward the other will be pneumatically actuated to the upward buckled position ©IEEE 1996 [59].....	30
16. (a) A linear spring. (b) A nonlinear stiffening spring resulting from decreased length with increased deflection. (c) A nonlinear softening spring [62]......	32
17. Spring characteristics of the membrane (a). Cross-section of membrane actuation and corresponding spring stiffness (b).	33
18. Nominal load-deflection curve for a disk spring (Top). Frontal and cross sectional views of the disk spring (Bottom) [10]......	34
19. Load deflection behavior for a series of disk springs with differing displacements. Modified from [10]......	35
20. Membrane with heat generation (Q) and methods of heat transfer shown [67].	39
21. Vertical thermal plate actuator [27]......	41
22. Square style resistor. The partial box surrounding the resistor was originally used for alignment and does not influence resistor behavior.	47
23. Spiral resistor.	48
24. (a) Quad beam design. (b) Twin-beam design. The backside etch cavity and the approximate membrane shape are also illustrated for clarity. The length and width of the membrane are shown for reference.....	49
25. Analytically determined load/deflection characteristics for the Si/SiO ₂ membrane. At the initial buckling location, zero force is required since the membrane is at equilibrium. At approximately 7μm deflection, the membrane is expected to transition to the negative stiffness region.	50
26. Resistive heating element deposition process. (a) initial photoresist spin-on, (b) ultraviolet (UV) light exposure and develop, (c) gold deposition through electron beam evaporation, (d) excess gold and photoresist removal.	52
27. Fabrication sequence for the SU-8 cantilever.....	53

28. Backside etch process. (a) initial sample, (b) SU-8 photoresist deposition and patterning, (c) DRIE process, (d) instantaneous membrane buckling upon etch completion.	55
29. Four separate sized mesh models and their respective modal frequency.	56
30. Unpreturbed, non-equilibrium buckled state.	58
31. (Dashed) initial buckling with applied load to “nudge the table”, (solid) relaxed buckled state.	58
32. Test fixture with appropriate components listed. Micromanipulators are used for coarse adjustment, while the piezo actuator controls small displacements [77].	60
33. Zygo [®] user interface screen. User controls the measurement with the controls on the left. The optical image is used for fringe alignment. The profile data, 3D model, and surface profile are results from the machine.	63
34. Thermal stage user interface screen.	64
35. Strain energy of the membrane. Energy minima correspond to locations of predicted deflection.	68
36. Strain energy curves for a successive, 100K temperature increase in the membrane.	69
37. Analytically determined membrane deflection with increased temperature.	69
38. Initial membrane buckling determined by FEA.	71
39. Cross-section of the membrane with increasing temperature predicted by FEA.	72
40. Modeled membrane temperature with respect to voltage applied to the resistor.	74
41. FEM simulation results show the thermal gradient with an applied voltage of 5V. .	75
42. Simulated deflection under various applied voltages. The temperature collected from the resistor simulations was used with the deflection simulations to estimate deflection at each voltage.	76
43. Optical image of the deposited gold resistor located on top of the membrane.	78
44. Optical image of the second resistor design.	78
45. Deflection data for membrane actuation. Vertical error bars indicate one standard deviation of the sample data.	79

46. Deflection data for membrane actuation with a spiral resistor. Vertical error bars indicate one standard deviation of the sample data.	80
47. Analytically determined force/deflection behavior. The original membrane displacement is indicated on the x-axis, and the slope of the curves is directly correlated to the stiffness of the membrane.	82
48. Heating profile of the membrane with successive voltages applied to the resistor. (a)-(e) each represent 1-5V respectively.	83
49. Optical depiction of the SU-8 cantilevers immediately following the backside etching process to release the membrane.	85
50. SEM image of the fabricated device rotated to 45°. The four cantilever beams surround the post-buckled membrane. With a 1 mm edge length and a deflection close to 10 μm , the vertical deflection from buckling cannot be observed.	86
51. Interferometric image of the restricted membrane. (a) The buckling of the membrane. (b) Surface profile of the membrane indicating the buckling deflection.	87
52. Experimentally determined force/deflection curve.	88
53. Analytical modeling data, FEM data, and Experimental data.	91
54. Thermal actuation behavior of each style of resistor.	94
55. Failed resistive heater. Debris shown scattered around sample is from testing and failure of samples.	95
56. SEM image illustrating the failed portion of a resistor. The gold has been melted and fails to provide an electrical connection between the contact pads. This could be caused by excess heating and the formation of a secondary connection.	96
57. Euler Spring for vibration isolation [82].	106
58. Resistor mask, (a) original resistor design, and (b) revised design.	108
59. Anchor mask for SU-8 beams. The red areas will be etched in the mask maker, leaving chrome in the red regions.	109
60. Beam mask for SU-8 cantilevers.	109
61. Membrane etch mask (a). Magnified view of the two separate membrane etch holes and alignment marks (b).	110
62. Complete mask.	111

63. Membrane modal frequencies for the first four modes. Modes two and three are at the same frequency and represent the inverse of each other although their modal displacement is different.....	112
64. Mode shapes for the first four modes found using CoventorWare®.....	113
65. Visual bibliography. Articles are encircled with arrows indicating which authors cited each other.....	114

List of Tables

Table	Page
1. Comparison between different characteristics of a suspended meander resistor [73].	43
2. Mesh element size with the corresponding modal frequency and error measurement.	57
3. Deflection values for analytical equations and simulated analysis. The values are in microns of deflection.	76
4. Current values through each style of resistor at a specific voltage.....	80
5. Comparison between original FEA and modified FEA to include modeling the probe pad.....	92

List of Equations

Equation	Page
1. Strain introduced through thermal expansion coefficients.	16
2. Three dimensional membrane surface	20
3. Volume calculation for a function revolved around the y-axis [51].....	21
4. Membrane profile on the XZ plane.	21
5. Strain energy of bending.....	22
6. Strain energy generate by compressive stresses.	22
7. Flexural rigidity	22
8. Total Strain Energy.....	22
9. Thermal stress.....	22
10. Force/deflection equation, derivative of the total strain energy	23
11. Critical buckling load for plate buckling	23
12. Critical buckling load for a square plate.....	23
13. Maximum thickness required for elastic strain in a buckled beam.	27
14. Spring constant is the force required to deflect a spring a certain distance.....	31
15. Spring constant as a function of displacement.	31
16. Temperature distribution across a membrane.....	40
17. Electrical resistance.	40
18. Corrected resistance value to include the current crowding effects.	40
19. Power consumption	40

SELECTIVELY TUNING A BUCKLED SI/SIO₂ MEMBRANE MEMS THROUGH JOULE HEATING ACTUATION AND MECHANICAL RESTRICTION

I. Introduction

Background

Springs are a well-known device used to store mechanical energy. From an early age children are introduced to the concept of a spring through walking their Slinky® down the stairs. With applications ranging from early projectile weapon systems, most notably the bow and arrow, to vibration isolation in vehicles and precision equipment, springs are essential devices in today's world. Springs are a widely utilized component in the microelectronics industry, especially in inertial devices. Springs and other methods of mechanical suspension have been forced to keep up with the size constraints imposed by advances in technology. The continually evolving microelectronics industry has seen the geometry of electrical components decrease to the atomic level, and while enabling faster processors, forces engineers to develop advanced fabrication techniques and unique designs.

Justification

A separate but related field to microelectronics, microelectromechanical systems (MEMS) encompasses a wide array of sub-millimeter mechanical devices, and has evolved from the relatively simple silicon cantilever beam to complex micro motors [1]. Today, the MEMS industry is experiencing incredible growth, driven mostly by cell phone and tablet demand of inertial sensors, which encompasses approximately 20% of the industry [2]. From 2011 to 2012, the MEMS industry experienced an annual growth

rate approximately 12.7% Compound Annual Growth Rate (CAGR) [3]. In the same period, the integrated circuit (IC) industry witnessed a decline of approximately 2% [4]. In Figure 1, the yearly growth is partitioned to show the market share of the major components of the MEMS industry.

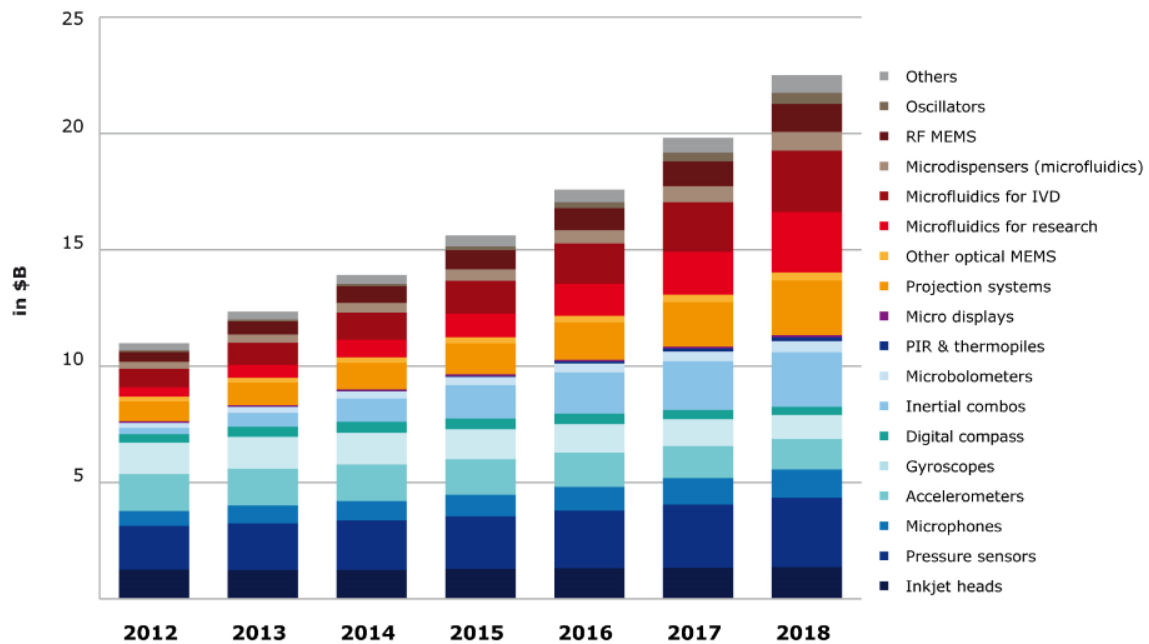


Figure 1. Projected growth of the MEMS industry [4].

Analysts expect the growth to continue at 12-13% driven by increasing demand for smart phone sensors and microfluidics devices for biological applications [2].

Researchers are continually finding new and exciting ways to use both new and existing MEMS technology to provide faster, smaller, and more efficient commercial products. The importance of cheap, small, and sensitive devices is a major goal for many MEMS researchers.

Many of these devices rely on the restoring forces of springs to return the device to equilibrium, such as when an accelerometer is displaced by an external force.

Furthermore, device geometry defines the particular characteristics of the device, notably natural frequency and sensitivity. Often times, it is difficult to tune the natural frequencies and enhance sensitivity of these devices for fear of potentially weakening the device. A decrease in individual size elements could make the device prone to stiction (static friction), a common failure mechanism amongst MEMS devices. Some devices might require an unreasonably small geometry to ensure device properties, such as the spring constant, which influences displacement sensitivity and resonant frequency are at required levels [5, 6]. By adding external springs with negative spring constant behavior, the total spring constant becomes the sum of the individual spring constants, in other words, a superposition spring. The addition of a negative spring, many of these devices can behave as if they have little or no supporting structure, without the structural instability.

Problem statement

Previous research at the Air Force Institute of Technology discovered a mechanical spring with linear regressive behavior in the form of a buckled Si/SiO₂ membrane [5]. While this behavior can be utilized for tuning the spring constant of MEMS devices, the ability to actuate the spring to change its behavior has yet to be discovered. Furthermore, a key aspect of a linear regressive spring is its negative stiffness behavior. If the spring movement could be isolated to this region, then the device would prove to be more useful. Since the device is formed from a thin membrane the actuation behavior can be used to serve in both microfluidic and pressure sensor application. Both are major areas of interest in the microelectronics industry.

Artificial negative stiffness, generated by electrostatics and used to modify material properties, has been demonstrated on MEMS accelerometers, but it requires additional power to function [7]. Additionally, methods of combining positive and negative stiffness for enhanced vibration isolation have been realized using large electromagnets on a macro scale [8]. The buckled membrane serves as a possible, low power, alternative which can decrease the overall spring constant of a system. This fact leads to the primary question driving this research: how can we develop a method to actuate and tune the characteristics of a buckled Si/SiO₂ membrane? How does the spring constant change with varying amounts of deflection in a buckled Si/SiO₂ membrane? Can we isolate the membrane deflection so it deflects only in the negative stiffness region?

Buckled structures

In order to investigate the question posed above, it is important to discuss buckled structures. Buckling occurs when a relatively slender structure is compressively loaded leading to bowing of the structure. MEMS researchers have investigated a buckled beam structure as a switching mechanism for several years [9]. This concept will be discussed comprehensively in this research. On a macro scale a device exists which behaves in similarly to the device presented in this research. The disk spring, or Belleville washer, is a device which displays an “s” shaped load-deflection curve [10].

Another feature of a buckled beam is its bistable state of operation. Bistability is best described using the playing card comparison. Picture a playing card being pinched between the thumb and fore finger. The card will initially bow in one direction, and once

a transverse force is applied, the card will snap through, and remain locked in the final position [9]. The buckled beam switch operates in a similar manner, and is useful in that it will hold one of two positions without any force being applied. In the following research, the mechanics of a buckled plate, particularly the region prior to snap-through will be investigated. The importance of this region stems from the fact that for an increased amount of deflection, the beam will provide an incrementally decreasing returning force [5].

Scope

The scope of this project includes, a thermal actuation method to tune the spring constant of the buckled Si/SiO₂ membrane. Additionally, this research seeks to restrict the outward buckled deflection of the membrane using overhanging cantilevers. Consequently, this experiment requires cleanroom equipment for fabrication to include photoresist spin stations, UV exposure tools, and chemical etching equipment. Testing requires a white light interferometer to measure deflections of the structures and a micro-Newton force sensor to record load deflection data.

The bulk of this research focuses on the mechanics behind the buckled structure. MEMS technology and processes are important for device fabrication and characterization. A series of investigative questions will guide this research towards success. This research will address the following questions:

1. What are the foundational mechanics of the buckled membrane? Buckling is well understood, but involves nonlinear equations and an understanding of finite element analysis.

2. Is there a model (both computer simulated and analytical) that can be developed to predict the behavior of the Si/SiO₂ membrane? Models have been developed and are readily available from previous research, but require tailoring to meet the needs of this project.
3. Is there a method that can be used to modify the spring constant of the buckled membrane? This is the area that will require innovation on behalf of the research team. There are several methods available to attempt to modify the behavior of the membrane. Our proposed solution is to modify the membrane actuation, and thus the spring constant, using thermal expansion brought about by a deposited surface micromachined resistor.
4. Is there a method to restrict the actuation of the membrane to the negative stiffness region? The method researched in this thesis will utilize a series of SU-8 cantilevers to overhang and apply a returning force to the membrane.
5. What is the most promising route for follow-on research? Upon completion of this research guidance for future work will be provided.

Assumptions

There are several assumptions which are necessary to simplify this research. Dr. Saif of The University of Illinois utilized a series of assumptions for use with his work tuning a bistable buckled beam [11]. These assumptions are closely related to the work presented here, and are as follows.

1. The compressive force generated by residual stress, stress between different materials, exceeds the critical load of the membrane.

2. The transverse deformation in the membrane is defined by the first buckling mode only.
3. The buckled shape of the beam is modeled by a cosine shape ($< 2\%$ error)
4. The materials used will behave elastically since strains are small.
5. The slope at any point along the deflected membrane is small (< 1).

Summary

A purely mechanical method of providing stiffness offset is needed as a method to alter the characteristics of a device without physically changing the geometry. The following chapter will focus on analytical modeling of the device in addition to an overview of the current state of technology and related areas. The third chapter will focus on the methodology used to successfully accomplish this research, with a focus on fabrication, testing and the data. The fourth chapter will present the results of the research, the fifth chapter will provide analysis of the results and any unexpected behavior, and finally, the sixth chapter will summarize the findings and provide suggestions for following research.

II. Background

Introduction

The purpose of this chapter is to present pertinent background information of the subject. Additionally, related work in the field will be discussed. The chapter begins with an introduction into the physics of semiconductors, and a discussion of the common processing techniques used for microelectromechanical systems (MEMS). Then follows is an introduction to buckling and how it can be exploited for the unique load-deflection properties. These properties are a result of buckled structures being bistable in their nature. With bistability comes unique spring behavior warranting a brief introduction into spring constants. Finally, the heat transfer aspects that are sought to actuate the membrane are discussed.

Semiconductors

Semiconductors, as the name suggests, are solid substances whose electrical conductivity is between that of a conductor and that of an insulator, and are sometimes known as “poor insulators”[12]. Conceptually, the cause of this behavior is rooted in quantum mechanics, and is primarily attributed to electron energy states.

Semiconductors are unique in that they have small bandgap energy (energy required to excite an electron to a higher energy state), unlike insulators which have large bandgaps and conductors which have either partially filled or overlapping bands [12].

Semiconductor materials can be easily manipulated by doping with other elements to become more conductive [13]. Furthermore, they are at the foundation of modern microelectronics.

Semiconductors gained widespread interest with the discovery of the first transistor by Bardeen, Brattain, and Shockley in 1947, and further with the introduction of silicon processing [14]. With the shift from vacuum tube electronics towards fabricating electronic devices on silicon chips, personal consumer electronics became a possibility, leading to the rise of Silicon Valley. During this time, researchers were also using similar fabrication processes to develop micron sized mechanical systems. Otherwise known as microelectromechanical systems or MEMS, these systems differ from integrated circuit devices in that they include movable components such as springs, gears, joints and hinges, and they can interface with electrical components.

MEMS Overview

MEMS are the integration of mechanical elements, sensors, actuators and electronics on a common silicon substrate using micro-fabrication technologies [15]. MEMS can be described as two things, mechanical and electrical components formed by specialized fabrication techniques. Similarly to integrated circuits, much of the advancement in the field can be attributed to the newly developed silicon processing. Kurt Peterson discusses in his article, “Silicon as a Mechanical Material,” four factors which helped drive the success of silicon [16].

1. Silicon is abundant, inexpensive, and can be produced with precision at high purity and perfection.
2. The processing is based on thin films which easily scale.
3. Device shapes are fabricated using photographic techniques, which also transition well to miniaturization.

4. Silicon electronics are easily batch fabricated, reducing costs.

Lastly, silicon has the ability to create a high quality native oxide (SiO_2) [13]. Beginning with an electrostatically actuated cantilever in 1965, advancements in MEMS fabrication technologies through the early 1970s enabled smaller, cheaper, and more sensitive sensors and actuators [1, 17]. By the late 1980's the advent of MEMS revolute joints and bushings enabled the fabrication of gear trains, spiral springs and other non-stationary devices as fundamental components for use in micro robots [18, 19]. Figure 2 shows SEM images for an example micro hinge and a micro electrostatic motor.

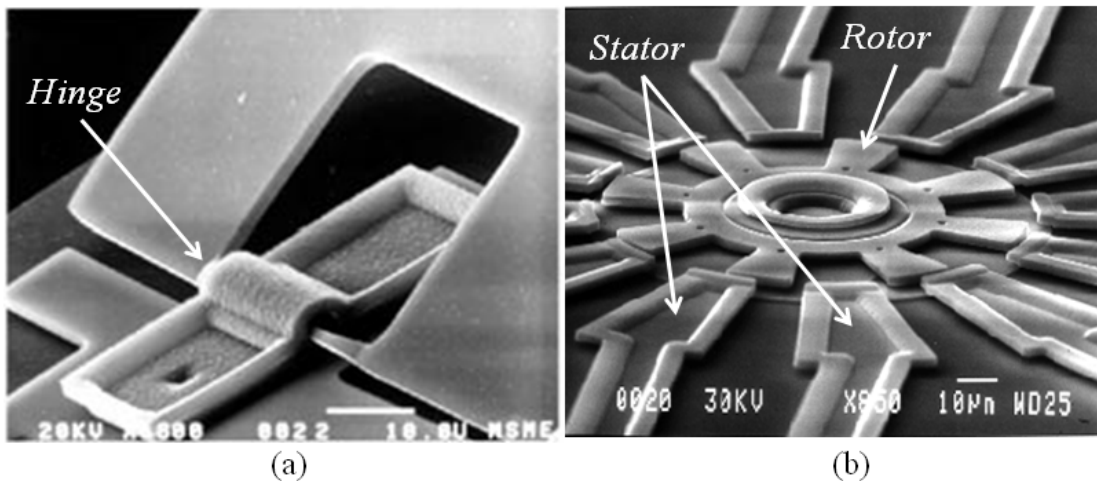


Figure 2. Scanning electron microscope image (SEM) of a MEMS hinge (a) [20]. Rotary electrostatic motor (b) [21].

In the 1990's researchers turned their attention to mechanical equivalents of electrical components, which benefit from high isolation, low power consumption and low cost [22]. One of the most popular components is the MEMS switch. Numerous configurations exist, all of which serve a similar purpose, to create distinct on and off states. Most can be electrostatically actuated between these on and off states similar to a transistor which is controlled through the "gate". Additionally, a mechanical logic

family, including AND, NAND, OR, NOR and NOT elements, was introduced in the early 1990's [23].

MEMS also encompass a variety of micro motors and micro actuators. Smaller sizes introduce unique features, most notably low inertia and friction. As a result, MEMS motors and actuators can quickly accelerate and decelerate to incredible speeds with little friction on the parts [24]. With the self-evident impracticality of a MEMS internal combustion engine, many unique actuation methods rely on external driving schemes (electrostatic [21, 25], magnetic [24], or electrothermal [26]) to displace an actuator, with the mechanical spring behavior of a structure is used to return it to equilibrium [27]. Unfortunately, MEMS structures are not without problems such as reliability, packaging, and in some cases, high voltage requirements [22].

Over the last several centuries, numerous processes and technologies were developed, which together form the basis of MEMS fabrication. These techniques can be separated into four distinct categories, which include: imprinting a design, deposition of layers, removal of layers, and the introduction of alien atoms into a material, and are otherwise known as *photolithography*, *film deposition*, *etching*, and *diffusion/ion implantation*, respectively [28].

MEMS Fabrication

Many of these fabrication processes were designed to be used to make electronic devices. However, fabrication equipment and processes are used by researchers in the MEMS field to create a diverse collection of sub-millimeter sized movable mechanical structures. Devices are typically fabricated using one of two overarching techniques

involving either manipulating thin films deposited on the surface of a substrate or by machining the substrate itself, and are commonly known as *surface micromachining* and *bulk micromachining*, respectively [17]. A third process, known as *micromolding*, builds a polymer mold with material deposition into the mold volume to form a structure [29]. Of particular importance to this research are the first two methods, which will be discussed in more detail.

Surface micromachining

The term surface micromachining refers to additive processes which form structures on top of supporting wafer surfaces. These structures can be formed using a combination of photolithography, film deposition, and etching. Photolithography is used to imprint desired patterns to form the shapes of structures either through etching or deposition, shown in Figure 3 (a,b). The Book “Fundamentals of Semiconductor Fabrication” defines photolithography as “the process of transferring patterns of geometric shapes on a mask to a thin layer of photosensitive material (called photoresist) covering the surface of a semiconductor wafer” [13].

When a design is imprinted on a wafer, film deposition is a common method used to form a structure, shown in Figure 3 (c). Both metals and non-metals can be deposited using one of two processes, physical vapor deposition (PVD) or chemical vapor deposition (CVD). PVD is typically used for metal deposition, and is categorized by its approach of removing material from a solid target and transferring it to the wafer [13]. Sputtering, which produces a conformal film, is a PVD process by which plasma ions bombard target material sending a shower of target material ions towards the substrate [28]. Conversely, evaporation produces unidirectional layers by heating metals to near

melting temperatures, raising the vapor pressure, and when combined with a high vacuum, ejects the material [28]. Of particular importance to this research is a method known as electron beam evaporation, which uses an electron beam bombardment to heat the metal. CVD in contrast, is entirely a chemical process. Gasses react and deposit products on the substrate with deposition rates determined by temperature with lower temperatures requiring plasma assistance for modest deposition rates.

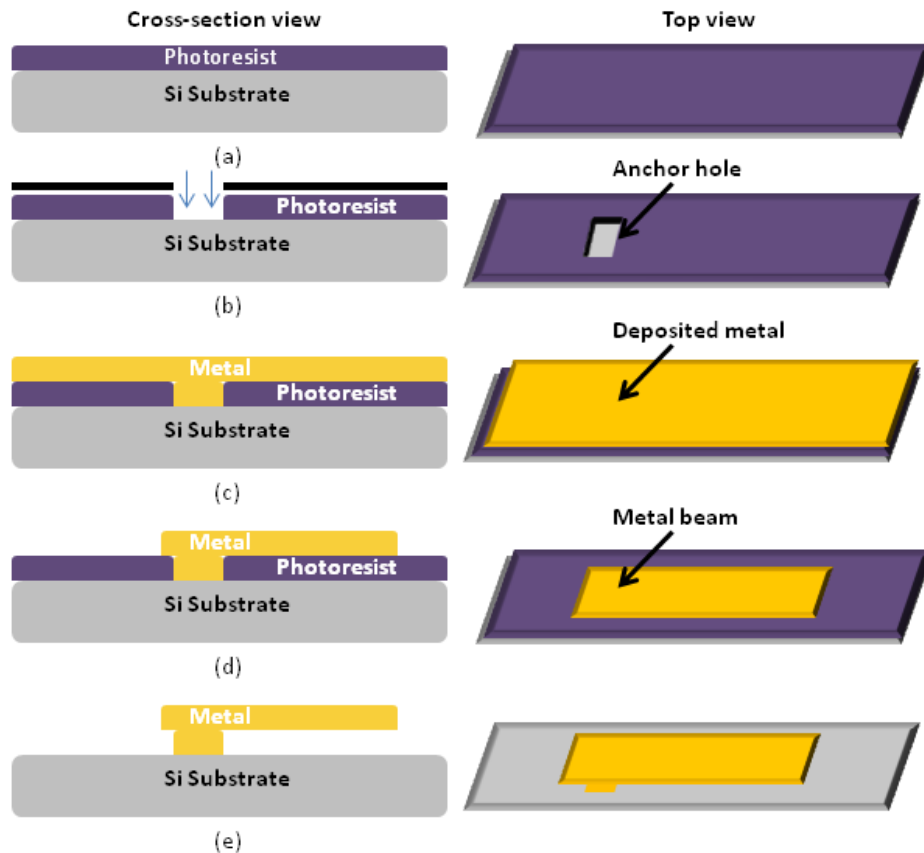


Figure 3. Surface micromachining process illustrating the formation of a cantilever beam. (a) Photoresist spin coating. (b) Photoresist exposure to desired mask pattern. (c) Film deposition. (d) Beam geometric shaping through another photolithographic process. (e) Sacrificial layer etch.

Typically, once a layer is deposited, the supporting structure, known as a sacrificial layer, will be etched, freeing the structure apart from where it is connected to the substrate [30]. A typical surface micromachined device process is shown in Figure 3.

Bulk Micromachining

While etching is used to release or define the geometries of surface micromachined structures, it is traditionally associated with bulk micromachining. The art of selectively removing precise amounts of silicon from a substrate has been thoroughly studied, and is used to fabricate membranes, trenches, holes, and undercut surface structures [31]. Liquid or “wet” etching (aqueous chemistries, typically acids in bases in which the bulk silicon is submerged) or dry (vapor and plasma) etching techniques are used to form either isotropic or anisotropic etch profiles illustrated in Figure 4 [31].

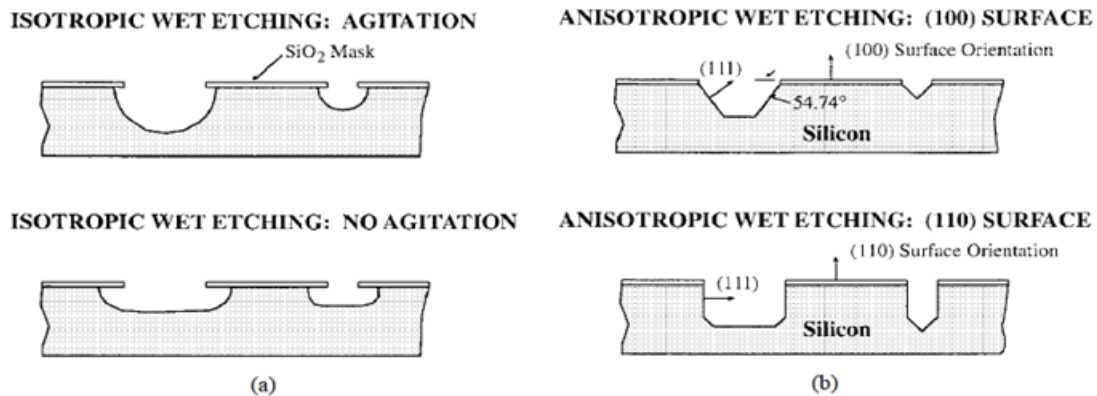


Figure 4. (a) Isotropic etching of silicon. (b) anisotropic etching of two different crystal oriented silicon substrates. Modified from [31].

Etch chemistries in both categories can be used to either etch equally in all directions (isotropic) or along crystal planes creating sharp features (anisotropic) [31].

In this research a dry etching method known as *deep reactive ion etching* (DRIE) is used to form the thin membranes. DRIE is an iterative process which involves etching for a predetermined depth, coating the inside of the etch surface with passivation chemicals, and directionally bombarding the bottom surface to remove the passivation layer [32]. DRIE is a quick and primarily anisotropic process enabling high aspect ratio features to be formed.

Hybrid Process for this Research

This research utilized a hybrid process combining surface and bulk micromachining. In order to fabricate the membrane used in this research, a bulk micromachining process using a DRIE creates a backside cavity and released the top two layers of a silicon on insulator (SOI) wafer. Surface micromachining is employed to fabricate the topside resistors for thermal actuation and the cantilever beams used to restrict the buckled displacement of the membrane. These processes involve photolithography processes, material deposition, and etching to form the desired structures.

Residual Stress

Stress is the primary element causing buckling, and it is a basic principle within the spectrum of strength of materials. Robert Mott defines stress in his book *Applied Strength of Materials* as “the internal resistance offered by a unit area of the material from which a member is made to an externally applied load” [33]. In thin films, stress develops between layers for a variety of reasons. Kaltsas *et al.* attribute the primary causes of the stress being a mismatch of lattice constants, coefficients of thermal

expansion and the growth procedure [34]. Silicon-on-insulator (SOI) wafers used in this research are made up of thin films and inherently contain residual stress. In the case of this research, the primary cause of residual stresses is the difference between the coefficients of thermal expansion (α) of silicon ($2.6 \times 10^{-6}/\text{K}$) and silicon dioxide ($0.5 \times 10^{-6}/\text{K}$) [35]. Additionally, the resulting strain in a film can be calculated using Equation 1 [36].

$$\varepsilon = -\Delta\alpha(T_2 - T_1) \quad (1)$$

Where ε is the strain, $\Delta\alpha$ is the difference in the coefficients of thermal expansion, and T_1 and T_2 are the deposition and cooled temperature respectively. The actual deflection resulting from residual stresses behaves nonlinearly because the silicon layer is resisting strain in the SiO_2 layer. As a result, the residual stress is primarily observed in the SiO_2 layer [37]. Furthermore, the silicon device layer will contain a negligible amount of residual stress because of its higher modulus of elasticity, crystalline structure, and doping [38]

The temperature difference is introduced during the fabrication of SOI, and more specifically in the bonding and subsequent anneal steps [39]. Once the wafer is cooled, the differences in the coefficients of thermal expansion result in stress gradients which cause an internal bending moment. If the structure is longer than the critical length, it will buckle [40]. Silicon, having a larger coefficient of thermal expansion, will attempt to shrink more than the silicon dioxide upon cooling [41]. Initially, as a result of the handle wafer (substrate) being significantly thicker than the oxide and the device layer, the top

layers will remain undeflected. Once the handle portion is etched away from the oxide and device layer, the resultant thin layer will no longer be physically constrained, and will transition to a lowest energy state corresponding to one of the bistable buckled states [36].

Buckling

The mechanism at the heart of this research is a phenomenon known as buckling. Buckling, or elastic instability, is a failure mechanism which, when subjected to a critical stress, causes a slender structural member to suddenly deflect drastically. With additional force the device will collapse [33]. A basic buckling scenario, illustrated in many mechanical engineering texts, is a cylindrical column loaded in compression. Shown in Figure 5 below, the column is compressively loaded and will deflect in the direction corresponding to the lowest inertia.

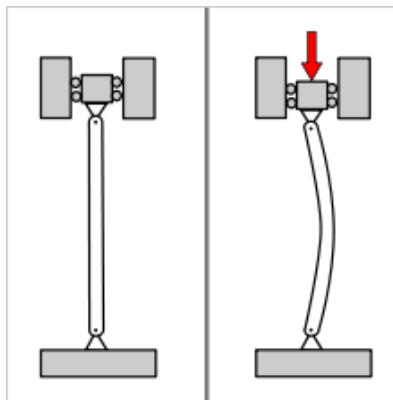


Figure 5. A slender column showing buckling when exposed to an external axial load [42].

In standard macro sized structures, such as bridges, in which the slender member acts as a support, buckling is regarded as a failure mechanism and undesired [43]. However, by displaying unique characteristics, buckling is sought out in this research.

As previously stated, compressive stress in the membrane is due to residual stress from fabrication. While residual stress buckling is the most common form used in MEMS, other methods of creating a buckled beam have been used. One such method is to apply a compressive force on the edges from an external actuator, and while this allows for a closer control of the compression, it requires bulky actuators and external power [11]. Others use a pre shaped buckled beam or membrane [44].

Figure 6 illustrates the buckling concept as it applies to plates. The compressive stresses are indicated by arrows applied over the surface [45]. Figure 6 shows one of the multiple buckling modes possible for a structure with a load greater than the critical buckling load [46]. Each of these modes corresponds to a specific compressive load on the plate.

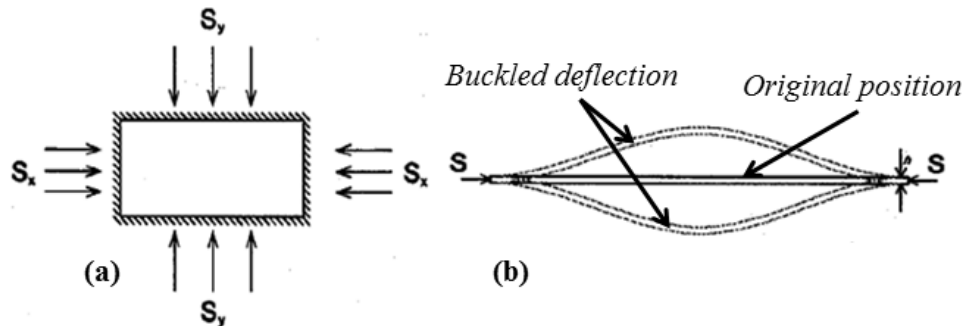


Figure 6. (a) membrane with compressive buckling stress shown. (b) cross-section of the buckled membrane with upper and lower equilibrium states (superimposed on lower plate diagram) ©IEEE 1994 [45].

It is important to note that although the membrane is buckled, the membrane operates within the elastic region during initial buckling and throughout actuation [47]. This is supported by the fact that silicon fractures at the upper end of the elastic region without undergoing plastic deformation, approximately 600 MPa [48]. Micro Raman Spectroscopy indicates a peak stress value of 240 MPa within the membrane during

buckling and transverse actuation [5]. In this case, the first mode accurately depicts the behavior of the membrane.

In traditional linear mechanics, displacements are proportional to loads; however, buckled structures display nonlinearity in this sense [46]. This situation is best demonstrated in Figure 7 in which an increasing load results in linear deformation until the critical buckling load is reached [46]. It is at this location that buckling leads to three possible deflection positions, only one of which is linear. The center line represents the unperturbed location where the membrane will come to rest, should no lateral force act on it or imperfections exist in the material. This behavior is analogous to the ball resting on the top of the hill, shown in the following section. In reality, the device will follow an alternate path prior to buckling. Budiansky *et al.* explain how imperfections present in materials will cause structure to deviate from theoretical behavior [49].

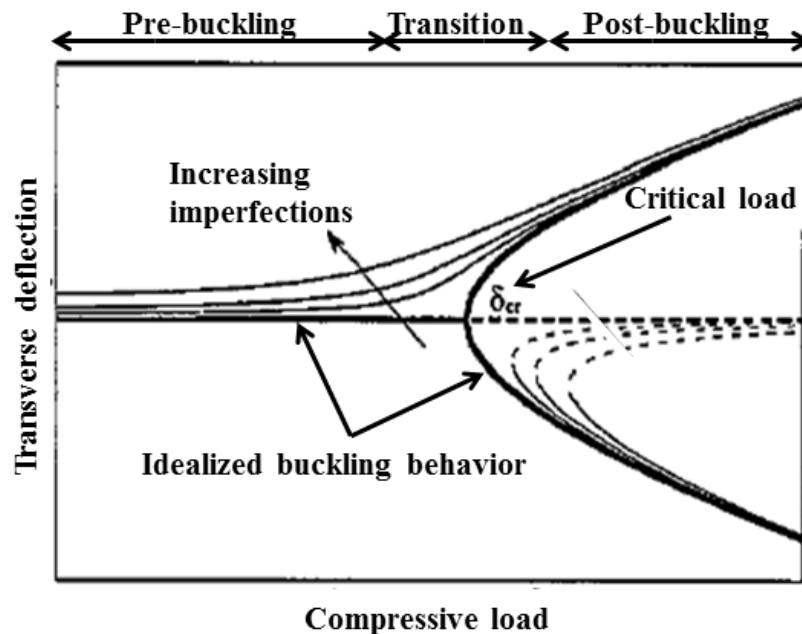


Figure 7. The equilibrium path of the center of the membrane under an increasing load. Y-axis indicates center out-of-plane deflection. Modified from [50].

By applying a compressive load, the membrane will begin lateral deflection prior to the indicated bifurcation point (δ_{cr}) with actual buckling occurring at a lesser load [49]. The modeling used in this research assumes idealized buckling behavior because it uses imperfection free material. This approximation is close to the actual buckling behavior during post buckling, which is the location of interest to this research.

When buckling occurs, formulas describing the shape of the deflected surface can be used to estimate the resultant buckled profile. The deflection surface of the membrane, where stress in the x-direction (σ_x) is approximately equal to the stress in the y-direction (σ_y), can be represented by Equation 2

$$z = \frac{\delta}{4} \left(1 + \cos \frac{2\pi x}{a} \right) \left(1 + \cos \frac{2\pi y}{b} \right) \quad (2)$$

where x and y are the locations on the plate, a and b are the width and length of the plate, and z and δ are the vertical deflection and maximum center deflection, respectively. Using Matlab, the Equation 2 can be viewed as a three dimensional plot assuming a thirteen micron initial deflection shown in Figure 8.

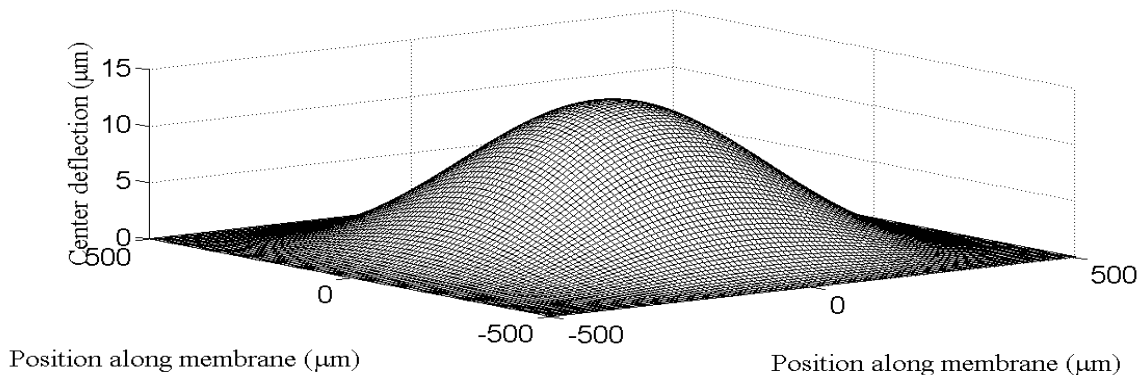


Figure 8. Computer generated three dimensional profile of a buckled membrane.

Occasionally, it is useful to determine the enclosed volume under the membrane. By actuating the membrane, a volume change will occur with a subsequent change in pressure. In order to analytically determine volume change, a revolution integral is used, shown in Equation 3.

$$V = \int_a^b \pi x^2 dw \quad (3)$$

The volume equation depends on x as a function of w. Setting y equal to zero in Equation 2 creates a two dimensional profile [51]. We now have an equation to use in the volume calculation. However, the equation must first be solved for x as a function of w. Equation 4 shows that result.

$$x = \frac{1000 \left[2\pi - \cos^{-1} \left(\frac{-\sqrt{z}}{\sqrt{a}} \right) \right]}{\pi} \quad (4)$$

Introducing Equation 4 into Equation 3 and solving the integral determines the volume encompassed by the membrane.

The outward deflection of the membrane is found at the location of minimum strain energy. Equations used to characterize a buckled plate combine the energy generated by both the strain energy of bending and the work done by the compressive forces during buckling [52]. Equation 5 and Equation 6 provide those two energy values, respectively.

$$U_b = \frac{\pi^4 W_o^2 D}{8} ab \left(\frac{3}{a^4} + \frac{3}{b^4} + \frac{2}{a^2 b^2} \right) \quad (5)$$

$$U_c = \frac{\sigma_x h}{2} \int_0^a \int_0^b \left(\frac{\partial w}{\partial x} \right)^2 dx dy + \frac{\sigma_y h}{2} \int_0^a \int_0^b \left(\frac{\partial w}{\partial y} \right)^2 dx dy = \frac{3}{32} \pi^2 \delta^2 h \frac{b}{a} \left(\sigma_x + \frac{a^2}{b^2} \sigma_y \right) \quad (6)$$

Where W_o is the center deflection, h is the thickness, a and b are the length and width, σ_x and σ_y are the compressive stresses, and D is the flexural rigidity represented by Equation 7

$$D = \frac{Eh^3}{12(1-\nu^2)} \quad (7)$$

Where E is Young's modulus, ν is Poisson's ratio, and h is thickness. Adding the two energy equations, solving the integrals, and simplifying the equations results in the total strain energy of the membrane which is represented by Equation 8 [45].

$$U = 33 \frac{Dh^2}{a^2} \left(\frac{W_o}{h} \right)^4 + 100 \frac{Dh^2}{a^2} \left(\frac{W_o}{h} \right)^2 \left(1 - \frac{\sigma}{\sigma_{cr}} \right) \quad (8)$$

Thermal behavior is studied in this thesis, and Equation 8 can be modified to include thermal stresses. By adding thermal stress (Equation 9) to the total stress (σ) in Equation 8 will accommodate for the addition of heat to the buckled membrane.

$$\sigma_{therm} = -E_{eff} \alpha_{eff} (T - T_{\infty}) \quad (9)$$

Where E_{eff} , α_{eff} , T_{∞} , and T are the effective biaxial Young's modulus, effective coefficient of thermal expansion, the ambient temperature, and the current temperature of the sample.

The derivative of Equation 8 represents the force/displacement characteristics of the plate, and will be used for monitoring the spring constant change as the plate increases in deflection.

$$\frac{dU}{dx} = 132 \frac{Dh^2}{a^2} \left(\frac{W_o}{h} \right)^3 + 200 \frac{Dh^2}{a^2} \left(\frac{W_o}{h} \right) \left(1 - \frac{\sigma}{\sigma_{cr}} \right) \quad (10)$$

This derivative is also used to find the minimum, and through rearrangement, results in the critical buckling load for the membrane shown in .

$$\left(\sigma_x + \frac{a^2}{b^2} \sigma_y \right)_{cr} = \frac{4 \pi^2 D a^2}{3 h} ab \left(\frac{3}{a^4} + \frac{3}{b^4} + \frac{2}{a^2 b^2} \right) \quad (11)$$

Additionally, for a square plate with uniform compressive loading, Equation 11 reduces to .

$$\sigma_{cr} = 5.33 \frac{\pi^2 D}{a^2 h} \quad (12)$$

Buckling is assumed to occur above this value. When the total strain energy () is plotted, the estimated deflection of a buckled plate is shown, corresponding to the minimums of the curve. Graphical representation of one, two, and

three multiples of the critical load with respect to the total strain energy () is shown in Figure 9.

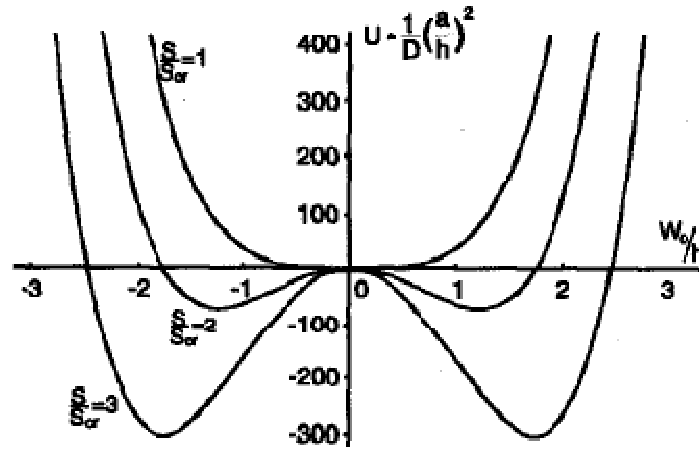


Figure 9. Total strain energy with reference to the center deflection. Multiple lines showing increased compressive loading illustrate how the distinct low energy states are formed ©IEEE 1994 [45].

The x-axis identifies the out of plane deflection as a ratio to the height of the original structure. When the membrane buckles it will deflect outwards until it reaches the lowest energy state. As the load increases, the minimum energy values decrease and travel further outward on the x-axis. This indicates that as the load increases, the deflection also increases. At loads equal to or below the critical buckling load, the plot has only one minimum energy location, the zero deflection position. Recall from Figure 7 that this indicates the equations assume a defect free membrane following ideal buckling behavior.

Because the membrane used in this research will be under compressive stress above the critical buckling load there are two minimum energy locations. The membrane will be in equilibrium at either location, buckled in and buckled out, a characteristic known as bistability.

Bistability

A unique characteristic of buckling is the ability of a buckled structure to switch between two states of minimum energy. Mechanically bistable systems demonstrate interesting phenomena surrounding the switching mechanism. Jensen *et al.* best illustrate this mechanism through the “ball-on-the-hill” analogy demonstrated in Figure 10 [53]. The ball comes to rest at either of the two “pits” or low energy equilibrium states. This concept dually applies to the buckled membrane with the exception that in the case of the membrane, the pits are of equal depth. Upon reaching the critical load, the membrane will buckle in one of two directions as shown in Figure 6. An interesting concept arises during actuation from one equilibrium state to another. When a force is applied to the ball in an effort to transition between equilibrium states, the required force will rise in conjunction with the increasing slope of the hill.

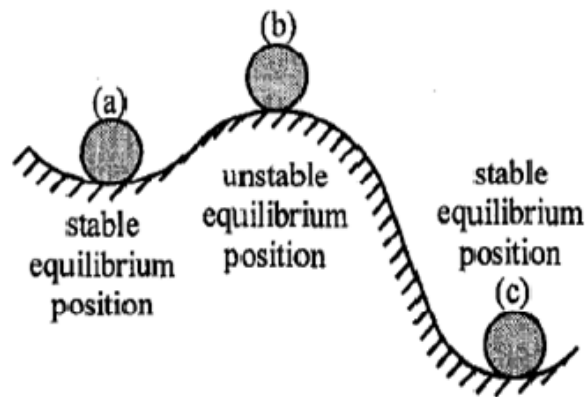


Figure 10. The ball-on-the-hill analogy demonstrating the concept of equilibrium states [53].

Once the slope of the hill begins to flatten, the load will reduce until point (b) is reached. Further displacement of the ball will require no force to transition it to the final equilibrium position. This behavior is known as snap-through. Qiu *et al.* used two

buckled beams connected at the center in a prefabricated buckled shape to test snap-through behavior [9]. Their goal was to prevent an intermediate, unsymmetrical mode from occurring prior to snap-through by connecting the two buckled beams. They provide a useful figure for illustrating the snap through phenomenon [9]. In Figure 11 snap-through is shown in three sequential steps.

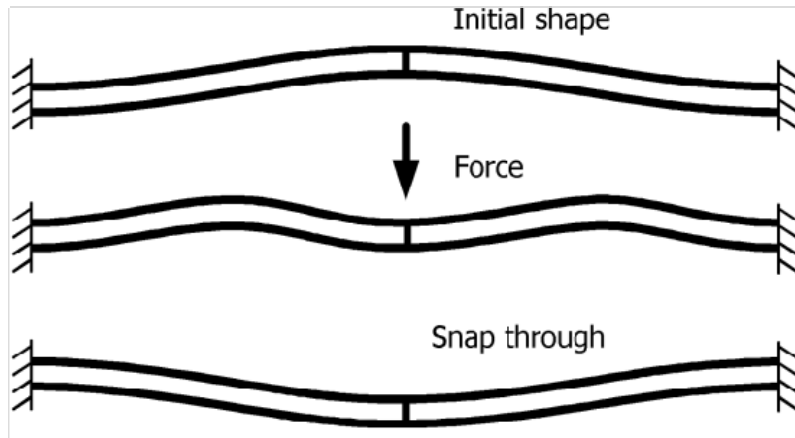


Figure 11. Three sequential cross-sectional diagrams which illustrate the snap through phenomenon in beams and membranes © IEEE 2004 [9].

The first position is the initial equilibrium position, and with an applied transverse force, the membrane will pass through the second position and snap to the final, second equilibrium position. The beginning and ending positions correspond to the low energy regions depicted in Figure 9. The unique characteristics of this region can be seen in the spring constant behavior.

Realized Applications of Bistability

MEMS researchers exploit this concept for use in many devices. The ability of the device to remain in one of the two equilibrium states without additional energy input make this mechanism desirable in low speed switching and memory applications [54].

Beat Hälg demonstrated a bilayer thin metal and SiO₂ beam for use with nonvolatile memory. Illustrated in Figure 12 the beam can represent digital 1 or 0 depending on the position of the beam.

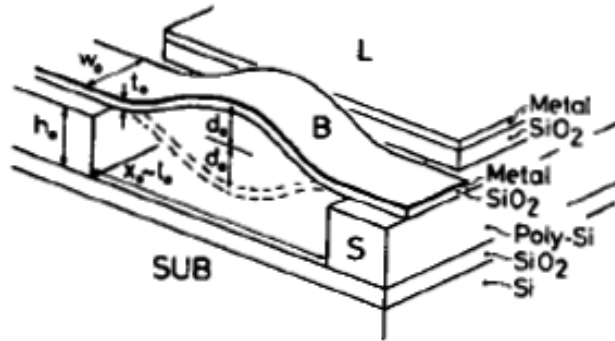


Figure 12. Schematic representation of the proposed nonvolatile memory cell. Features include, spacer (S), beam (B), substrate (SUB), and lateral electrodes (L) ©IEEE 1990 [55].

Hälg's research addresses several key questions regarding bistable mechanisms. First, electrostatic actuation of a buckled beam or membrane requires large voltages, unless the length to thickness ratio exceeds 1000 [55]. Additionally, the beam maintains its state under high acceleration, but is sensitive to fracture because of the necessary high length to thickness ratio. Finally, the beam will witness stresses within the elastic region even at snap through assuming the thickness is less than what is given by Equation 13.

Equation 13 Maximum thickness required for elastic strain in a buckled beam.

$$t^2 \leq 0.01(\sigma_{lim} / \sigma_0)(\sigma_{lim} / E) \quad (13)$$

Where σ_{lim} and σ_0 are the yield strength and the residual stress of the beam, respectively. E is the Modulus of Elasticity and t is the relative thickness. While Equation 13 indicates that a SiO₂ beam is an order of magnitude smaller than required for

elastic deformation, a silicon beam approaches plastic deformation. We know however, that Si fractures upon reaching the elastic limit, so the mere fact of fabricating an intact Si membrane suggests the silicon is within the elastic region [5].

Hälg's research was piggybacked by a group of researchers in Sweden who fabricated a buckled beam in plane with the substrate. The buckled beam was fabricated using silicon on insulator (SOI) and provides further insight to the stresses present in the layers. They also analyzed the effects of linking parallel buckled beams for added stability during snap through similar to Qiu. Although they admit the snap through force is greater [56].

Furthermore, a group of researchers have routed the high stresses of switching a buckled beam and created an alternative bistable switching design. Matoba *et al.* devised a bistable switch which contains two layers of polysilicon with a sandwiched layer of silicon nitride shown in Figure 13 [57].

Joule heating in either the bottom or top layers causes material expansion resulting in a state switch [57]. Initially, the design was fabricated in such a manner, so that upon sacrificial layer release, the residual stress in the nitride layer would apply significant compressive stress to the silicon cantilever beams inducing buckling. The nitride beam was anchored directly to the substrate. Figure 13 illustrates the finalized design, with the tension-band anchor heated to ease the switching process. Conversely to Hälg's design, this design uses thermal expansion forces to actuate. Voltage on I_1 causes the nitride anchor to expand, forgoing the intense stresses at snap through. An additional voltage can be applied to I_2 which expands the top layer of silicon and forces the switch to the down position.

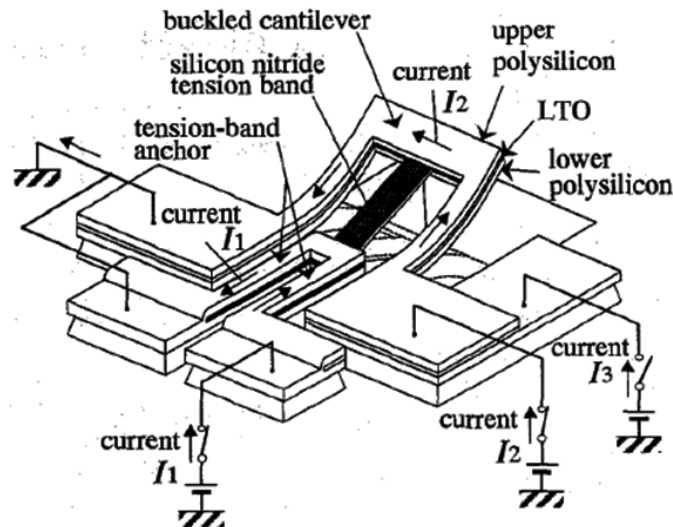


Figure 13. Bistable snapping microactuator. Bistability equilibrium position is caused by the tension band applying a compressive force to the beams, and the beams resisting the bending. The low energy state created by this effect is similar to what occurs during buckling ©IEEE 1994[57].

Goll *et al.* devised another temperature actuation scheme which contains an enclosed meander resistor beneath a buckled membrane illustrated in Figure 14.

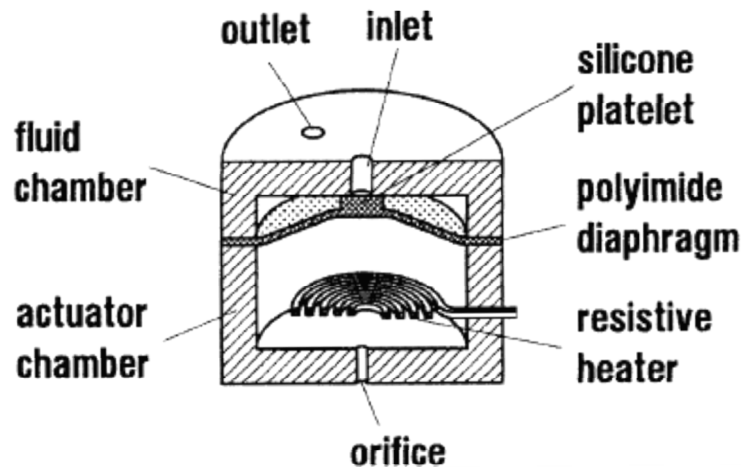


Figure 14. Bistable microvalve actuated by resistive heating [58]. The buckled membrane is used to physically close the inlet of the valve. The resistive heater is used to actuate the membrane with heat pulses.

By applying a signal to the resistor, joule heating generates a pressure wave that travels upward and switches the membrane, and closes the valve. To open the valve,

current is passed through the resistor, heating the air in the chamber to temperature equilibrium with heat transferring primarily through the orifice in the bottom. When current is removed, heat rapidly transfers out of the system creating a small vacuum inside the chamber opening the valve [58]. Another similar bistable valve has been developed, which utilizes electrostatic actuation.

Wagner *et al.* devised a valve using an electrostatic method to actuate a membrane. The device consists of two side by side buckled Si/SiO₂ membranes pneumatically coupled illustrated in Figure 15 [59].

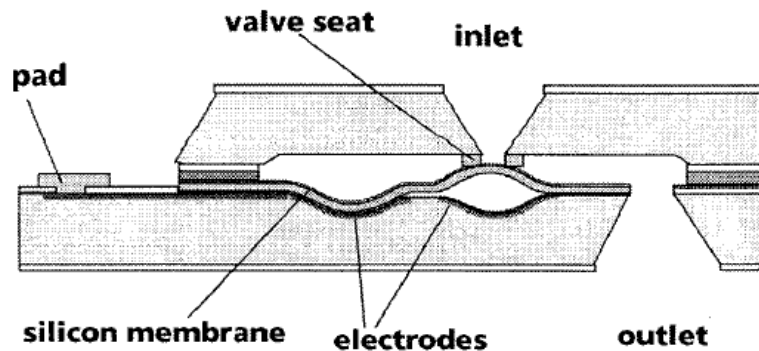


Figure 15. Microvalve with pneumatically coupled membranes. The membrane is used to close and open the fluid valve. When one membrane is actuated downward the other will be pneumatically actuated to the upward buckled position ©IEEE 1996 [59].

The resultant structure enables one membrane to buckle upwards, while the other will be buckled downwards. When the upward buckled membrane is electrostatically shut, a decrease in cavity volume increases the pressure and forces the other membrane to snap to the other equilibrium position [59]. This concept was speculated for further use as an implantable drug delivery system [60]. The researchers discovered, however, that the electrostatic actuation schemes for a buckled membrane of 1-3mm size dimensions required potentials upwards of 200v [59]. Because the membrane used in this research is

of similar dimensions, this indicates that an electrostatic actuation scheme will also require high voltages and creative fabrication techniques to accommodate the mounted rigid electrodes.

Transverse Actuation and Spring Constant

The transition between two buckled states is of primary interest to this research. The spring constant describes the load/deflection behavior of the membrane. It is a measure of the slope of the stress/strain curve [61]. In a linear spring, the spring constant will not change with deflection, therefore the spring constant can be calculated using Equation 14:

$$k = \frac{F}{y} \quad (14)$$

where F is the applied force, and y is the deflection of the spring. If the spring displays nonlinearity (as it does in this research) in the force/deflection curve, then the spring constant will change at every point along the spring. As a result the spring constant is the first derivative of the equation of the line used to map the load/deflection behavior.

$$k(y) = \frac{dF}{dy} \quad (15)$$

Examples of various springs are shown in Figure 16 with their corresponding force/displacement plot below the schematic of the spring.

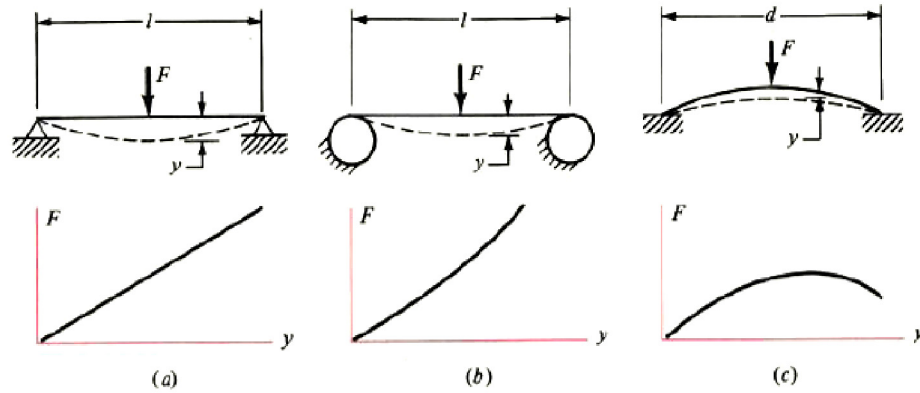


Figure 16. (a) A linear spring. (b) A nonlinear stiffening spring resulting from decreased length with increased deflection. (c) A nonlinear softening spring [62].

The situation illustrated by Figure 16 (a) is typical of a standard spring, and is an assumption used in many engineering applications. The spring in Figure 16 (b) deviates from linear behavior and exhibits an increasing spring constant, a result of the beam length shortening when deflected. The mechanism demonstrated in Figure 16 (c) exhibits similar behavior to the membrane used in this research and the disk spring. The spring will increase with a steadily decreasing spring rate until a maximum force is achieved at some point during deflection determined by the dimensions of the spring. After which the spring constant will become negative, and will require lower force for further deflection.

Linear Regressive Spring Characteristics

As mentioned in chapter 1, this researcher is focused on two areas of the buckled membrane. First, by mounting a resistor atop the membrane, we seek to actuate the membrane and change the spring characteristics. Secondly, we will attach beams to the substrate surrounding the membrane. These beams will overhang the membrane and apply a transverse force to prevent the beam from deflecting to equilibrium. To

understand exactly what these effects will accomplish, we must discuss the force/deflection curve shown in Figure 17.

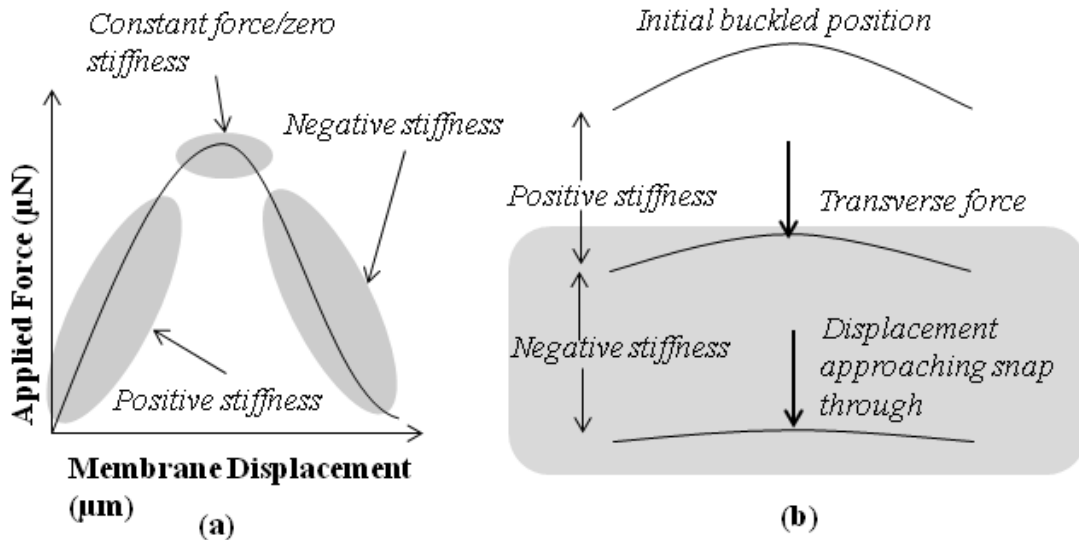


Figure 17. Spring characteristics of the membrane (a). Cross-section of membrane actuation and corresponding spring stiffness (b).

Notice that as the spring is initially compressed, the returning force is positive. At a certain location along deflection the spring returns a reducing force, corresponding to negative stiffness. By actuating the membrane the curve will increase and the stiffness will change. Additionally, by controlling the amount of outward deflection upon buckling, the membrane can be trapped to actuate in the region experiencing negative stiffness. This behavior can be seen in a commercial device known as a Belleville washer or disk spring.

Belleville Washer

A device displaying similar characteristics to the buckled membrane is the Belleville washer. Almen and Laszlo are the first researchers to derive equations and formulas for the Belleville washer [10]. They provide a comprehensive analysis of the

design and characteristics of the disk spring, and in particular, how the dimensions influence disk spring behavior. In Figure 18, a standard load/deflection curve is shown with a schematic of the disk spring [10].

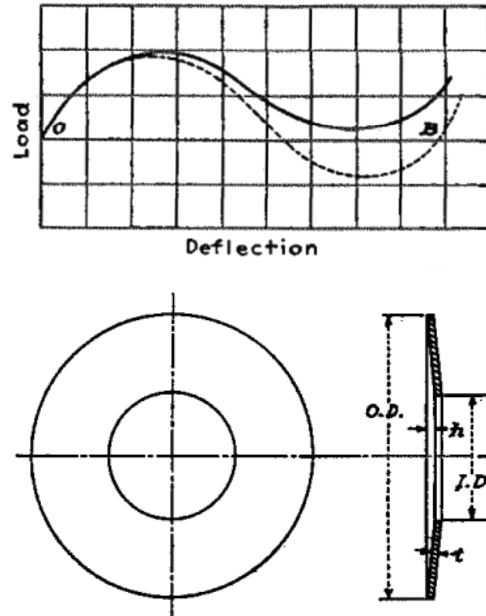


Figure 18. Nominal load-deflection curve for a disk spring (Top). Frontal and cross sectional views of the disk spring (Bottom) [10].

In the load/deflection figure, the returning load follows a sine pattern by first increasing, flattening, and then decreasing to slightly above zero, similar to what was shown in the previous section. At this location, the disk spring is snapped through but will return to the original position should the load be released. Conversely, the dashed curve Figure 18 (B) crosses below the zero force line, indicative of bistability, similar to what is seen with the membrane. Furthermore, Almen and Laszlo described how the load/deflection characteristics change with increasing initial displacement (h in Figure 18). This is particularly important to this research effort because it provides clues as to

how the membrane spring behavior is expected to change during actuation. The force/deflection plot is shown in Figure 19.

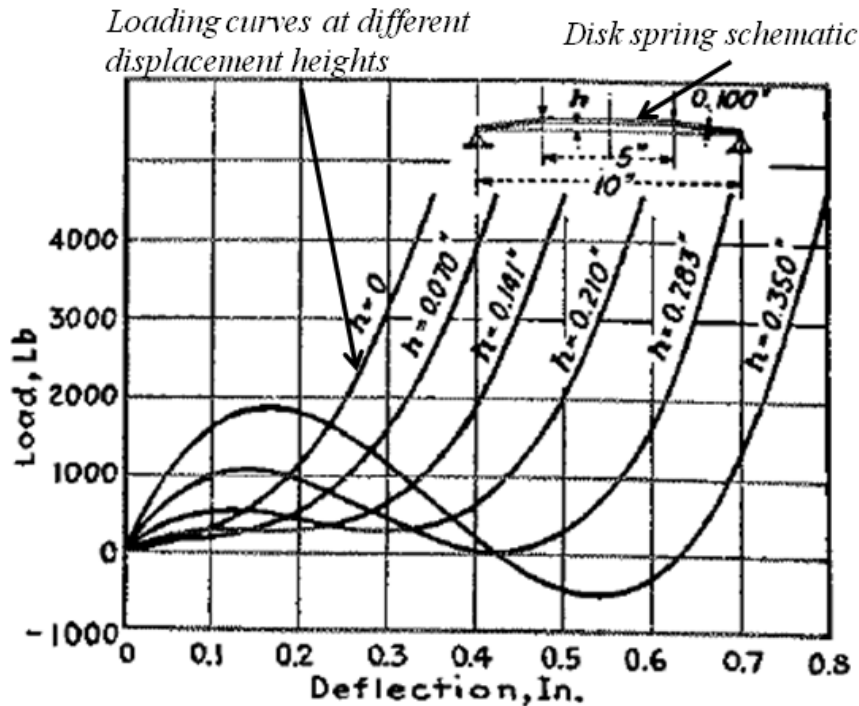


Figure 19. Load deflection behavior for a series of disk springs with differing displacements. Modified from [10].

As the initial height of the disk spring is increased, the maximum required load to deflect the spring is increased, along with the slope of the curve (stiffness).

Numerous examples of the applications of such device exist; however, it is not practical to mention all of them. Nevertheless, there are several which properly illustrate the usefulness of the device. One such example uses a stack of Bellville washers as a chain tightening mechanism. The purpose of the washers is to provide unique load-deflection characteristics, which can be altered depending on the chain tightening application [10]. Another use involves suspension dampening on vehicles. Again, the unique load/deflection characteristics, particularly the nonlinear behavior, enable the

spring to absorb a forceful impact causing the disk springs to fully deflect and remain open. The resulting device protects the damper from high impact forces, but still allows for low impact damping [63]

In an effort to understand the behavior of the proposed devices, many researchers turn to computer aided numerical modeling prior to fabrication and testing. The following section briefly introduces the process of computer based finite element modeling.

Finite Element Methods Background

While analytical equations can determine the profile and the degree of deflection in the membrane, advanced modeling is necessary to understand transverse loading, heat transfer, and the snap-through process. Through finite element modeling (FEM) techniques, stress, strain, temperature, fluid flow, deflection, electrical characteristics, and other analyses can be performed for unusually shaped or loaded objects. Steven Lepi, author of *Practical Guide to Finite Elements*, presents a summary of this method, “The [Finite Element] Method partitions a structure into simply shaped portions called finite elements, generates an approximate solution for the variable of interest within each element, then combines the approximate solutions” [64].

Partitioning a structure is similar to using the Riemann sums approach in calculus. A curve is split into numerous geometric sections, in which each of the “finite elements” can be calculated and subsequently added together. Both the finite element and the Riemann sums approach approximate the solution to a given problem. The accuracy of this solution is a function of the size of the individual finite elements in relation to the

overall device shape. In a practical situation, these calculations are performed by a computer program to spare the user from lengthy arithmetic. A program known as CoventorWare® is used in this research. It is tailored to MEMS and has three procedural “steps” which a user must complete before performing analysis.

CoventorWare® assists MEMS researchers by using familiar processes to create models for FE analysis. Users specify material properties, create a design layout, and develop a process as if the device were to be fabricated. The system compiles this information and provides the user with a three-dimensional rendition (solid model) of the device. It is at this step where the user decides the type and style of the finite elements (mesh). After generating a mesh, the user can select from a comprehensive suite of solvers, each focused on a specific area of MEMS [65]. Within these, boundary and loading conditions are specified to closely approximate actual behavior.

Heat Transfer

Heat transfer is the flow of energy as a result of a temperature difference between two media. Heat energy is transferred using one of three primary methods, conduction, convection, and radiation [66]. Conduction is of primary interest to this research, but each method will be discussed in the following section.

Heat Transfer Methods

Conduction is the method by which heat is transferred through a substance without motion of the substance itself. Conduction materials are normally solids, but liquids with zero velocity can transfer heat energy through conduction as well. Physically, conduction corresponds to motion of free electrons, lattice waves (phonons),

magnetic excitations, and electromagnetic radiation [66].

Convection refers to heat transfer by means of fluid flow. Fluid mechanics plays an important role since flow characteristics determine the convection heat transfer coefficient [66]. Furthermore, there are two forms of convective heat transfer, free and forced convection. Free convection is the local heating of a fluid near the source, upon which the fluid will lose density and be displaced by a cooler, denser fluid. Forced convection, is the process by which an already moving fluid flows over the heat source and receives heat energy, such as a fan or radiator in a vehicle [66].

The third and final method of heat transfer, radiation, is the transfer of heat through electromagnetic radiation. All substances emit heat in the form of radiation energy, but the net energy flow will be from high to low temperature [66]. Different materials have different properties corresponding to their ability to absorb, transmit, and emit radiation energy.

Heat energy is transferred through a combination of all methods in a given situation. However, the methods can be ranked, ordered by their heat transfer effectiveness: conduction, convection, and radiation. Other researchers discovered that when using small devices such as our membrane, 98% of the heat energy transferred is through conduction [67]. As a result, a conduction based approach will be used to heat and subsequently actuate the membrane. The proposed method uses joule heating of a deposited meander resistor. With the smaller sized devices, the resistor is able to achieve localized, intense heating from both convection and radiation.

Related Joule Heating Based Research

Thermal actuation is an actuation method used by many MEMS researchers. The

classic example is the MEMS lateral thermal actuator. Several research groups, however, have utilized joule heating for buckling [68]. Others have focused on the methods of fabricating a resistor on a device [67, 27]. The latter is used by Bouwstra *et al.* for detecting mass flow rates using a novel sensor design. Their design measured flow rates of fluids by detecting the shift in natural frequency of a thermally actuated, unbuckled membrane [67]. Pictured in Figure 20, the membrane is illustrated with boundary conditions for the three methods of heat transfer.

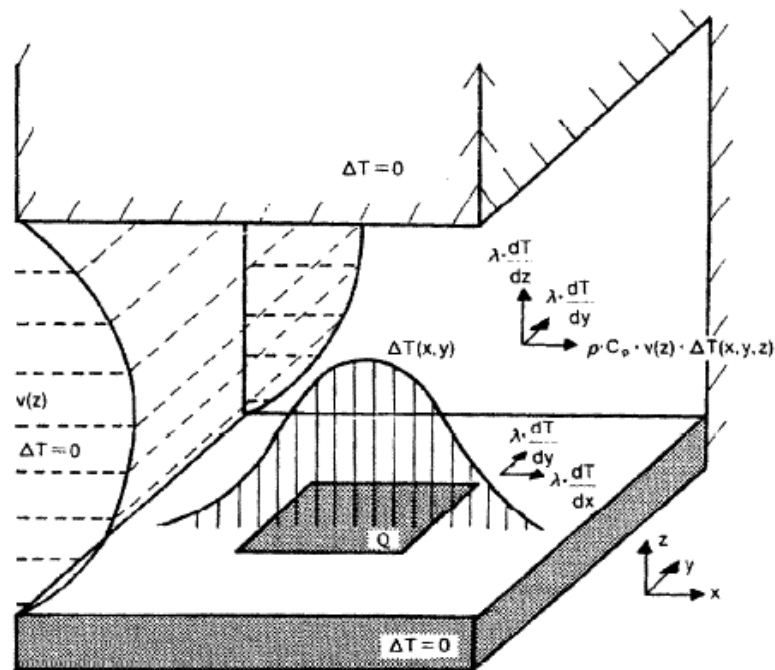


Figure 20. Membrane with heat generation (Q) and methods of heat transfer shown [67].

To estimate the temperature across the membrane, they developed what they refer to as a “simple” model for conductive heat transfer in a membrane with a centrally located resistor. Equation 16 models the temperature across the membrane

$$\Delta T_{avg} = \frac{H}{4\pi\lambda t} \quad (16)$$

Where H is the heat generation per unit time, λ is the coefficient of heat conduction, and t is the thickness of the membrane [67]. To model the temperature across the membrane, the resistor power needs to be considered. However, the resistance influences the power in the resistor and must first be considered. Heat energy transfer is controlled by the material's thermal resistance [69]. It is the ratio of the temperature gradient to the heat flow, and is equivalent to electrical resistance in [69].

$$R = \rho(l / A) \quad (17)$$

Where ρ is the electrical resistivity, l is the length, and A is the cross-sectional area of the resistor. Two resistor types are used in this research. One of which is a square, sharp cornered resistor. The resistance is altered due to the increased current density at the corners [69].

$$R = R_s(N + (k' N_{cb})) \quad (18)$$

Where R is the overall resistance, R_s is the sheet resistance, N is the number of blocks in straight regions, k is the corner block correction factor, and N_{cb} is the number of corner blocks [70]. The electrical power lost through the resistive element is converted to heat. Equation 11 provides the generated power to be used in the heat generation equation.

$$P = I^2 R \quad (19)$$

Where I is the current and R is the resistance.

Lin and Lin extended the analysis to include the deflection as a result of heating. They developed a thermal based vertical micro-actuator using a fixed end beam with an embedded doped resistor and a large plate attached to the side. Figure 21 shows a top-view schematic of the actuator.

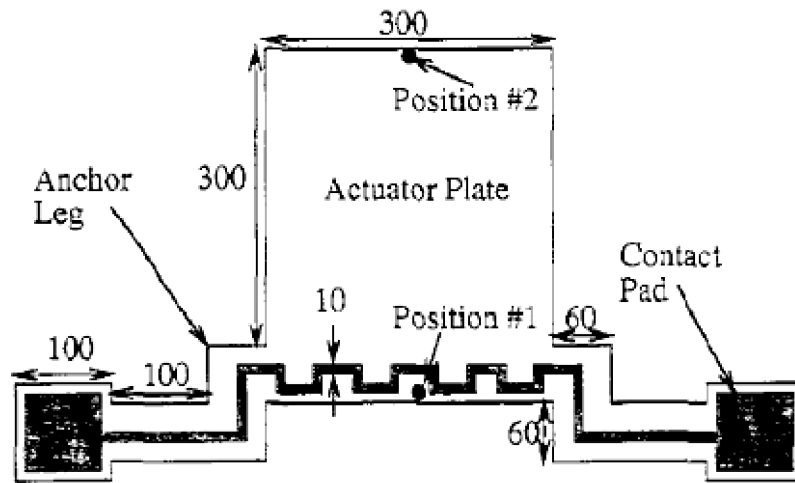


Figure 21. Vertical thermal plate actuator [27].

With an applied voltage, the beam is stressed in compression until the critical buckling load is achieved. At this point the actuator witnesses a large vertical deflection. With increased voltage, the actuator will deflect upwards similar to what is expected to be seen in this research. The authors used both analytical equations and computer simulation to model their device, but their analytical equations underestimated the actual deflection by nearly 75%. Additionally, the authors tested the frequency response of the device and found that the device would follow input up to about 100 Hz.

Thermal buckling of fixed-ended beams has been implemented in many useful MEMS devices. Chiao and Lin strictly focused on thermal buckling in low resistive beams with an applied voltage. Their research further solidified the common theme that thermal actuation schemes tend to follow input frequencies up to the order of 100 Hz

[68]. Additionally, the behavior of joule heating resulting from current tended to increase exponentially, confirming what was predicted by simulations in this research (see chapter 4). Their deflection results illustrated another important concept. Experimental results were situated between the estimates for mathematical modeling and FEM modeling. FEM overestimated the buckling deflection while analytical modeling underestimated the deflection.

While Chiao and Lin merely tested the actuation ability of a beam with an applied current, Hoffmann *et al.* employed thermal beam buckling to mechanically maneuver fiber-optic cables. They combine a vertical actuator (thermal beam buckling), to move the support from under the fiber optic, with a lateral thermal actuator to switch the position of the actuator [71]. Their beams displacements follow a similar trend as many of the other thermally actuated devices, in that the rate of further deflection change decreases with increasing temperature.

The mechanism supplying heat to the membrane in this research is a deposited gold meander resistor. Optimal designs for such a device were considered by many researchers. Some were concerned with hotplates and sensitive sensing elements [72]. Others were interested in MEMS heaters for IR applications. Lee *et al.* focused on the latter, specifically a heater design for MEMS IR sensing. They compared several features of a suspended heating resistor including, filament width, filament spacing, and total length of the resistor to the power consumption [73].

Table 1 Comparison between different characteristics of a suspended meander resistor [73].

	Design 1	Design 2	Design 3	Design 4
Filament width (μm)	20	20	20	20
Spacing (μm)	2	20	10	10
Length (μm)	200	250	150	250
Power consumption (mW)	239	372	520	446
Peak Temperature ($^{\circ}\text{C}$)	958	1211	1132	935

Their results indicate that a modest design consisting of a reasonably long resistor and sufficient spacing between filaments will provide the best heating aspect. Design 1 was the most efficient heater however, but for this research, the amount of heat is the focus. As a result, power consumption will not be considered.

Thermal actuation mechanisms are a unique aspect of MEMS systems. Although they are slow due in part to thermal relaxation times, they serve several unique purposes. They typically have large stroke lengths, for use where large displacements are required, low voltages, although power consumption may be high due to joule heating, and they can provide large forces. CoventorWare® simulation was primarily utilized in this research for understanding the behavioral effects from thermal stimuli. For experimental testing, infrared imaging enabled closer viewing of the thermal characteristics of the membrane during actuation

Summary

This chapter presented a theoretical perspective on the buckled membrane used in this research. The chapter began with a brief introduction to microelectronics; in particular MEMS techniques and history were introduced. Next, stress was introduced with a discussion about residual stresses and its importance of causing buckling.

Buckling was introduced with equations modeling the shape and critical buckling load of the membrane. In this research, buckling is sought out because it provides useful behavior, particularly a region of negative spring constant. The desired state of operation takes place between the two bistable positions of the buckled membrane which was described with reference to the ball-on-the-hill analogy. The importance of spring constant was discussed, and equations for predicting and experimental methods of finding the spring constant were introduced. Finally, the heat generation and transfer mechanisms acting in the membrane were discussed to generate an analytical equation in an effort to model resistive heating in the membrane. In the following chapter, the research methodology is discussed with an emphasis on fabrication and data collection methods.

III. Methodology

Chapter Overview

This chapter details the research methodology, which encompasses the design, fabrication, and testing procedures. Recall, that this research explores two modifications to the buckled membrane, thermal actuation and mechanical restriction. The first section of this chapter focuses on design and fabrication techniques, including all cleanroom processes up to testing of the finalized structure. MEMS processes, in particular surface micromachining and bulk micromachining, are primarily used in the fabrication of the device. Conventional processes are used for device fabrication, including: wafer cleaning, photoresist spin-on, ultra violet (UV) light exposure, chemical etching and thin film deposition. Once devices are fabricated, they are tested to compare what was predicted by modeling. These methods are discussed in the latter portion of this chapter, which presents the testing and data collection methods as they are performed in this research.

Design

The two designs featured in this section are for testing two different aspects of the Si/SiO₂ membrane. Resistors are used to heat and subsequently actuate a post buckled membrane in an effort to change the spring behavior, similar to different heights in a disk spring, discussed in Chapter 2. Two styles of resistors are investigated, a square resistor with sharp cornered filaments and a spiral resistor with rounded filaments. The second design featured overhanging cantilevers to restrict the membrane's deflection distance.

The cantilevers are used to restrict the membrane to the negative stiffness region of actuation.

Resistor Design

The initial resistor design consisted of straight edges and sharp corners. The purpose of this resistor was to quickly get a design fabricated and tested, to provide a high heater surface area, and to reach a maximum temperature under 25V. Additionally, the different filament spacing between the center five filaments and the outer two filaments was intentional. This resistor was used as a baseline for other resistor types to test their effectiveness. When designing the resistor mask for lithography, the outer portion for every model was used to enable a quick replacement of the inside filament style. Each design contained different features. The elements changed on the square resistor included, filament width, number of filaments, and filament spacing. The resistor used for this research contained the best combination for low voltage and high heating capability. The other resistor types are shown in Appendix B. The second resistor style was designed in a spiral shape to reduce current concentration around corners, which was a concern with the first style of resistor [69].

The rectangular resistor, Figure 22, was composed of a relatively thick wire. Cutbacks in the wire were situated close together, leaving low filament spacing. It was believed that this would help localize maximize the heating area while maintaining a localized heating profile. Unfortunately, low spacing could contribute to a higher rate of shorting amongst samples. The total resistance from pad to pad is estimated to be $1.07 \times 10^{-5} \Omega$.

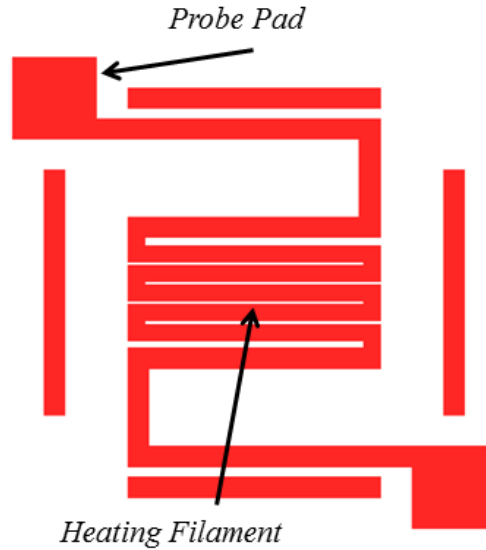


Figure 22. Square style resistor. The partial box surrounding the resistor was originally used for alignment and does not influence resistor behavior.

The spiral resistor included a thinner filament with increased filament spacing and a total resistance of $1.05 \times 10^{-4} \Omega$. These two styles enabled us to determine if a difference in filament thickness or spacing could be a factor in performance. As discussed in Chapter 2, other researchers previously investigated the effects of resistor dimensions on performance. They concluded that most geometric changes on a resistor will affect only the power requirement of a resistor of this type, while the heat generated will remain relatively the same [73]. Additionally, the goal of this research was to test the capabilities of joule heating on a buckled membrane, and minimizing power consumption for packaging and incorporating into MEMS devices will be left to future research.

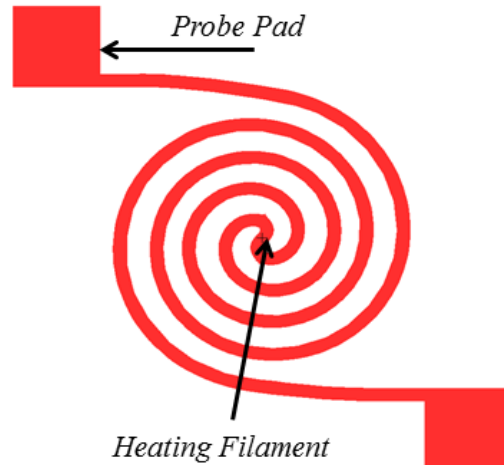


Figure 23. Spiral resistor.

Each resistor was formed into an array of 52 resistors per sample, each corresponding to a specific membrane. Figure 58 (a,b) located in Appendix B shows the resistors in their respective masks.

During the mask writing procedure, the red areas will be traced with a laser. Photoresist exposed to the laser will be developed away, leaving a primarily opaque mask with clear resistors and a clear border, used for alignment.

Beam Design

Prior to backside etching and membrane buckling, cantilever beams, formed from SU-8 photoresist, are fabricated atop the thin, joint layer of silicon and oxide. Although SU-8 has a low biaxial modulus of elasticity (5 GPa), it was chosen as a structural material since it yields thick layers of material quickly and at low cost [74] [75]. A schematic of the proposed device is shown in Figure 24.

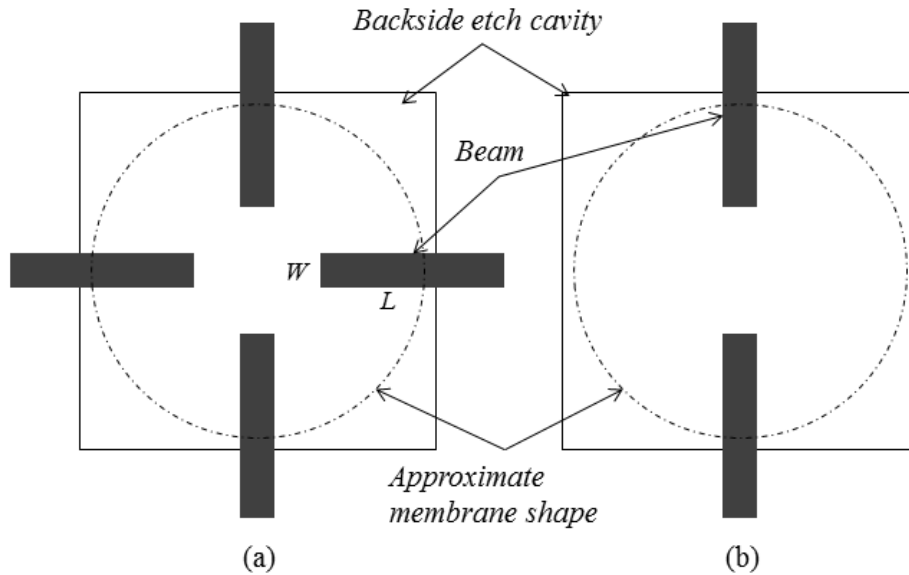


Figure 24. (a) Quad beam design. (b) Twin-beam design. The backside etch cavity and the approximate membrane shape are also illustrated for clarity. The length and width of the membrane are shown for reference.

The design consists of several geometric configurations of the beam in an attempt to experimentally determine the appropriate design required to restrict the membrane. These configurations varied by the length and width of the beam. The beam widths range from 100-250 μm and the lengths range from 600-750 μm . All of the geometric configurations are used with both a twin-beam (Figure 24 b) and a quad-beam (Figure 24 a) design.

Recall that from Chapter 2 helps identify the location during actuation at which the membrane crosses into the negative stiffness region. This is shown in Figure 25.

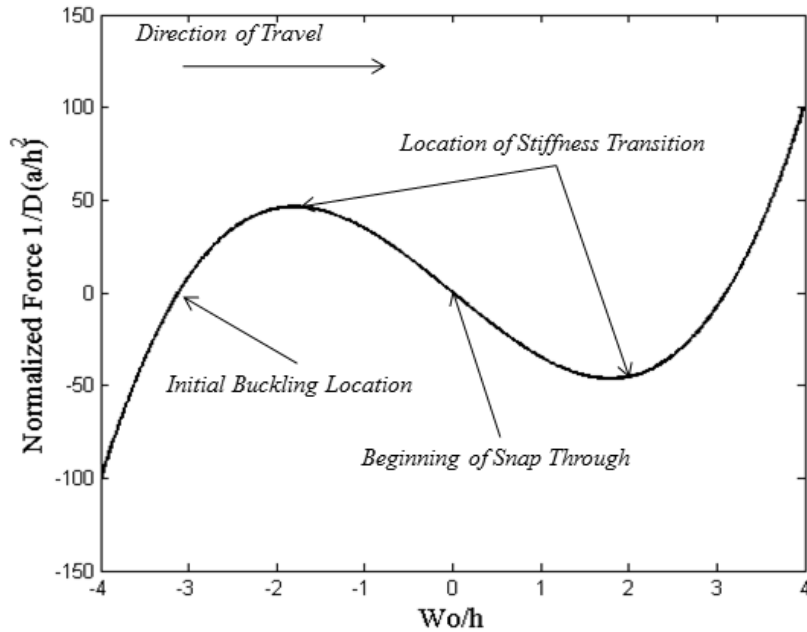


Figure 25. Analytically determined load/deflection characteristics for the Si/SiO₂ membrane. At the initial buckling location, zero force is required since the membrane is at equilibrium. At approximately 7μm deflection, the membrane is expected to transition to the negative stiffness region.

This equation estimates the transition from positive to negative stiffness to occur at 7μm of deflection from the initial position. By using the beams, we hope to restrict the membrane to this area. Ideally, one of the many styles of beams will provide the necessary returning forces to restrict the membrane.

Fabrication

A two mask process is required for the fabrication of the resistors, whereas a three mask process is used for the movement restricting cantilevers. The cantilever beams require an anchor and a beam mask in addition to the backside etch mask. The complete process begins with a bare SOI wafer. SOI is formed by first thermally growing an oxide on a standard silicon substrate followed by wafer bonding of a second wafer on top of the oxide. The topside wafer is appropriately thinned through chemical mechanical polishing

(CMP). This process uses a 5 μm top silicon wafer (device layer) and a 2 μm oxide layer for optimal mechanical properties. The resistors and cantilevers on the topside are patterned and fabricated preceding the backside etching in an effort to reduce the chance for membrane damage.

Resistor Fabrication

The SOI wafer is diced into one inch squares in preparation for processing. The specific size of the squares enables easier handling while preserving resources since each original SOI wafer yields several dozen one inch samples. In accordance with standard MEMS processes, the samples are initially cleaned using solvents, including acetone, methanol, and isopropyl alcohol with a final rinse using deionized water to remove organics and unwanted residue. The lithographic processing begins with the application a single layer of SF11 photoresist followed by a single layer of 1818 photoresist, both of which act as sacrificial layers (Figure 26 a). The SF11 undercuts the 1818 layer (Figure 26 b) preventing connection of the sacrificial gold and resistor gold, and ensuring the success of the lift-off technique for excess gold removal. Additionally, the purpose of the 1818 photoresist is used to mask the SF11 layer below which requires a deep ultra violet (DUV) photoresist flood exposure system.

1818 is exposed using an MJB3 mask aligner to define the resistor locations. Figure 58 in Appendix B shows the schematic of the resistor mask. When fabricated, the areas with red are etched from the chrome mask, while the white areas remain opaque on the mask. UV light passes through locations without chrome and will expose the photoresist below. The box surrounding the mask areas is one inch on each side and is used for alignment with the backside DRIE etch holes in order to position the resistors on

top of the membrane. Although this method allows for only approximate alignment, it succeeds so that the resistors are deposited on top of the membrane.

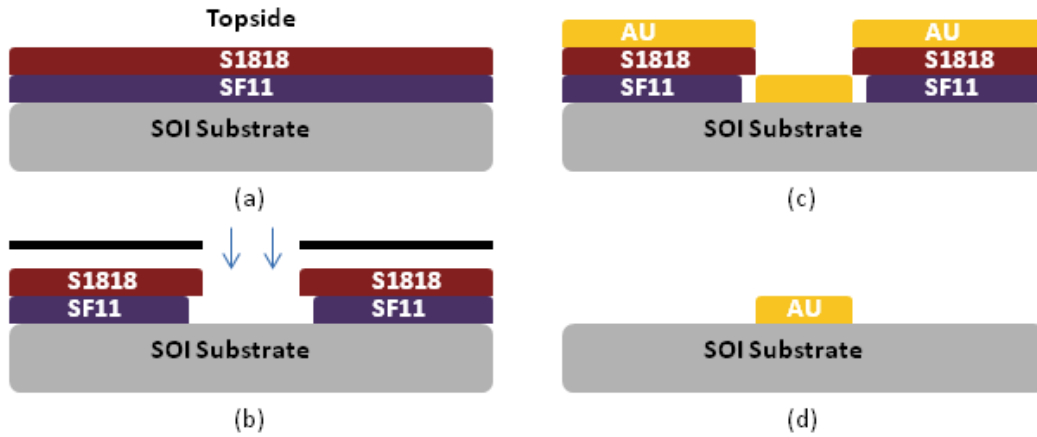


Figure 26. Resistive heating element deposition process. (a) initial photoresist spin-on, (b) ultraviolet (UV) light exposure and develop, (c) gold deposition through electron beam evaporation, (d) excess gold and photoresist removal.

The masking material is a positive photoresist, indicating that ultra violet light chemically alters the photoresist so that it will dissolve in a developer solution. As a result, the SF11 is uncovered and exposed using the aforementioned deep ultra violet light system (Figure 26 (b)). Following a brief develop procedure, bare silicon is exposed in locations where the resistors will be deposited. To do this, gold is evaporated over the surface of the sample, depicted in Figure 26 (c). The samples are now ready for the backside etching process.

Beam Fabrication

To fabricate the movement restricting cantilevers a similar fabrication process is used. As with the resistors, the beams are fabricated atop the membrane prior to backside etching. The purpose of this, similar to the resistors, is to preserve the membrane's integrity. Membrane fragility eliminates the possibility of post processing on the

membrane, which can cause failure. Additionally, fabricating the beams atop the membrane after it is released does not allow the membrane to deflect upwards into the beams and become constrained.

The SOI is briefly submerged in a weak HF solution followed by a normal cycle in an oxygen asher to remove native oxide and promote SU-8 adhesion. A single layer of 1818 photoresist is spin coated on the topside of the sample and heated to evaporate the solvents, Figure 27 (a). It is subsequently exposed using the anchor mask, and acts as a sacrificial layer for the SU-8, Figure 27 (b). SU-8 is spin coated atop the previous layer of photoresist and exposed according to the beam mask, Figure 27 (c,d). Once again, the solvents are evaporated through heating. SU-8 is a negative tone photoresist, indicating that appropriate ultraviolet (UV) exposure promotes crosslinking of SU-8 by activating the photoplastic material [76]. An additional baking period, appropriately dubbed the post-exposure bake, is required to crosslink and “set” the photoresist. A temperature ramping method is used to prevent SU-8’s characteristically high stresses developed in the crosslinking phase.

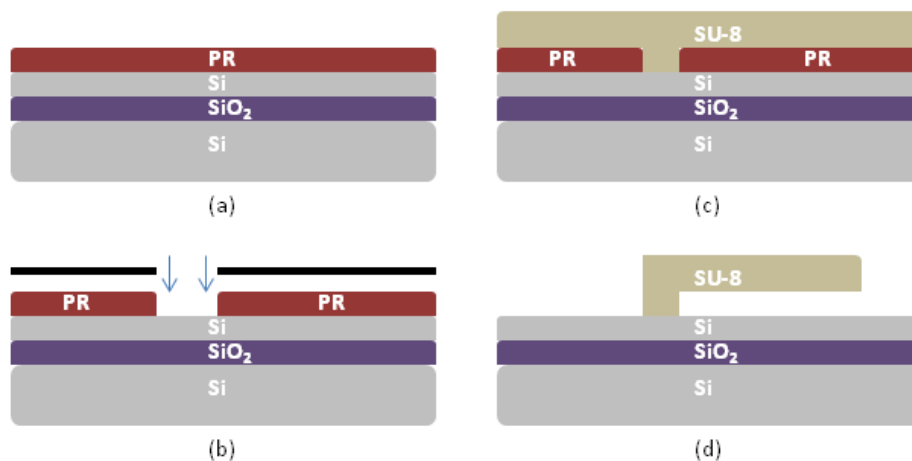


Figure 27. Fabrication sequence for the SU-8 cantilever.

After the SU-8 exposure, the photoresist is developed leaving only the beam. The sacrificial photoresist is also dissolved in this process because of its solubility in SU-8 developer. Topside fabrication is accomplished following the backside patterning but before backside etching.

Backside Etch Process

The thick side (handle) portion of the SOI is patterned using SU-8 to protect areas where etching is undesired. This design consists of a series of one millimeter squares and circles patterned using standard photoresist deposition procedures, exposure and develop processes. Following spin coating, the solvents are evaporated by sample heating. Again, temperature ramping is used to prevent SU-8's characteristically high stresses developed in the crosslinking phase. Although high stresses do not affect the mechanical properties of the device, it can cause the SU-8 to delaminate, affecting the DRIE process [76].

After photoresist processing, the sample is etched using the deep reactive ion etching (DRIE) method previously discussed. Etching selectivity permitted using the oxide layer on the topside as a natural etch stop. The resultant structure was composed a thin layer of both silicon and silicon dioxide (5 μm and 2 μm) which buckles out of plane. The complete process is shown in Figure 28.

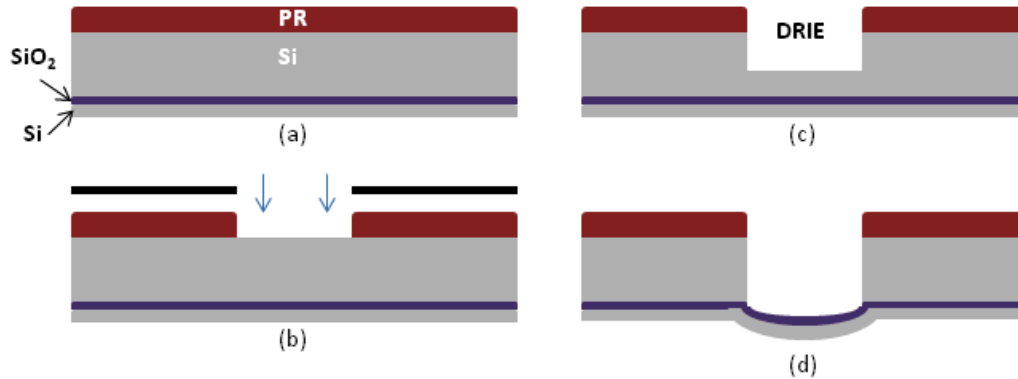


Figure 28. Backside etch process. (a) initial sample, (b) SU-8 photoresist deposition and patterning, (c) DRIE process, (d) instantaneous membrane buckling upon etch completion.

Upon etch completion, the masking layer for only the resistors on the topside needed to be removed leaving a silicon surface with thin resistors. Traditionally, “Scotch® tape” is used to lift-off a majority of the excess gold and photoresist. Again, the fragility of the membranes complicates post processing. The adhesive forces from Scotch® tape fracture the membranes, so an acetone ultrasonic bath followed by a five minute soak in 1165 stripping agent was used to remove the photoresist and gold (Figure 26 d). As a result, only the gold deposited directly on the silicon remained. The finished devices were now ready for testing. Prior to testing, however, a simulated model needed to be developed as a basis for comparison.

Finite Element Methods Process

The basics of FEA modeling were briefly described in chapter two. This section extends the description by detailing the methods by which the membrane was simulated using CoventorWare®. Two primary processes are addressed in this section: *mesh convergence study* and *solver methodology*.

Generating an Appropriate Mesh (Mesh Convergence Study)

In order to have confidence in a model, the mesh must be analyzed in what is known as a mesh convergence study. If the dimensions of a finite element are too large, the program will provide unreliable results; however, if finite elements are smaller than necessary, computational time will be wasted on unnecessary precision. The essence of mesh design is moderation, and in the famous words of Albert Einstein, “Everything should be made as simple as possible, but not simpler” [64].

Beginning with a completed solid model of the membrane, harmonic analysis was subsequently conducted using a variety of mesh sizes. In this study, CoventorWare’s “Harmonic Analysis” feature calculated the modal frequency of the plate. The natural log of the harmonic results was graphed with respect to the inverse of the amount of elements. Known as Richardson extrapolation method, and graphically shown in Figure 29, the results were curve fit, and the y-intercept was interpreted as the location of infinite mesh refinement [65].

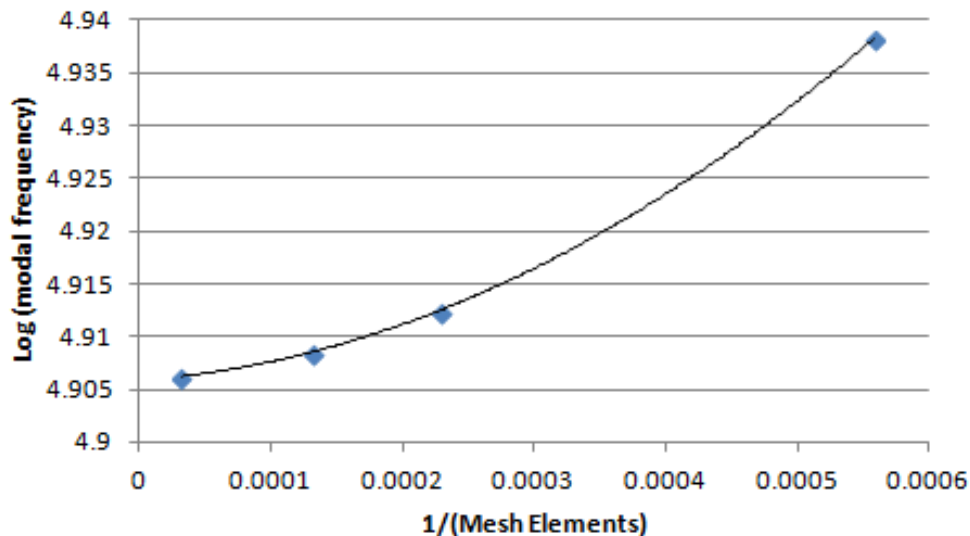


Figure 29. Four separate sized mesh models and their respective modal frequency.

This value was presumed to be the actual modal frequency, and was compared to the modal frequency at a particular element size to estimate the accuracy provided by each element size. The user decides on the amount of acceptable error in a project and select a mesh with the appropriate amount. For the membrane used in this research, a linear Manhattan rectangular block mesh with element size of 30 μm , 30 μm , 1 μm (x,y,z) was calculated to have an approximate error of 0.63% while still maintaining a low computational time. Table 1 lists element sizes and error estimations.

Table 2. Mesh element size with the corresponding modal frequency and error measurement.

Mesh Element Size	1 st Modal Frequency (Hz)	Corresponding Error percentage (%)
Infinite Mesh size	80500.76	0
100 μm	113502	40.9
60 μm	86738.38	7.7
40 μm	81743.05	1.5
30 μm	81011.84	0.6
15 μm	80572.59	0.089

Simulating Buckling

With the appropriate mesh selected, the design was prepared to simulate buckling behavior. A 240 MPa compressive stress was applied to the oxide layer and a 5 MPa tensile stress to the device layer in the material properties editor [5]. The MemMech solver handles mechanical motion and loading, further, the solver was set to nonlinear physics. In the advanced options tab, the initial increment is reduced from 1 to 0.01 to help the solver converge on a solution. The edges of the plate are fixed, and CoventorWare® simulates the membrane as a defect-free, homogeneous material which results in an unperturbed buckled state shown in Figure 30.

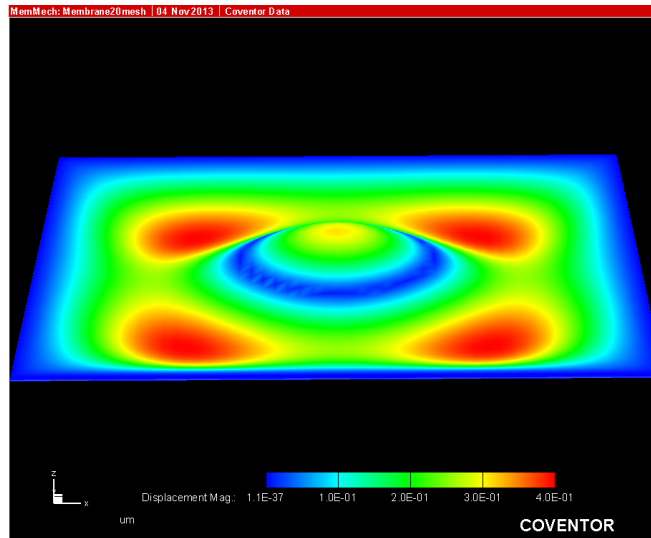


Figure 30. Unperturbed, non-equilibrium buckled state.

In order to “nudge the table” a small transverse load is applied in order to transition to the first buckling mode [65]. Unfortunately the transverse load itself caused deflection in the membrane, and further simulation was performed using CoventorWare’s restart feature. Using the initial result paired with a nearly zero applied load ($<10^{-10}$ MPa) enabled the membrane to “relax” into the real buckling position. Figure 31 shows the change in membrane profile between the “transversely-loaded” and “relaxed” state.

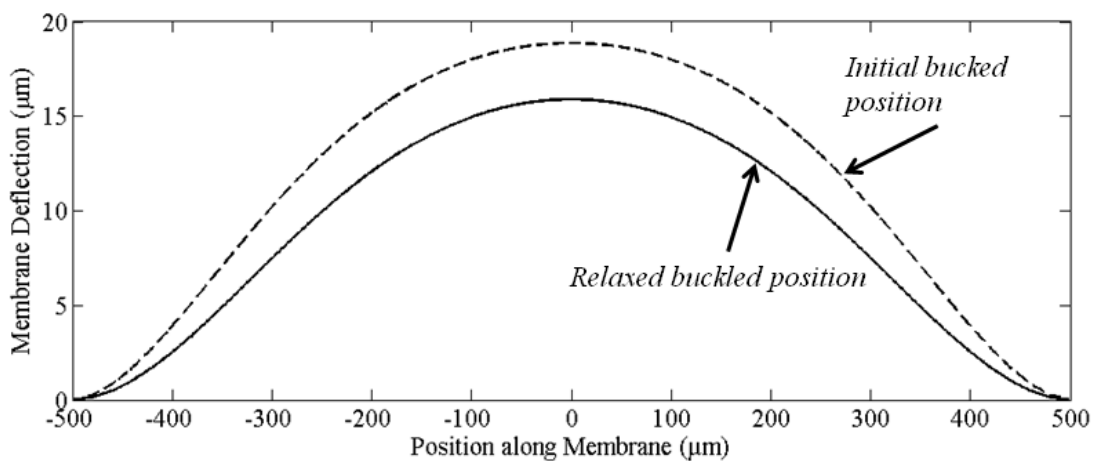


Figure 31. (Dashed) initial buckling with applied load to “nudge the table”, (solid) relaxed buckled state.

From this result, different testing conditions were applied to study the impact on the membrane. Initially, a series of temperatures were applied to the surface of the membrane to enable a first order estimation of the expected behavior. Small changes were made to the simulation setup and simple models were initially used. Simplifying not only ensures computational times are reasonable, but also it helps to identify errors.

The electro-thermal characteristics of the resistor were also simulated to understand how the membrane heated with added electrical power. Initially, voltages were applied to the probe pad surface, but they simulated excess current to flow through the resistor. Experimental testing utilized an electrical probe to contact the pad, which reduces the contact with the pad and increases the resistance. The probe tip is therefore introduced into the model as a $10\mu\text{m} \times 10\mu\text{m}$ layer of gold on the pad where the voltage can be applied. This reduced the overall temperature in the membrane to more reasonable levels.

The primary goals of FEA simulations were to estimate buckling behavior, predict buckled deflection change with applied heat, and to predict the heat profile for different voltages. Together, these results supplied the foundation with which to compare experimental data. The next section discusses one method of collecting experimental data, the load/deflection test fixture. This fixture was used as the cornerstone for the overhanging cantilever testing.

Test Fixture for Load/Deflection Measurements

The membrane was experimentally tested using a test fixture configured to record load and deflection data. The test fixture itself includes a movable stage which positions

a micro Newton force sensor using micro manipulators. Once in position, a voltage regulated piezo electric motor controls the small step movement of the force sensor during testing. The entire system is housed within a Plexiglas container allowing for a nitrogen controlled environment. The test fixture, pictured in Figure 32, allows a sample to be placed in the sample carrier on the right side, while the force sensor is manually moved close to begin testing [77].

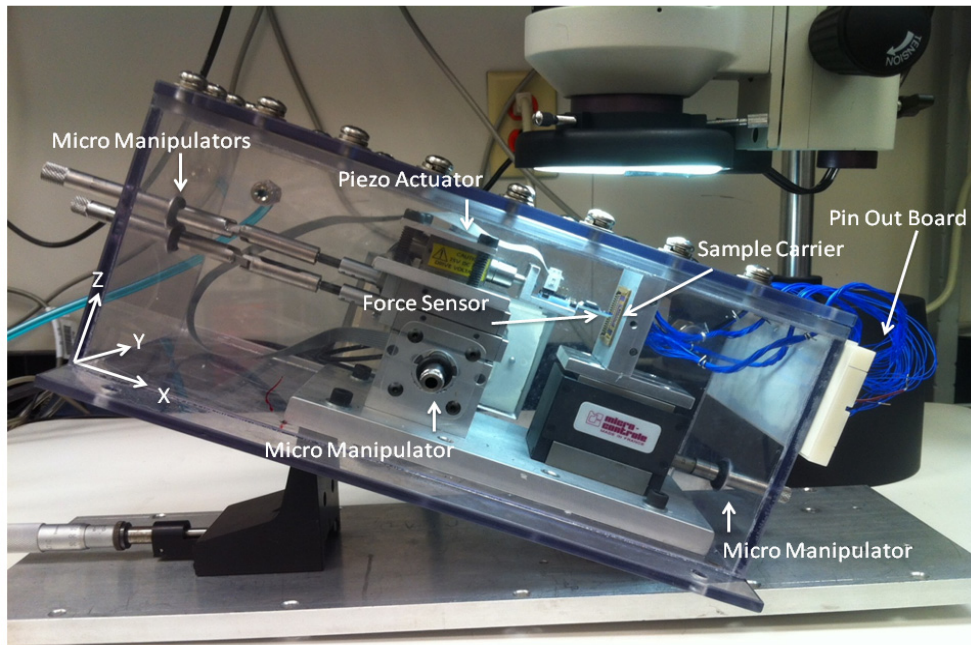


Figure 32. Test fixture with appropriate components listed. Micromanipulators are used for coarse adjustment, while the piezo actuator controls small displacements [77].

The box was angled enabling close observation of the sample through a microscope. Input voltage to the piezoelectric motor and the force data were controlled through Labview, a software program integrating several pieces of equipment and performing data collection.

When testing, the program allows us to specify the step size of the piezoelectric motor and the maximum sensor force which will trigger the program to end. The force sensor is rated to a specified maximum force load, and should the force sensor undergo loads above this value, it will break. The resultant data, force readings, are recorded at each step by the force sensor.

Additional testing methods were required to test the thermal actuation method to modify the stiffness of the membrane.

Experimental Methods

Several testing methods were utilized to characterize the behavior of the thermal membrane actuators. Experimental data can be compared with the model to understand similarities and differences. While load/deflection data was used to verify spring behavior, the following experimental methods tested the resistive heating and actuation abilities of the membrane.

Zygo[®] Optical Surface Profilometer

Immediately following fabrication, device deflection was measured using a white light optical interferometer (Zygo[®] optical surface profilometer). This device nondestructively reflects light from the surface of the sample and quantifies surface roughness, step heights, critical dimensions, and other topographical features [78].

High fidelity, three dimensional computer generated images are produced with appropriate light intensity combined with proper table alignment. Zygo[®] results are displayed as three dimensional depictions of the structure, cross-sectional plots of the surface, and data files of heights and lateral distances. Additionally, the Zygo[®] is

equipped with micromanipulator probes enabling DC voltage to be applied while deflection measurements are taken.

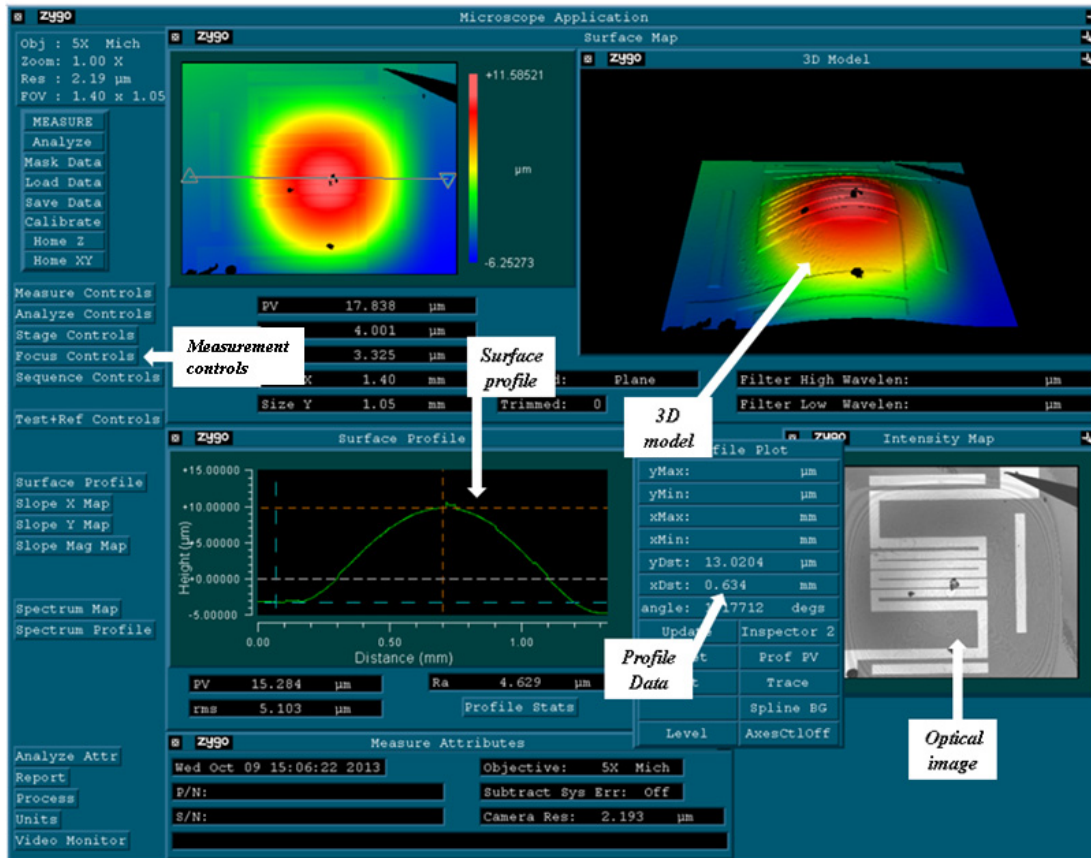


Figure 33 shows the (a) three dimensional rendition of the membrane deflection, and (b) the cross-sectional surface profile.

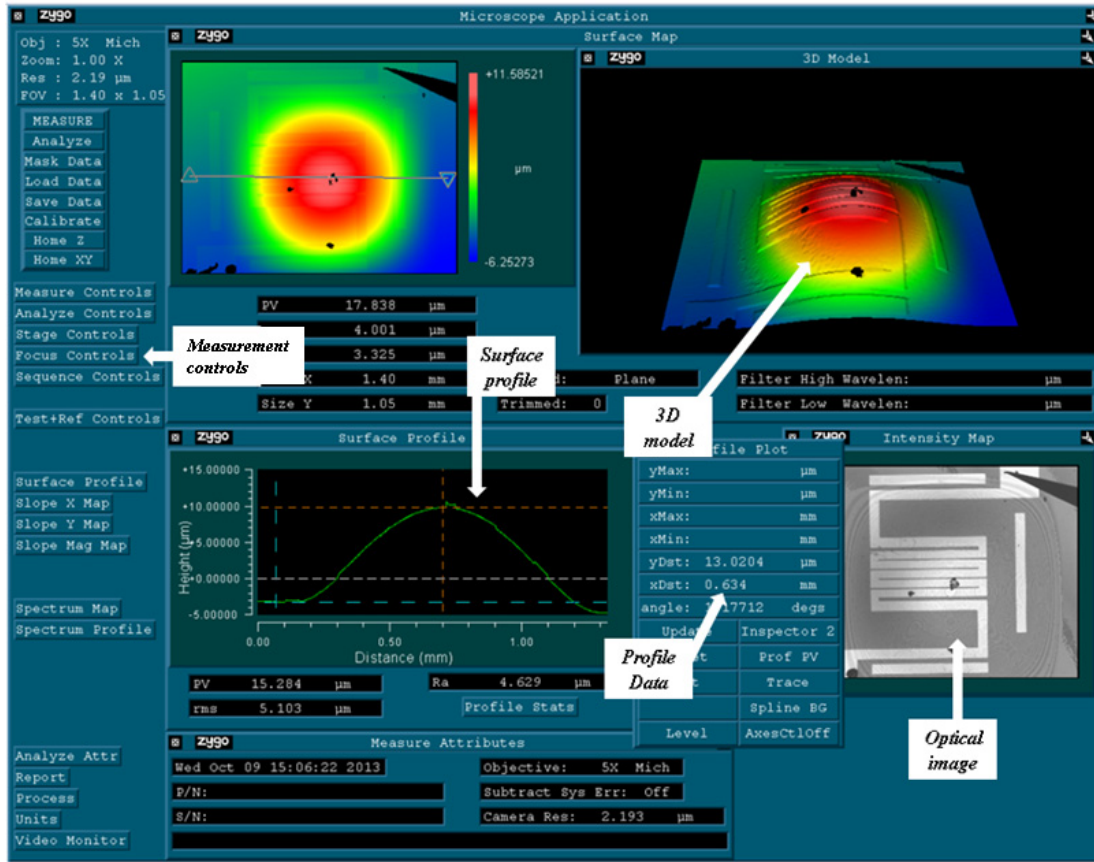


Figure 33. Zygo[®] user interface screen. User controls the measurement with the controls on the left. The optical image is used for fringe alignment. The profile data, 3D model, and surface profile are results from the machine.

In the earlier stages of this research, Zygo[®] testing was used to verify the buckling characteristics of the membrane, while later testing was used to measure membrane deflection with resistive heating. It was also used with the displacement reducing cantilevers to understand initial deflection distance and buckled equilibrium position (buckled in or buckled out).

Thermal Probe Station

A second type of testing sought to understand the thermal characteristics of the membrane's resistive heating capabilities. AFIT's thermal probe station is equipped with a thermal infrared (IR) camera to capture infrared images of a device. Additionally, an

optical camera is mounted beside the thermal camera to aid in probe placement. A signal generator and a power supply enable thermal testing under both steady state and transient conditions.

The camera can detect temperatures within the range of 0-140°C at the low range setting and 0-300°C at the high range setting. Neither is large enough to capture the complete temperature range that is expected in the membrane, but each provides a visual confirmation of the temperature change associated with different voltages. Pictured in Figure 34, the user interface is shown with major functions highlighted.

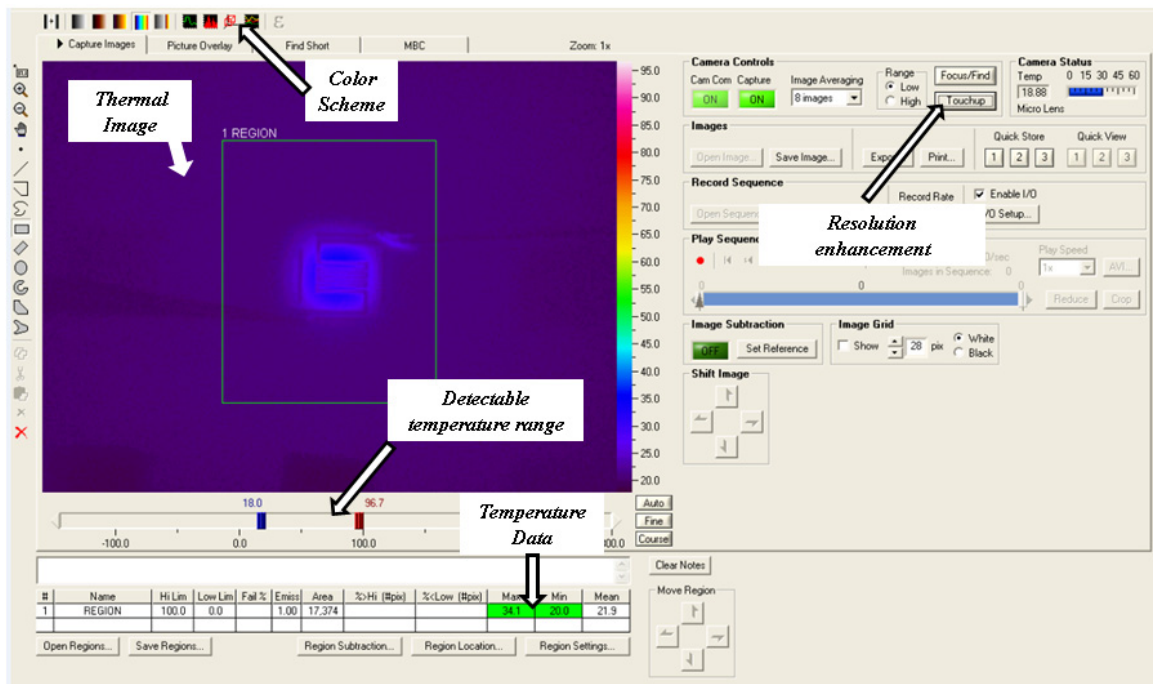


Figure 34. Thermal stage user interface screen.

The images aided in visual inspection of the temperature gradient across the membrane and help to understand the thermal properties of the membrane. The camera was focused properly with the color scheme set to the appropriate temperature range.

Summary

This chapter presented descriptions of the fabrication techniques and testing methods used in this research. The fabrication process requires two masks with two independent procedures. The topside of the sample is patterned in preparation for resistor deposition or cantilever fabrication. This is immediately followed by the backside patterning and development of the etch windows. A DRIE is used to bulk micromachine the handle of the wafer, thinning the sample to the top stacked silicon on silicon dioxide. Device geometries were observed through the use of an optical interferometer (Zygo®). Load/deflection testing was performed in the force test fixture and thermal testing was necessary to detect thermal gradients. Subsequently, CoventorWare® simulations are used to predict experimental data and provide a basis of comparison once the testing is complete. Testing results and discussion are presented in the following chapter.

IV. Results

Chapter Overview

The purpose of this chapter is to present a detailed analysis of the results as were performed according to the research methodology. Analytical calculations and FEM simulations were extensively studied and used as a basis of comparison for the measured experimental data. Equations were used to estimate the degree of buckled deflection and are further modified to consider thermal stimuli. Additionally, these equations can be used to estimate the force required to induce snap-through in the membrane, as well as estimate the change in spring constant as it deflects further from thermal effects. Next, simulations were performed with the express purpose of modeling initial membrane deflection, the heat profile across the membrane under a series of voltages, and the membrane deflection under localized heating. After which, the experimental results are interpreted and discussed.

The goal of experimentation was to develop a method for both actuating and restricting the deflected distance of a Si/SiO₂ buckled membrane thereby modifying the spring constant. The proposed solutions were a buckled membrane with a deposited gold meander resistor and overhanging cantilever beams, respectively. Two resistor styles were used for actuating the membrane and were DC tested with voltages ranging from 1-5V and 1-6V, respectively. Voltages higher than this caused failure in the resistor. Data was collected using an IFM to measure deflection and a thermal camera to measure the temperature profile. Membranes with cantilever beams were also tested using an IFM to measure displacements, and a force/deflection test fixture to measure the spring behavior.

Analytic Modeling

Chapter 2 discussed the equations used to predict the behavior of the membrane during buckling and with applied thermal loads. Additionally, the force/deflection characteristics were estimated for the thermally actuated membrane and the membrane with movement restricting cantilevers. By entering values for material properties, the equations were tailored to the specific scenario and provided a close prediction of the membrane's physical behavior. Determining accurate material properties of the structure for use in the equations can be difficult and can greatly influence the results. In this research, Young's moduli for crystalline silicon and glass, 170GPa and 85GPa respectively, are considered to lie within the "bulk" category of film thickness and are well understood. Also, the dimensions of the membrane and thicknesses of the layers are assumed to be within 5% of the expected value because of accurate and well known deposition and foundary processes. That leaves two factors which determine the accuracy of analytical modeling, the internal residual stress values and the bending effect caused by the resistor. Recall from earlier that the residual stress values are expected to be 240 MPa, but values between 300 MPa and 400MPa have also been witnessed. Additionally, the effect from the deposited resistor has yet to be included and will be discussed in the next chapter.

Shown in Figure 35, the relative strain energy resulting from residual stress is shown with reference to the amount of membrane deflection. This plot is similar to what is shown in Chapter 2; however, the energy curves are unique to this particular buckling scenario.

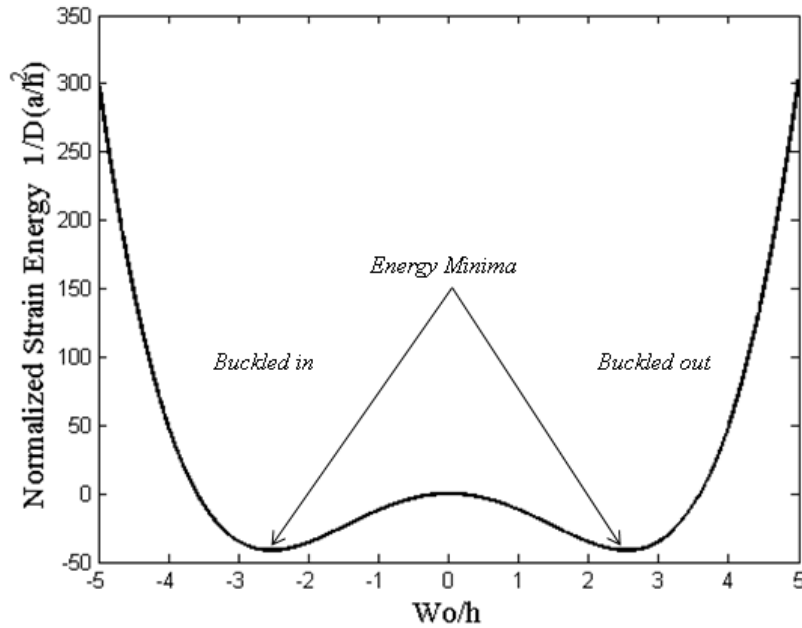


Figure 35. Strain energy of the membrane. Energy minima correspond to locations of predicted deflection.

The minimum y values correspond to a stable equilibrium point to which the membrane is expected to deflect. Since the membrane is buckled, low energy states exist for both the buckled in and buckled out states. The x-axis indicates the degree of out of plane displacement corresponding to these energy minima. The displacement is in terms of out of plane deflection with respect to the thickness ($7\mu\text{m}$), so the model predicts an out of plane deflection of just under three times the thickness. This corresponds to a buckled deflection of approximately $18\mu\text{m}$ in either direction.

By introducing thermal stress into Equation 8, Figure 35 can be modified to include the effects of a temperature increase in the membrane. Figure 36 shows this effect with each strain energy curve signifying a 100 K temperature increase. With successive temperature increases the change in deflection is reduced, which is as expected by literature [68, 71].

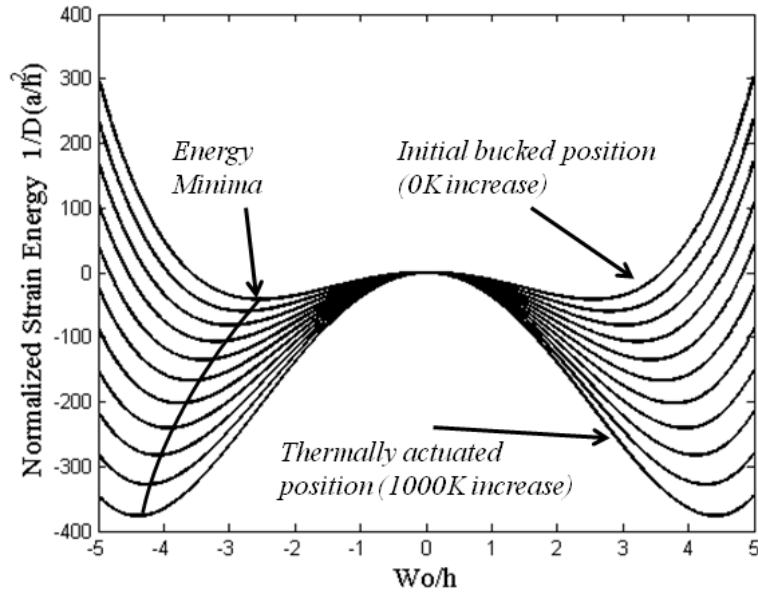


Figure 36 Strain energy curves for a successive, 100K temperature increase in the membrane.

Since the low energy states mark the location of membrane deflection, the minimum of each strain energy curve can be extracted and graphed with respect to temperature, shown in Figure 37.

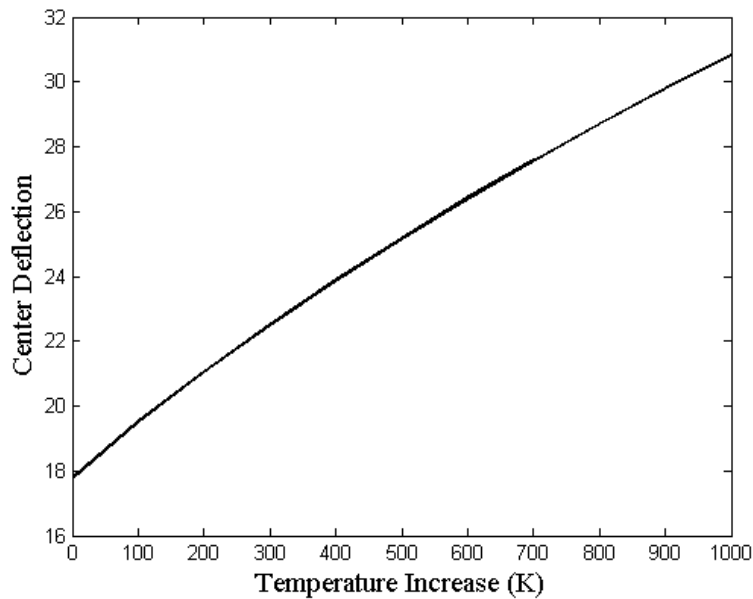


Figure 37. Analytically determined membrane deflection with increased temperature.

This result more accurately illustrates the progression of center membrane deflection with added temperature. From the graph, it should be noted that the model predicts membrane deflection to range from just under 18 μm to just over 30 μm of deflection. Later, this result will be compared to simulated and experimental data for agreement. The results from the electro-thermal simulation will be applied to the analytical equations to establish a connection between voltage and temperature.

Results of Simulation Scenarios

Computer aided simulation was used to model the behavior of the membrane and complement the analytic calculations. To ease the computational load, three simulation schemes were utilized. These include membrane buckling, thermal actuation, and resistor heat performance. Additionally, a modal analysis was conducted on the membrane to understand the mode frequencies and shapes. These results are shown in Appendix C. Finally, the three independent simulations were combined into one model closely resembling the actual experimental condition.

Simulated Membrane Buckling

To model the membrane behavior, several assumptions were employed to reduce complexity. Although bulk material surrounding the membrane strains during buckling, only the area of the membrane was modeled and the edges were fixed, which effectively increases the stiffness. The physical structure was considered homogeneous and free of defects, and was formed from exactly 5 μm of Si and 2 μm of SiO₂ with an internal load of 240 MPa in the oxide layer. The Manhattan linear mesh algorithm was used for

defining the mesh. Since the geometry of the membrane is simple with no geometric disparities, extruded algorithm would yield the same result in this case.

After the device was meshed in the preprocessor tab of CoventorWare®, it was simulated for buckling. The initial simulation result with no thermal stimulus is depicted in Figure 38, which is color-coded to indicate variations in height.

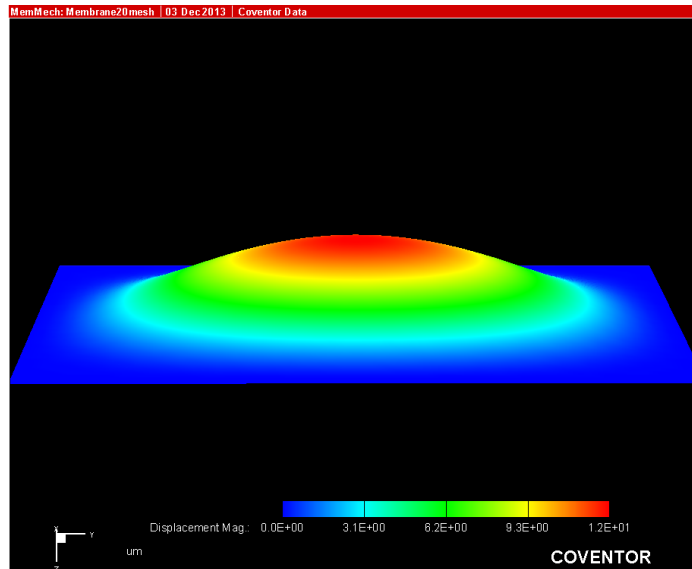


Figure 38 Initial membrane buckling determined by FEA.

It is important to note that this result predicts an initial membrane buckling of approximately 12 μm .

After assuring this analysis was performed correctly and yielded repeatable results without diverging, temperature effects were introduced to the model. The temperature effect was modeled by applying a constant temperature to the surface of the membrane. The simulation began at the post buckled state, and converged to a new equilibrium state as a result of the thermal effects. In Figure 39 the cross-sectional membrane profiles are displayed showing how the membrane deflection rises with increasing temperature.

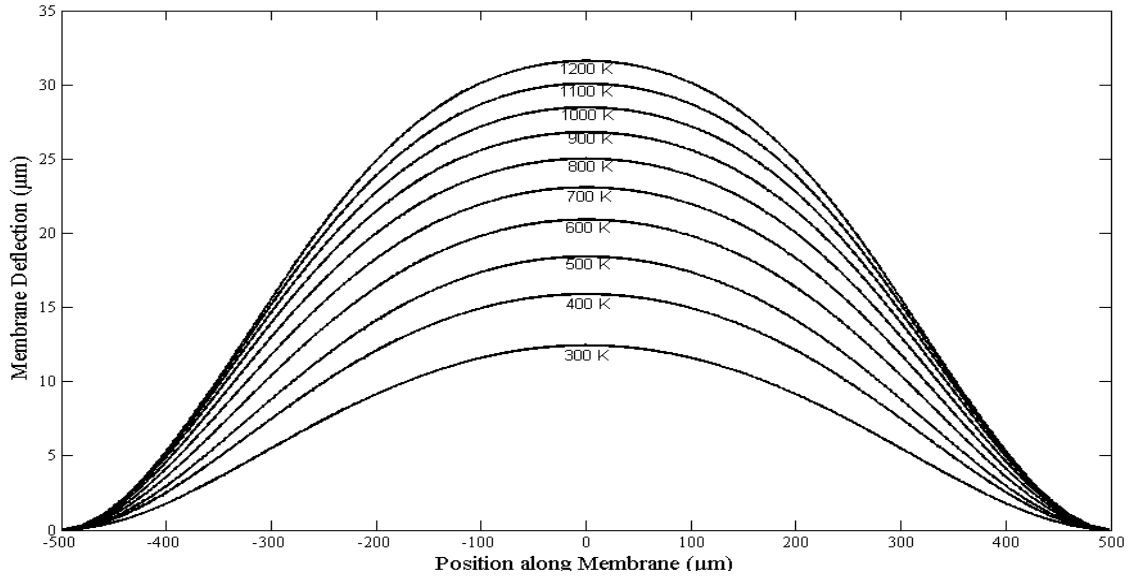


Figure 39. Cross-section of the membrane with increasing temperature predicted by FEA.

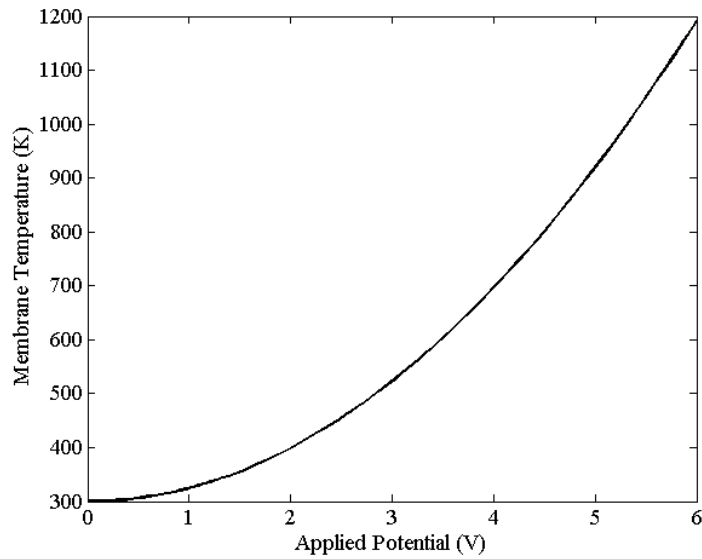
Each line corresponds to a 100 K temperature rise in the membrane with the maximum temperature at 1200 K. The simulation indicates that the membrane will actuate between approximately 13 μm and 32 μm . The trends predicted by the simulation agree with the results of the analytical equations, in that as the temperature is increased, the change in deflection is reduced.

Electro-Thermal FEA

It is important to explore how the thermal effects are influenced by an applied voltage on the resistor. Analytical equations can easily estimate the resistance and electrical behavior, but are less meaningful for the thermal analysis because of a vast amount of assumptions, witnessed by previous research [27]. Additionally, experimentally determining the exact thermal temperatures is not reliable since the limit on the thermal probe stage is 300°C, it has not been calibrated recently, and silicon

emissivity is not constant. As a result, Coventorware's electro-thermal analysis was primarily used to understand these effects.

Simulations of this nature are better understood and are less computationally sophisticated, which indicates the results are of high fidelity and accurately represent the situation at hand. The maximum temperature results of the simulations are collected and



plotted. Illustrated in

Figure 40, the temperature rise in the membrane is shown with respect to applied voltages to the resistor.

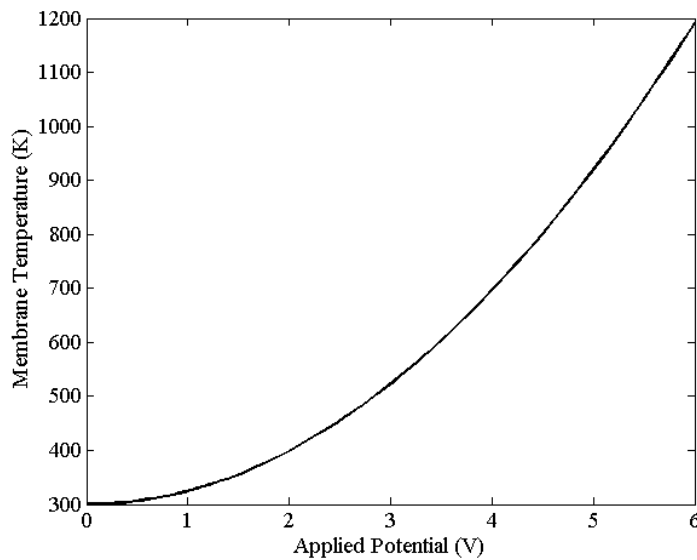


Figure 40. Modeled membrane temperature with respect to voltage applied to the resistor.

The simulations predict a temperature rise to 1200K, which corresponds to an applied potential of 6V. These results apply only to the first style of resistor used in this research. Other resistor types are likely to have different heating profiles depending on the amount of power dissipated through the wire.

Visually, the thermal gradient on the membrane is shown in Figure 41. During simulation, the edges of the membrane are set to room temperature to approximate the behavior of the surrounding bulk substrate. The ideal scenario would be to model a section of the bulk substrate itself, but that would demand excessive computational effort and would likely yield a similar result. During thermal imaging, it is expected that the membrane temperature gradient will be sharper and closer to the edges of the membrane to account for bulk substrate heating.

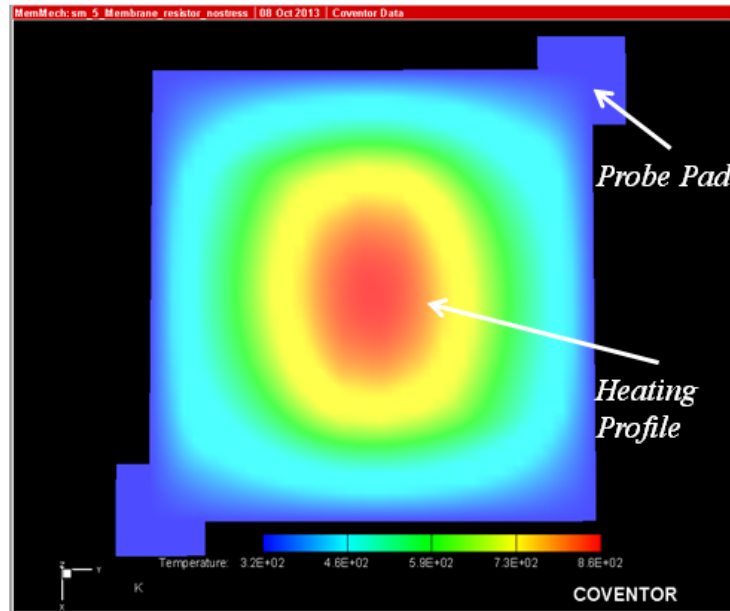


Figure 41. FEM simulation results show the thermal gradient with an applied voltage of 5V.

The final objective of the simulations was to establish a connection between joule heating and membrane displacement. Pairing the data from Figure 40 with the corresponding deflection curve in Figure 39, a model was established for the applied voltage to the membrane. The resultant data can be seen in Figure 42, in which each voltage is paired to a specific deflection from the relaxed position.

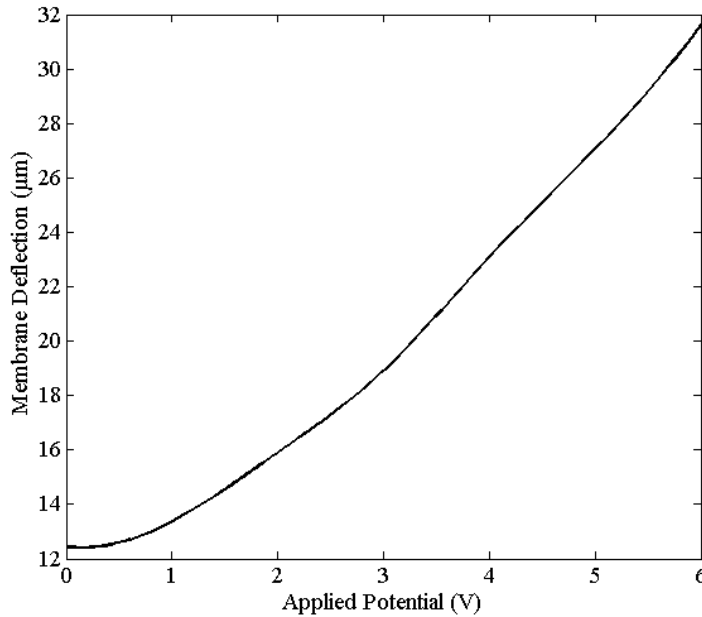


Figure 42. Simulated deflection under various applied voltages. The temperature collected from the resistor simulations was used with the deflection simulations to estimate deflection at each voltage.

The curve resembles that of Figure 40 as a result of the exponential heating behavior of joule heating. However, upon closer inspection, the curve is slightly shallower owing largely to the response seen in Figure 37 and Figure 39 where incrementally increasing the temperature caused a smaller change in deflection. The deflections associated with a specific voltage are listed in Table 3 for both the analytical equations and the simulations. Furthermore, the analytical equation values for temperature are determined from applying the temperatures associated with each voltage from CoventorWare®.

Table 3. Deflection values for analytical equations and simulated analysis. The values are in microns of deflection.

	0V	1V	2V	3V	4V	5V	6V
Analytics	17.77	18.2	19.5	21.4	23.9	26.6	29.8
FEM	12.4	13.4	15.9	18.9	23.1	27.0	31.6
% Dif	35.6	30.4	20.3	12.4	3.4	1.5	5.9

The end deflection predicted by both methods of simulation are similar, yet the starting deflection and the change in deflection are drastically different for each modeling method. Experimentation will show the true behavior of the device and confirm the accuracy of either method.

Thermal Actuation Experimental Results

After completing simulations and analytical calculations, experimental devices were fabricated for testing. Prior to fabricating usable devices the photolithographic process, etch process, and measurement techniques were studied using expendable samples. After the process was well understood and could be repeated, testable devices were constructed. Actuation was measured under the interferometric microscope and thermal gradients were measured at the thermal probe station.

Actuation Measurements

The completed samples, shown optically in Figure 43 and Figure 44 were prepared for testing under the interferometric microscope to study the actuation behavior. Recall from Chapter 3 that two styles of deposited resistors were utilized for this test. The first, a square resistor consisted of a more basic design and required less time to create in the design software. The simple design allowed for quick fabrication and early testing while more time could be dedicated to the spiral design.

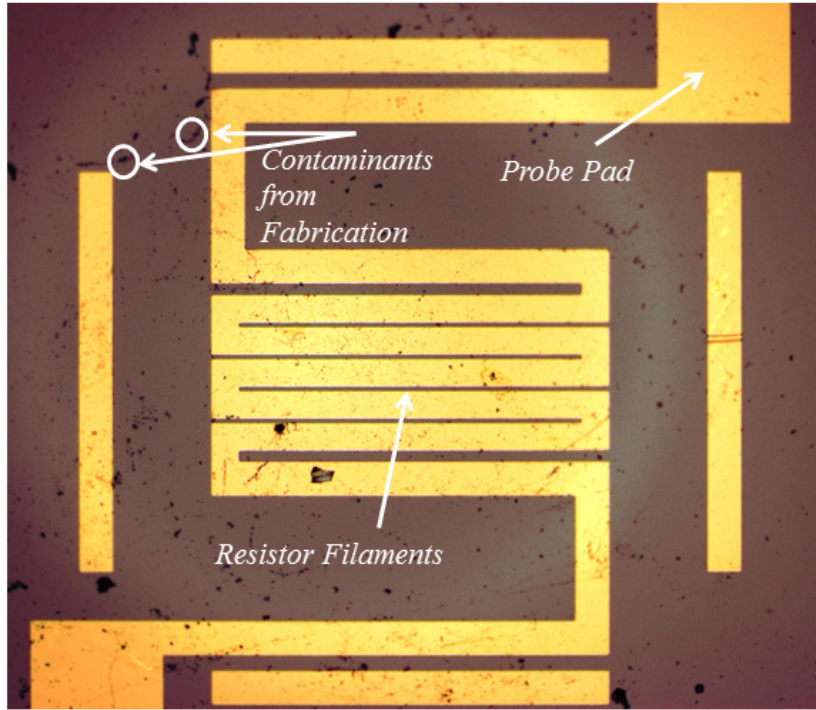


Figure 43. Optical image of the deposited gold resistor located on top of the membrane.

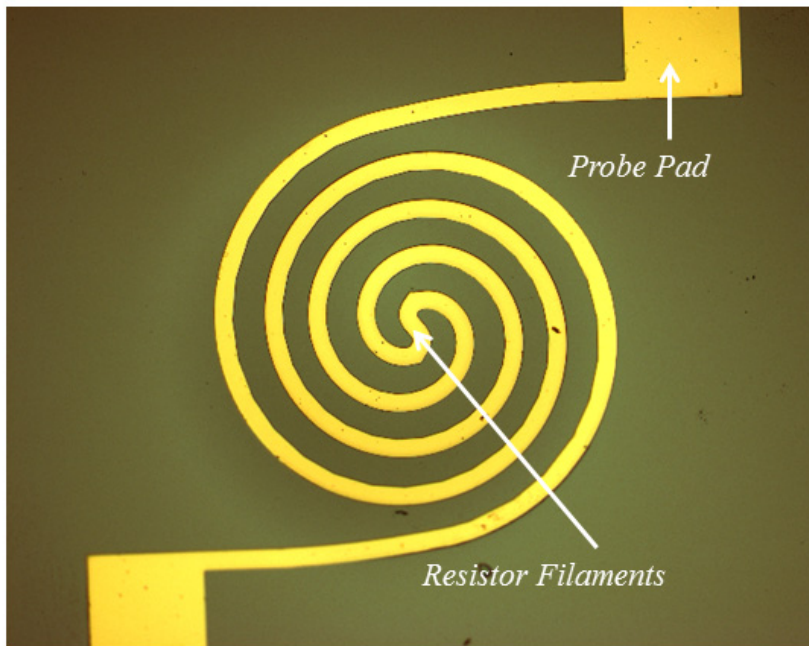


Figure 44. Optical image of the second resistor design.

The Zygo[®] IFM is equipped with movable probes which can be connected to a power supply in order to electrically test micro scale devices. Here, they are connected to a 6V power supply and carefully lowered to the contact pads to supply power to the resistor. However, the Zygo[®] table must first be positioned for optimal focus prior to making contact with the probe tips. Measurements can now be taken by manually adjusting the applied voltage and measuring the deflection in the membrane. The deflections were recorded for each voltage across numerous samples. Figure 45 shows the results of 20 tests with the rectangular resistor style.

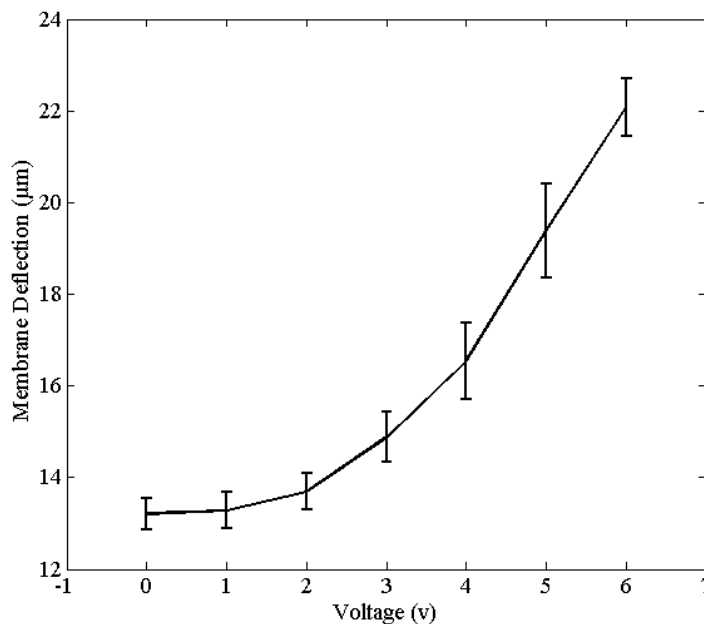


Figure 45. Deflection data for membrane actuation. Vertical error bars indicate one standard deviation of the sample data.

The membrane actuated from an initial deflection of 13.3µm to 22.2µm. The voltage across the resistor had an exponential effect on the temperature, and as a result, the deflection in the membrane. Simulations modeled up to 6V of applied voltage to the

resistor; however, in reality, many rectangular-style resistor samples witnessed catastrophic resistor damage at 6V.

Spiral-style resistors behaved similarly to the rectangular resistor style, in that the deflection increased exponentially with increasing voltage. The spiral resistors, however, remained intact up to a higher voltage. At 8V all devices failed after briefly withstanding the voltage, but they remained reliable up to and including 7 volts. The deflection data for the spiral resistors is shown in Figure 46.

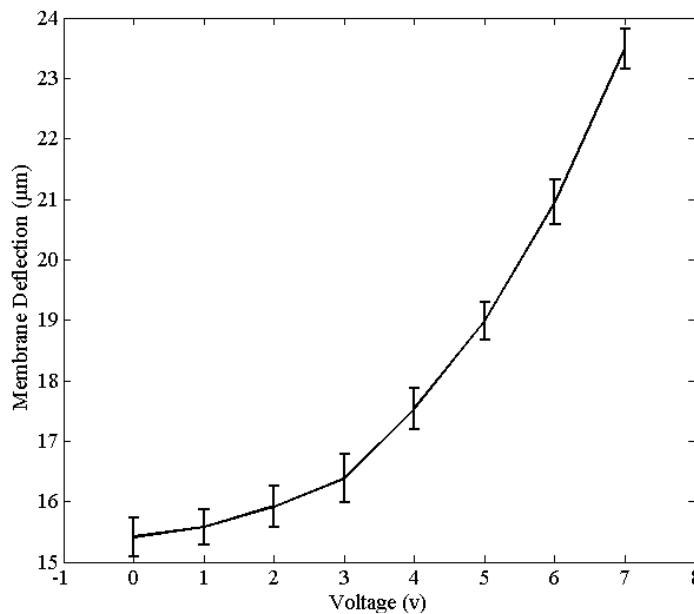


Figure 46. Deflection data for membrane actuation with a spiral resistor. Vertical error bars indicate one standard deviation of the sample data.

The initial deflection was measured to be 15.1µm and the actuated deflection was measured to be 23.5µm. Additionally, the average current through each type of resistor at each voltage is listed in Table 4.

Table 4. Current values through each style of resistor at a specific voltage.

	1V	2V	3V	4V	5V	6V	7V
Square (mA)	32	81	146	194	220	239	-
Circular (mA)	14	33	58	85	104	126	144

Initial displacements of the spiral resistor sample set were slightly higher than the rectangular set. This is likely attributed to the lower volume of gold deposited on top of the membrane. A lower volume of gold supplied a lower returning force against the membrane deflection. Additionally, the spiral resistor actuated to a greater deflection and was generally more robust. The smooth curves of the spiral resistor prevented current crowding around sharp corners, and resulted in less “hot” spots where current could have caused excessive heating and failure.

Samples of both resistor types required a “break in” period in which the current flow and actuation were exceptionally lower than average. For example, a particular resistor might draw 17mA of current with 1V applied. Increasing the voltage to 3V then reducing to 1V would cause the resistor to draw 32mA, the normal amount. It is assumed that by resistor heating and actuation caused a more robust connection was established with the probe tip.

Force/Deflection Estimation using Measure Deflection Data

To reiterate, the purpose of actuating the membrane was to study the force/deflection behavior and how the membrane changes as a spring. We began by attempting to experimentally test the device using the force/deflection testing chamber. The sample was wire bonded into a sample chip and actuated with an applied voltage during testing. Unfortunately, contacting the membrane at the location of heating interfered with the force sensor’s capability to detect a capacitance change, and thereby a force. The force sensor subsequently failed during testing, so testing an actuated membrane was discontinued.

Instead, analytical modeling provides sufficient insight into the membrane's force/deflection characteristics. Using the derivative of the energy equation from Chapter 2 (), the predicted force/deflection characteristics can be graphed. Figure 47 shows this plotted where individual curves correspond to the average temperature at each applied voltage found during experimentation. The equation depends on the ratio of center deflection to the membrane thickness, but it does not use initial deflection as an input. In order to input the initial deflection of the membrane found from experimentation, the stress value used in the equation was modified. An initial stress estimate was used, and then the membrane displacement predicted by the model was verified against the actual deflection values to ensure the curves correspond to the correct amount of deflection.

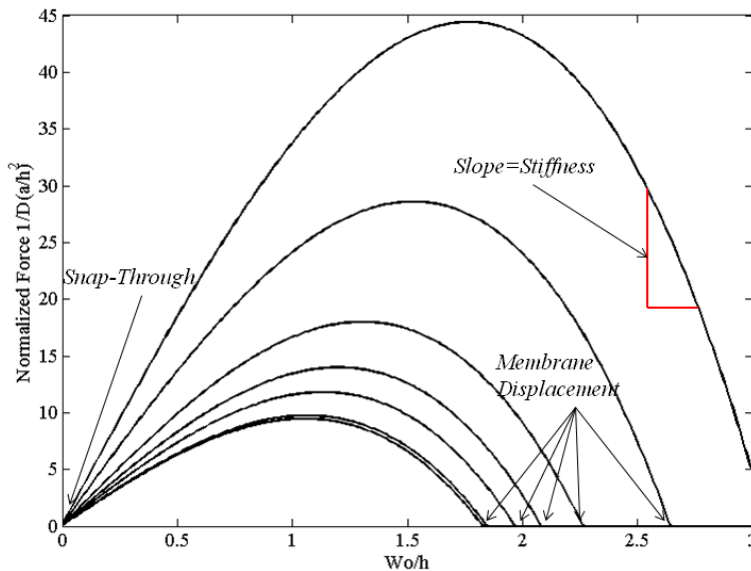


Figure 47. Analytically determined force/deflection behavior. The original membrane displacement is indicated on the x-axis, and the slope of the curves is directly correlated to the stiffness of the membrane.

From Figure 47 we can find the estimated stiffness change between different degrees of membrane actuation. Using Equation 14 from Chapter 2, the negative

stiffness between the non-actuated membrane and the thermally actuated membrane is expected to change from approximately -1.71 to -5.20 normalized force units/ μm . In other words, a threefold increase in stiffness is observed between the non-actuated membrane and the actuated membrane. Furthermore, the total stroke length of complete snap-through actuation of the membrane is predicted to double between the heated and unheated states.

Thermal Stage Testing

The purpose of the thermal testing was to better understand the heating profile in the membrane. The stage is equipped with electric probes, similar to those on the Zygo[®], for testing small electronic devices. The probe tips could be lowered to the contact pads on the membrane, and with an applied voltage, the membrane can be imaged with an infrared camera.

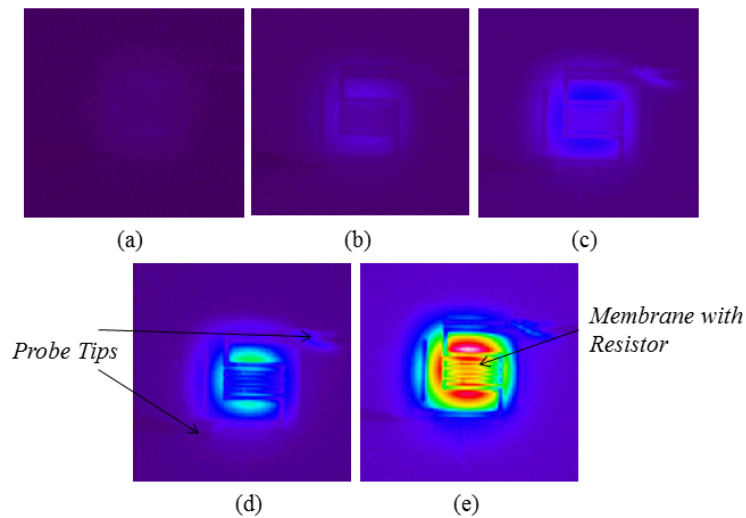


Figure 48. Heating profile of the membrane with successive voltages applied to the resistor. (a)-(e) each represent 1-5V respectively.

The membrane has a peak temperature at the center, with a steadily decreasing temperature until the bulk substrate. The surrounding bulk substrate increases in

temperature a negligible amount. Figure 48 supports the findings of the thermal FEM analysis of the membrane. The two temperature profiles appear similar, but as predicted, the thermal images indicate that the membrane is retaining a higher temperature across a larger surface.

Negative Stiffness Isolation Results

The cantilevers were fabricated atop the membrane in an attempt to restrict the membrane to the negative stiffness region of the force/deflection curve. This corresponds to restricting the membrane from fully buckling. The cantilevers were fabricated prior to backside etching so the membrane buckled into the beams. Initially, optical images were collected to verify the beams remained intact. IFM images were collected to ensure the membrane buckling was reduced and the beams were buckled in the correct direction. Finally, force/deflection measurements were collected to determine if the membrane was constrained to operate within the negative stiffness region.

Optical imaging

Optical images were collected initially to ensure the beams survived the fabrication, and in particular, the etching process. Additionally, scanning electron microscope (SEM) images were collected to observe the final released state of the beams more precisely than through the optical microscope. Figure 49 and Figure 50 illustrate images of the finalized device taken using the aforementioned methods.

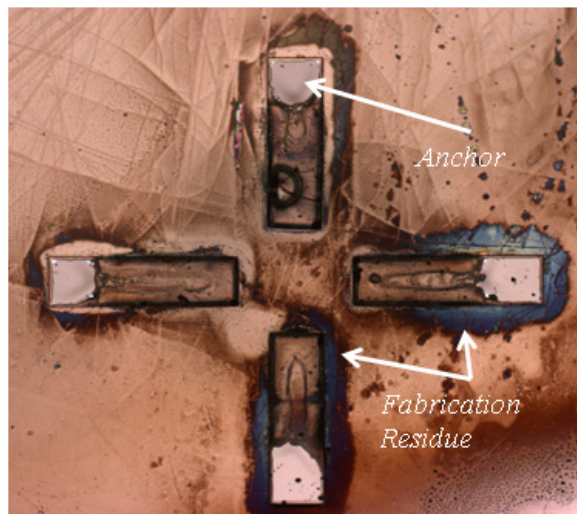


Figure 49. Optical depiction of the SU-8 cantilevers immediately following the backside etching process to release the membrane.

Figure 49 illustrates an item of interest. The background silicon appears to either be heavily damaged or contain large amounts of foreign substance on the surface. We believe this to be a result of the DRIE process, which may cause minor etching of the underside of the sample, as well as leaving a residue from the stabilization oil. To combat this effect, after the etching is finished the samples are carefully cleaned in an attempt to remove this substance. The substance withstood intensive solvent cleaning, and further attempts at cleaning the sample were discontinued because lengthy soaking times in solvents will attack and weaken the bonds at the anchors of the beams.

While the optical images are quick and enable an initial check to ensure the integrity of the beams, SEM images provide a clearer image with the ability to view the sample from an angle.

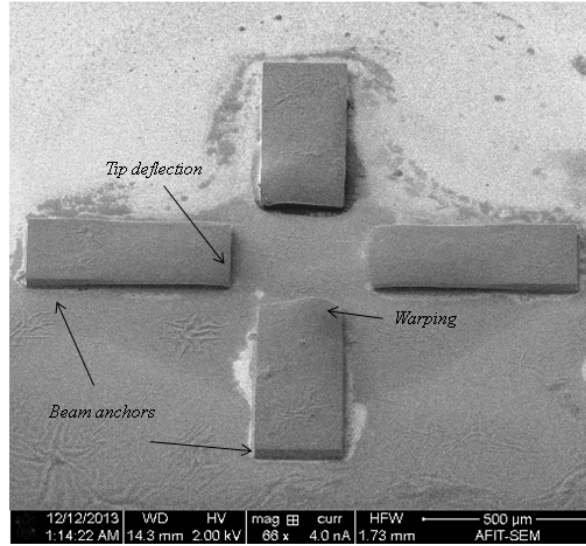
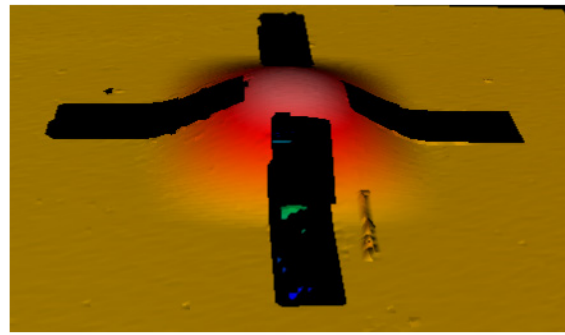


Figure 50. SEM image of the fabricated device rotated to 45°. The four cantilever beams surround the post-buckled membrane. With a 1 mm edge length and a deflection close to 10 μm , the vertical deflection from buckling cannot be observed.

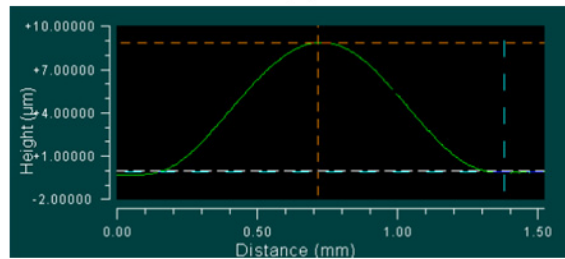
Although the beams appear more structurally sound than the optical image suggests, the beams show signs of stress, most likely induced through the post exposure baking process. The tips are curved down on nearly all of the beams, and some beams show signs of warping and deformities.

Interferometric imaging force/deflection measurements

Prior to force testing, the devices were measured under a white light interferometric microscope (IFM) to measure the deflection of the membrane. Resulting images confirm that the beams restrict the deflection of the membrane. Typically, an unconstrained membrane will deflect 12-14 μm , and IFM measurements indicate the beams restrict the deflection to distances ranging from 7-12 μm . Figure 51 shows the cross-sectional deflection profile of a successfully released membrane as well as the three dimensional rendition of the membrane.



(a)



(b)

Figure 51. Interferometric image of the restricted membrane. (a) The buckling of the membrane. (b) Surface profile of the membrane indicating the buckling deflection.

The featured membrane in Figure 51 is restricted to less than $9 \mu\text{m}$. The vertical direction is exaggerated for effect, and the cantilever beams reflect light poorly, so they appear imbedded in the silicon.

Force/deflection measurements

Further testing, used to confirm the force/deflection behavior of the membrane, was performed using a custom testing chamber. The resultant force data are recorded at each step by the piezo controller, and compiled to generate a load/deflection plot. In Figure 52 the force is plotted with respect to distance.

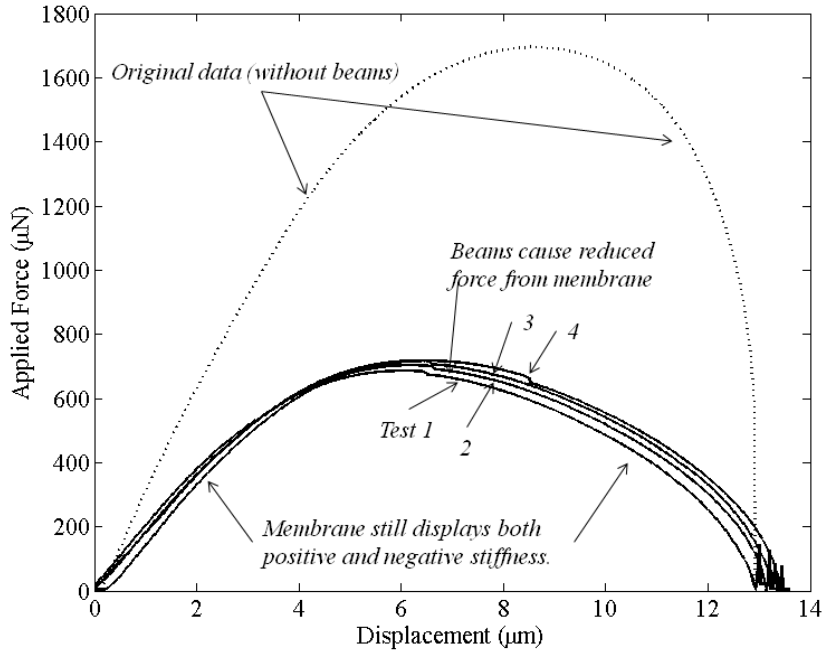


Figure 52. Experimentally determined force/deflection curve.

The plot contains four separate tests conducted on a single membrane with four 200x700 μm restricting cantilevers. The membrane's deflection was reduced from 13 μm to 9 μm by the beams, which was the amount predicted by analytics required for the negative stiffness region; however, according to the results, an additional 6 μm of displacement was required to reach the location of maximum force. Unfortunately, the cantilevers merely reduced the peak returning force in the membrane from roughly 1700 μN to 700 μN . Further observation concluded that the cantilevers reduced the force proportionally to their size, which influences beam stiffness. It is believed that a similar effect would be found from depositing a layer of material over the entire surface of the membrane, which would be stressed upon buckling and aid in reducing the force required to displace the membrane.

The offset of these curves is believed to be a result of the difference in starting locations between the separate tests. Although it is possible the membrane experiences slight hysteresis during actuation along its deflection path.

Summary

This chapter presented the experimental data collected in this thesis research. Modeling and simulation were presented first to illustrate what behavior we expected to observe in the membrane. The analytical modeling estimated the membrane to actuate from a deflected position of 21.7 to an actuated position of 32.56. FEA modeling on the other hand predicted an initial deflection of 12.4 and an actuate deflection of 31.6. Experimental testing measured an initial buckling deflection of 15.1 μm and the actuated deflection was measured to be 23.5 μm for the square meandering resistor, and 13.3 μm to 22.2 μm for the circular resistor. The experimental results were used in analytically estimating the force/deflection characteristics of the membrane spring behavior. By thermally actuating the membrane, the model predicts a threefold increase in stiffness in the membrane. This demonstrates that tuning the stiffness of the membrane using thermal actuation is feasible, and can be useful in applications where a stiffness change during normal device behavior is required.

Force/deflection measurements used to measure the ability of the overhanging cantilevers to restrict the deflection of the membrane were discussed. The purpose was to identify if the reduced deflection in the membrane caused it to actuate in only the negative stiffness region. IFM and SEM images verified that the membrane deflection was reduced by up to 30% and the beams were intact upon release and subsequent

membrane buckling. The force/deflection measurements concluded however, that the membrane was not constrained within the negative stiffness region. The beams simply reduced the membrane deflection by applying a returning force against it. As a result, the membranes showed reduced maximum returning force and a lower stiffness through actuation. In addition, their bistability was lost.

V. Analysis

Introduction

The purpose of this chapter is to analyze several key issues in the data in more detail. While Chapter 4 briefly discussed the results, it only summarizes the analysis for the behavior witnessed during this thesis research. Three primary sections are included in this chapter, model and experimental data comparison, resistor failure during experimentation, and negative stiffness isolation analysis.

Model and Experimental Data Comparison

Membrane modeling was extensively investigated during this research effort. After experimentation, we wanted to understand how the accuracy of the models compared to the experimental data. All three data sources (FEA, Analytical, and Experimental) are shown in Figure 53.

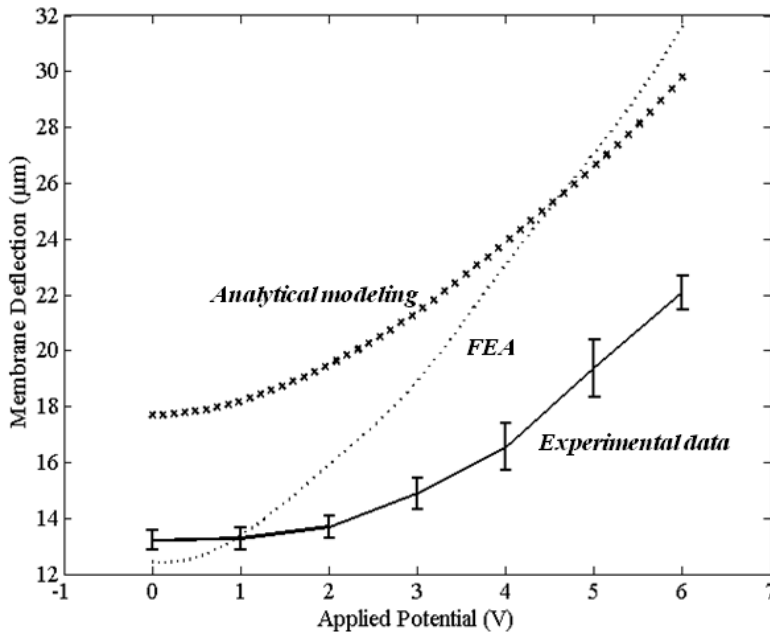


Figure 53. Analytical modeling data, FEM data, and Experimental data.

The figure indicates that both the analytical equations and the FEA predictions are considerably unlike the experimental data. However, FEA accurately predicts the initial deflection position of the membrane, while the analytical modeling accurately predicts membrane deflection trends. FEA modeling underestimates the membrane buckling by nearly 6% at no thermal influence, and overestimates by up to 35% at maximum temperature. We believe there are several reasons contributing to this behavior. First, the initial buckling underestimates the actual deflection because the membrane's edges were fixed during simulation. In reality, the bulk substrate surrounding the membrane would strain and contribute to the overall deflection.

Secondly, the maximum temperature was greatly overestimated because a potential of 6V was applied to the entire probe surface. The actual membrane had a lower pad to pad voltage, in other words, a higher total resistance in the system. Additionally, a physical connection exists between both the voltage source to the probes and the probes to the pads. Voltage is lost in each of these areas, from contact resistance. We attempted to correct this problem after experimental testing by modeling the probe tips on the pads as opposed to assuming a potential over the whole pad. This was accomplished by modeling the probe tip as a 5 μ m x 5 μ m thin (<1 μ m) pad on the surface of the original pad. The result is a lower temperature through the resistor and subsequently a lower membrane temperature shown in Table 5.

Table 5. Comparison between original FEA and modified FEA to include modeling the probe pad.

	1V	2V	3V	4V	5V	6V
Original Design (K)	324	399	522	696	919	1191
Modified Design (K)	300	381	484	627	812	1037
Percent Difference (%)	7.69	4.61	7.55	10.43	12.63	13.82

Lower temperature translated to a lower predicted deflection in the membrane. However, FEA modeling still overestimated membrane deflection at max temperatures. While this change did not fix the overestimation from the model, it helped to partially correct the issue. Other items need to be considered to create a more accurate model.

Analytical modeling consistently overestimated membrane deflection by 30%. There are several reasons for this behavior. Similar to FEA, analytical modeling assumes a fixed end membrane. In reality, the bulk silicon surrounding the membrane would strain and allow membrane edges to displace. Additionally, analytical equations did not model the resistor's effect to membrane buckling. The resistor was deposited prior to membrane buckling, so as a result, when the membrane buckles, the resistor will experience strain and provide a resistance to the deflection.

This effect is perhaps best seen in Figure 54 where the deflection of each style of resistor is shown with respect to voltage. Two important trends are shown in the figure. First, the initial deflection of the spiral resistor is $15.5\mu\text{m}$ and the initial deflection of the square meandering resistor is $13.3\mu\text{m}$. This discrepancy was a result of differences in the volume of gold deposited on top of the membrane. The square meander resistor included a volume of 0.25mm^3 and the spiral resistor included a volume of 0.057mm^3 . This difference in volume contributed to a change in the resistance to deflection provided by the resistor material.

A hybrid model was theorized to compensate for the weaknesses displayed in each model. By first modeling the buckled deflection using FEA, this value would be used in an iterative process to modify the stress parameter in the analytical equations. Once the analytical equations showed an accurate initial deflection, the thermal behavior

could be modeled using the analytical equations. This exploits the accuracy of FEA to model the initial deflection, and the accuracy of the analytical equations to model the stress introduced through joule heating. In effect, analytical equation line from Figure 53 will be translated to begin at the initial deflection location predicted by FEA, also shown in Figure 53.

When comparing the two resistor types, the square meander resistor heated with a lower applied voltage. This is caused by the lower resistance through the resistor. A lower voltage corresponds to a higher current, and subsequently a more rapid temperature increase.

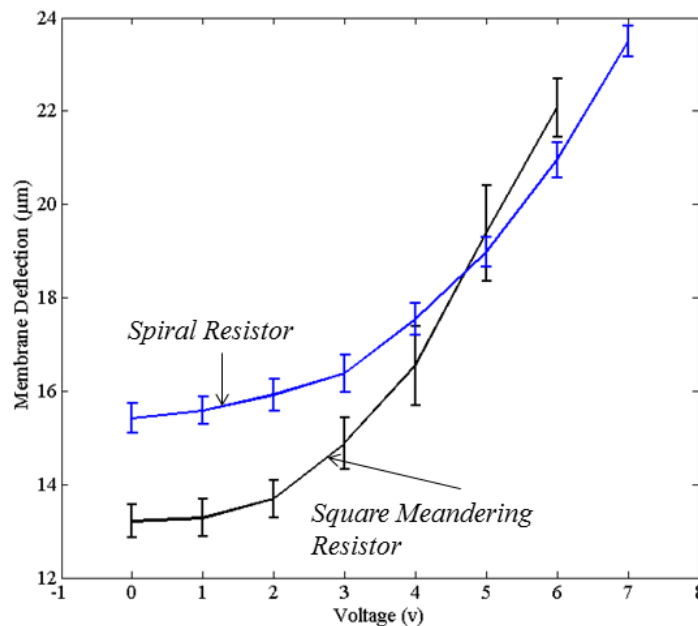


Figure 54. Thermal actuation behavior of each style of resistor.

Resistor Failure During Experimentation

This section discusses the resistor behavior during testing. Primarily, we wanted to address how the resistor failed. The rectangular style resistor failed with applied

voltages at or above 6V. In Figure 55 a failed resistor is shown with the brown region indicating the location of failure.

The failure is not likely caused by the high current and sharp corners around which the current crowds because the resistor did not fail at a corner. Additionally, the circular resistor failed at a lower current value. This indicates that the high temperatures were the reason for the failure. It is well known that the melting point of bulk substrate gold is just over 1300K, which is higher than the maximum temperature witnessed in FEA simulation [79].

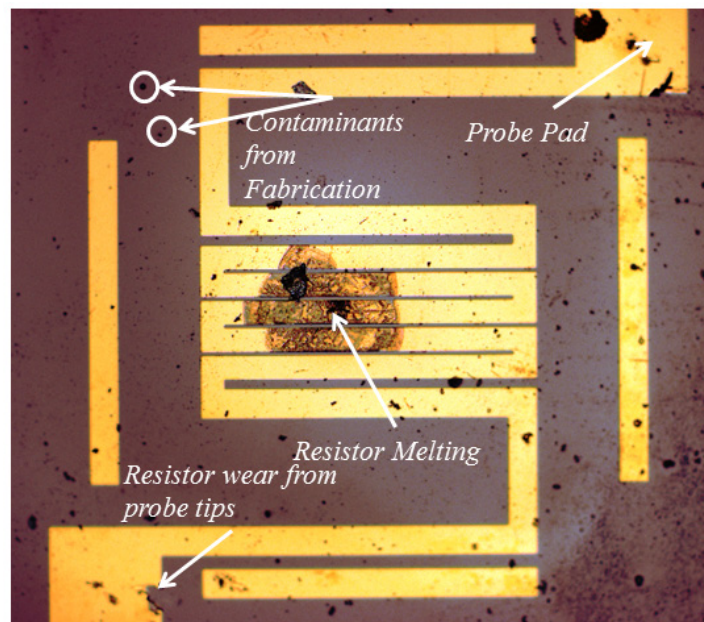


Figure 55. Failed resistive heater. Debris shown scattered around sample is from testing and failure of samples.

However, literature suggests that the melting temperature of gold is lowered as the feature dimensions are reduced. This is a phenomenon known as melting-point depression [80]. Thermodynamic properties of thin films can change drastically with an increase in surface area to volume ratio. This phenomenon is typically applied to

nanostructures, but in this case we believe it applies to our resistor behavior because the thickness of the gold resistor is 300nm. As the samples reach peak temperature in the middle of the device, as witnessed by thermal measurements, the gold near the center is the first to melt. During melting, the melted portion appears to crawl outward until the total area is encompassed.

A similarly failed resistor is shown under the SEM in Figure 56. The failure is caused by the gold seemingly melting, evaporating, and failing to provide an electrical contact between the probe pads. There are also indications of a secondary connection created during this failure which could have accelerated the failure because of intense shorting.

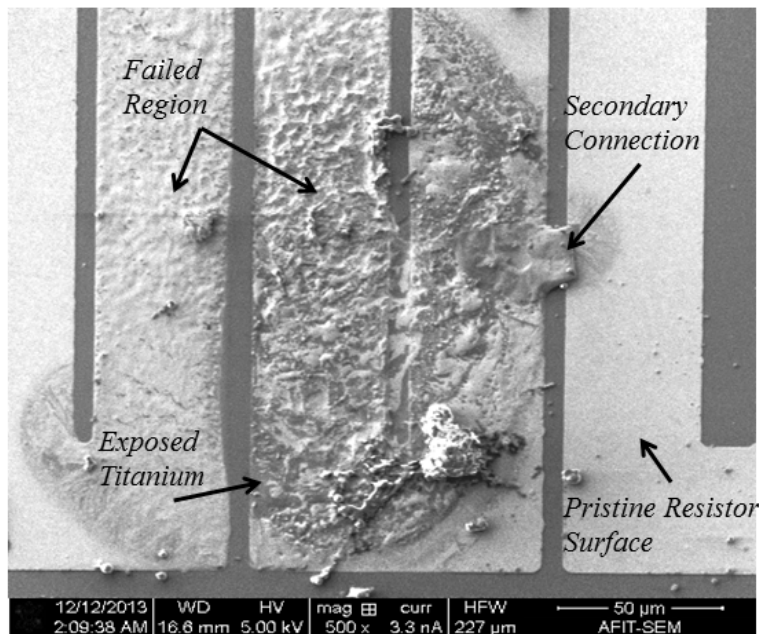


Figure 56. SEM image illustrating the failed portion of a resistor. The gold has been melted and fails to provide an electrical connection between the contact pads. This could be caused by excess heating and the formation of a secondary connection.

It was also discovered that establishing an electrical contact between the probe and the contact pad could be difficult. Adjusting the probe typically solved the issue. This

further indicates that the contact between probe and pad was less than ideal and caused the resistance in the system to be higher than expected.

Negative Stiffness Isolation Cantilever Analysis

Successful fabrication of the device proved difficult at first. Large changes in temperature during the post exposure baking step caused warping and stresses in the beams, reducing the uniformity across separate samples and the effectiveness of the beams. In earlier samples, it was discovered that most of the beams failed to adhere to the substrate following backside etching. The post exposure baking procedure was slightly modified to combat this effect by promoting adhesion and reducing warping. By increasing the temperature ramping time during this procedure using a single hot plate and ramping in intervals of 5°C from 65°C to 85°C, we were able to fabricate a successful sample.

The backside etching process deposited undesired substance on the topside of the device, potentially affecting the performance. Careful solvent soaking was used in an effort to remove the residue. After several lengthy soaks, the residue remained, but the beam anchor interface began showing signs of wear. For fear of destroying anchors, the solvent soaking effort was dismissed. For future samples, a protective coating of photoresist will be applied prior to backside etching. This could help reduce the residue buildup.

Results of this experiment indicate that the membrane needed to be displaced further to be isolated in the negative stiffness region. Additionally, the deflection restriction mechanism (SU-8 cantilever in this case) needs to be as stiff as possible to

prevent it from interfering with the force deflection characteristics. Whatever structure is used to restrict the membrane must only restrict its outward deflection and not add an external force to aid in spring deflection. Ideally this would be a structure with infinite stiffness, which is placed at exactly the correct distance above the membrane to constrain it to the beginning of the negative stiffness region ($9\mu\text{m}$). In the test used for this research, the beams were seated approximately $1.8\mu\text{m}$ above the surface of the silicon. SU-8 has proven to be lacking in stiffness even with the benefit of thick layer heights, unachievable by many other materials. However, multiple layers of sacrificial photoresist under the beam could raise the beam height to the required $9\mu\text{m}$. Additionally, multiple layers of SU-8 could provide the necessary stiffness in the beams.

In Figure 52 the force/deflection behavior changed with the addition of the cantilever beams. Without the beams, the region immediately prior to snap through was short and steep. With the addition of the beams, the total curve is lowered and the region prior to snap through is shallower. Additionally, the membrane had lost snap through behavior. It was observed that upon reaching the snap through region, the membrane still applied a returning force against the force sensor. We believe the beams adhered to the membrane and caused this behavior.

Summary

This chapter discussed and analyzed several key aspects of experimental data. Three primary sections were included in this chapter, model and experimental data comparison, resistor failure during experimentation, and negative stiffness isolation analysis. We proposed reasons for the model's deviation from actual behavior.

Additionally, resistor failure was suggested to occur from excess heating in the membrane. Finally, the cantilever's fabrication and ability to restrict the membrane were analyzed and discussed. If the beams were stiffer and situated higher above the membrane, the membranes could be restricted to the negative stiffness region.

VI. Conclusions and Recommendations

Chapter Overview

Previously at AFIT, a linear regressive spring, in the form of a buckled Si/SiO₂ membrane was developed and tested. This current research focused on developing an actuation scheme to modify the spring constant as well as restrict the spring to the region displaying negative stiffness. The purpose of this chapter is to review the findings of this research and understand potential directions for future research in this area.

Conclusions of Research

The rapidly growing MEMS industry and increased demand for MEMS devices is forcing the industry to come up with unique and creative ways to develop new components. Many inertial sensors could function more efficiently with lower overall stiffness in the restoring tethers. Additionally, microfluidics, in particular microvalves, could benefit from a better valve actuation scheme. This research investigated using a buckled plate formed from silicon and silicon dioxide as MEMS disk spring.

This research sought to address several questions posed in the introduction. The following are the summarized research goals and brief explanation of how they were addressed in this research. First, we wanted to address the foundational mechanics of the buckled membrane. This thesis effort explored the basic mechanics in depth in Chapter 2, along with applications used by other researchers. Next we wanted to determine if there was a model (both computer simulated and analytical) that could be developed to predict the behavior of the Si/SiO₂ membrane. Two modeling avenues were explored for predicting device behavior. Extensive CoventorWare® simulations and analytical modeling were conducted.

A two pronged approach was used for this research. The first element attempted to determine if the membrane could be actuated with a deposited resistor. This was done to modify the spring constant of the device. Experimental testing confirmed that thermally actuating the membrane changed the outward deflection. When compared to the models, the analytical model overestimated the displacement in the membrane. FEA predicts the initial deflection position accurately but overestimated the increased deflection from heating. Although FEA is considered to be nearly as accurate as actual behavior, it relies heavily on the accuracy of the user input. By assuming that the entire probe pad, or even just modeling a 5µm² pad as the probe contact, we overestimated the amount of current drawn through the resistor. Later, the force/deflection test fixture was used to test a thermally actuated membrane, but equipment failure resulted in unreliable data. As a result, membrane deflection data were used in conjunction with analytical equations to estimate the spring behavior of the membrane when it was actuated. These results estimated a threefold increase in membrane stiffness.

Secondary testing attempted to restrict the outward buckling deflection of the membranes by adding cantilevers attached to the surrounding bulk substrate to constrain the membrane. These cantilevers reduced outward buckling deflection by up to 30% but failed to limit membrane deflection to the negative stiffness region. Post experimental analysis suspected that the beams were not stiff enough to limit membrane deflection with beam deflection $< 1\mu\text{m}$. This caused the beams to act as a spring on the membrane and simply reduced the force for transverse actuation.

Significance of Research

- This research led to the development of a novel membrane actuation scheme with the express purpose of modifying the membrane spring constant. Analytical equations predicted a 300% increase in stiffness of the membrane throughout the range of actuation.
- Models of buckling behavior were developed and tested against experimental data. Future research could use these models and make small changes according to what was presented here to yield more accurate results.
- A modified Labview interface was developed for use with the force testing fixture to accommodate single-cycle MEMS regressive spring devices.
- A detailed background in buckling theory and related work was provided to help future research in this area.
- A SU-8 cantilever beam approach was developed to restrict membrane actuation to the negative stiffness region. Realized devices held the

membrane at the desired distance, but did not contain the necessary stiffness to hold the membrane at that location without applying a returning force.

Recommendations for Future Research

Membrane geometry and actuation speed

This research focused on a single sized membrane for actuation testing (1mm²), however, decreasing the size of the membrane could prove useful in practical applications. Size requirements in industry demand small components and a more practical membrane actuator would inevitably be much smaller. An array of devices with decreasing sizes should be a focus for future research. However, as the size of the membrane decreases, the critical buckling thickness will shrink as well, so smaller diameter devices will need to be appropriately thinned to function as desired.

Additionally, future research should investigate the actuation speed capabilities of the membrane. While it is known that the thermal response of similar devices are slow (100Hz) when compared to electrical switching capabilities, the actual limits of the device presented in this research would be useful to understand prior to implementation into a system.

Finally, although the devices performed consistently across a complete sample, adjusting the fabrication process could provide a more robust device. Many devices required a “break in” actuation cycle before they performed consistently through many actuations.

Reliable Force Testing

In order to understand the spring characteristics of the membrane, the force measurement fixture was used. Testing the membrane while actuated was attempted, but current or heat interference from the resistor caused the system to generate unreliable readings. By further investigating the force testing fixture, users will be able to reliably test the force capabilities at all actuation displacements and current values.

Negative Stiffness Restriction

Previous research suggested isolating the spring within the negative stiffness region of actuation. This research presented a possible solution by restricting the membrane using overhanging cantilever beams. Realized devices utilized a cantilever beam fabricated from SU-8 photoresist to apply an ideally infinite restoring force against the membrane at the location where it crosses into the negative stiffness region. When tested, the beams merely reduced the outward deflection and the force from the membrane.

By modifying this method and using a stiffer material, restricting the membrane to the negative stiffness region could be achieved. Multiple layers of SU-8 or a thick layer of metal could be a potential solution.

Summary

This chapter presented the major findings of this research. By actuating a MEMS buckled membrane using thermal stresses, the transverse spring actuation characteristics could be modified. Modeling predicts that the membrane's spring constant could be tripled through thermal actuation. Additionally, a method was developed to isolate the

membrane to actuating in the negative stiffness region. Although, this restricted the membranes outward deflection, it failed to keep the membrane in the negative stiffness region. This research opened several avenues for following research, including membrane actuation speed testing, geometry scaling, reliable force testing, and negative stiffness isolation.

Appendix A: Possible Applications

The purpose of this appendix is to present possible applications of the research. There are three primary areas where this research seems to fit best, and each utilizing the membrane in a different manner.

Vibration Isolation

Vibration isolation seeks to, as the name suggest, reduce vibrations to a specific target area of a structure or device. In MEMS and NEMS precision vibration isolation is critical to preserve structural integrity and reduce physical noise in devices. While, pneumatic, air table, systems are widely used, smaller feature sizes require a more precise vibration isolation system. Negative stiffness vibration isolation can provide this higher precision, and it is created by a vertical spring which supports the weight load combined with a negative stiffness mechanism [81]. This negative stiffness mechanism could be the membrane presented in this research particularly if it can be isolated within the negative stiffness region.

Euler Spring

In the realm of vibration isolation, research has suggested to use Euler springs for vertical vibration isolation. An Euler spring is essentially a buckled beam where the compressive buckling force is applied by the suspended mass. As a result vibrations cause compressive loading beyond buckling. The static energy stored in a typical spring mass system is reduced to nearly zero in an Euler spring and only dynamic energy storage needs to contribute to the spring mass [82]. In a traditional mass spring system where much spring energy is stored as static energy, the spring mass must be large which supports low frequency resonant modes [82]. Euler spring systems contain lower masses

and help to reduce this low frequency resonant mode. In Figure 57, a schematic of a Euler spring system is shown with the mass suspended by the tops of the Euler springs.

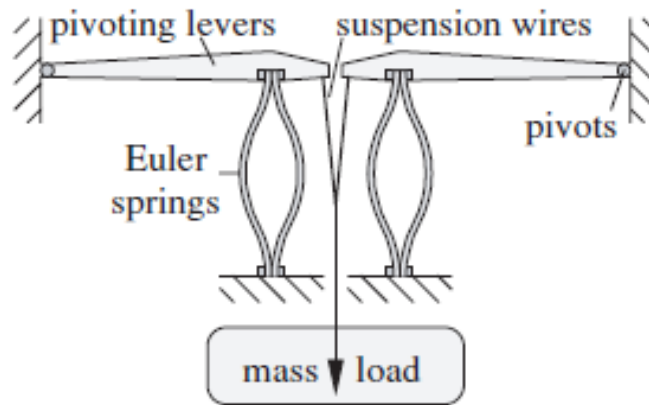


Figure 57. Euler Spring for vibration isolation [82].

The buckled membrane used in this research could be used in this manner for creating a self contained MEMS vibration isolation system. Additionally, the resistor actuation scheme could be used to externally displace the Euler springs and change resonant modes.

Switches and Valves

Valves and switches were discussed in this research as areas where other researchers have used buckled structures. Hälgl fabricated a memory device using a buckled beam and switching between states through electrostatic actuation. This membrane could use a similar device, but instead of switching states with electrostatic actuation, thermal actuation could be used. Arya et al. discovered a way to thermally switch a buckled membrane through a deposited metal on the backside. With heating, the backside metal will expand faster than the silicon and apply a transverse bending force to the membrane [83]. This will result in a state switch. Switching the membrane back to the original state will result from removing the electrical power and subsequent cooling.

Equilibrium switching is not the only way this membrane could be useful. By thermally actuating the membrane as is done in this research, a small deflection switch could be fabricated. An overhanging electrode could be fabricated with an air gap above the membrane. Upon thermal actuation, the membrane could make contact with the switch. Small actuation would be necessary because of the slow actuation speeds characteristic to heating.

Buckled structures for valves could prove particularly useful because of equilibrium positions. Typically, valves will remain open or closed for extended periods of time, and reducing the force required to hold the valve in that position could prove useful. Again, using the membrane with the backside deposited metal could be a method of constructing a novel microfluidics valve.

Appendix B: Mask Design

The purpose of this appendix is to show the mask designs that were used in this research effort. The following mask is used with the resistors.

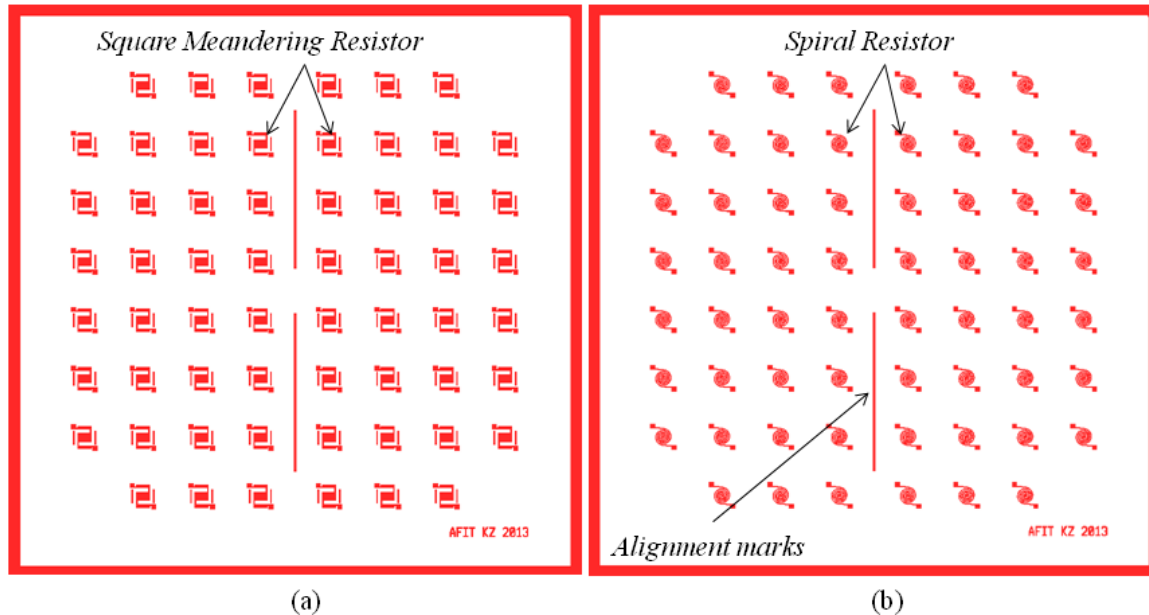


Figure 58. Resistor mask, (a) original resistor design, and (b) revised design.

The next mask is for the anchor holes for the beams. The anchor holes expose the underlying S1818 photoresist to allow the subsequent SU-8 photoresist to make contact with the silicon substrate. This contact serves as an anchor for the cantilever beams. The anchor holes are round to reduce stress in the beam anchors and promote SU-8 adhesion.

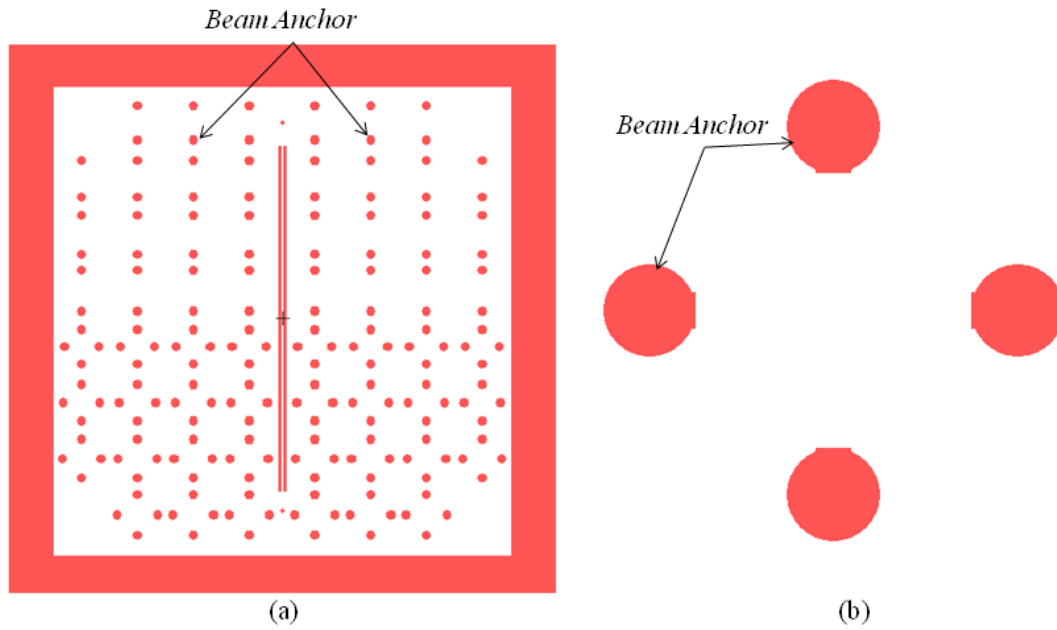


Figure 59. Anchor mask for SU-8 beams. The red areas will be etched in the mask maker, leaving chrome in the red regions.

The next mask shown is the beam mask. This mask is used for exposing the SU-8 beams used for membrane deflection restriction.

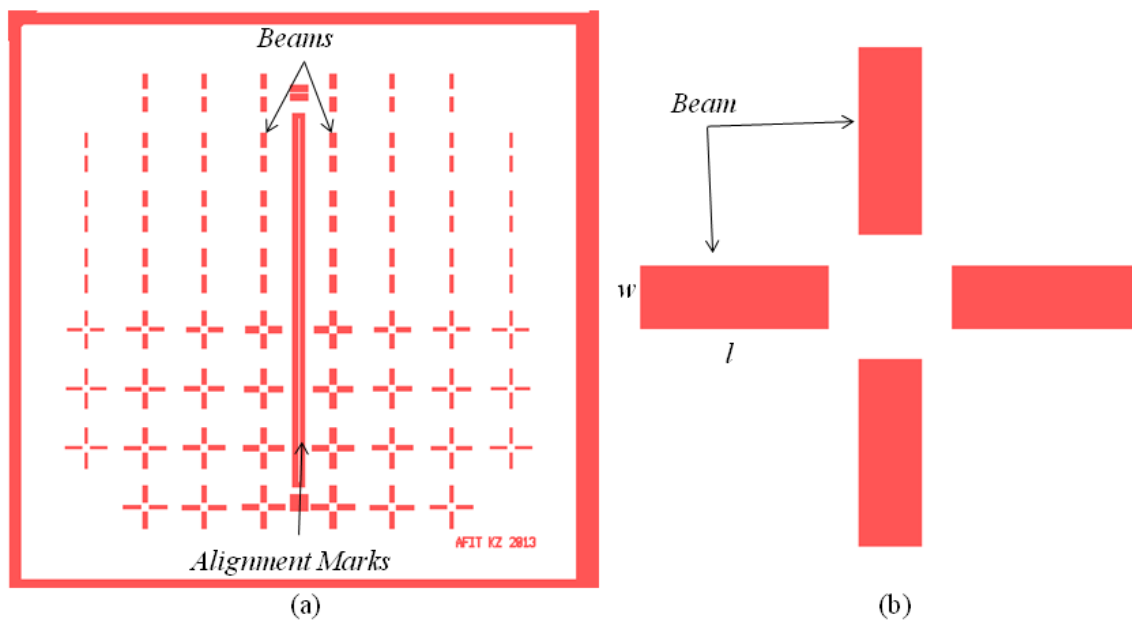


Figure 60. Beam mask for SU-8 cantilevers.

The next mask is for exposing the membrane etch cavity in the SU-8. SU-8 is a negative photoresist, so UV light promotes cross-linking of the photoplastic material in the resist. Because of this, the mask is an inverted design compared to the other masks. The red region will be etched away leaving a mostly clear window, with small chrome squares and circles.

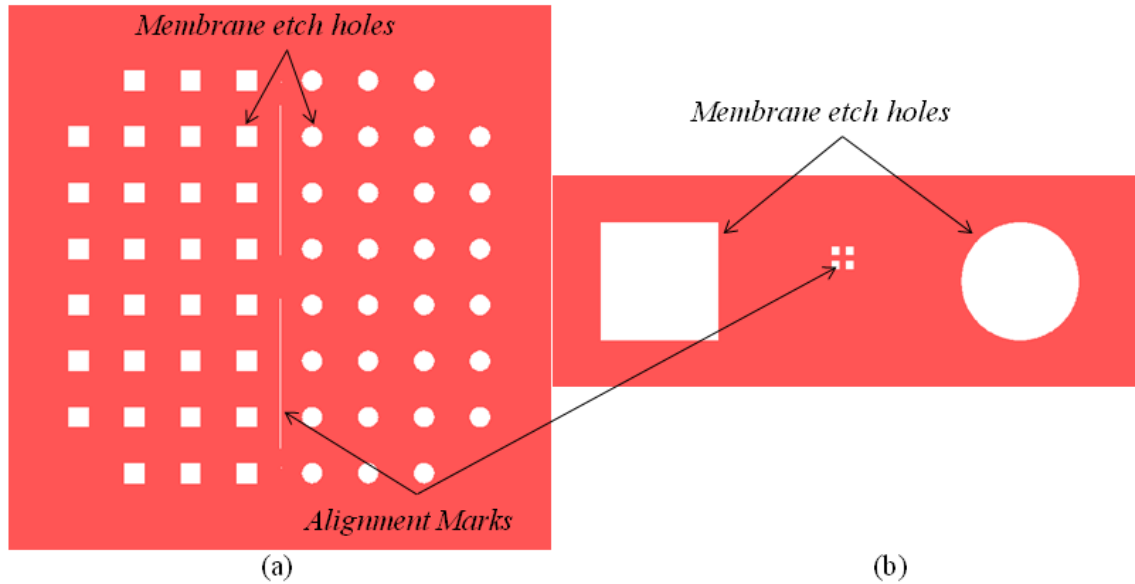


Figure 61. Membrane etch mask (a). Magnified view of the two separate membrane etch holes and alignment marks (b).

Finally, each mask is combined to fit on a single encompassing mask to conserve resources. The masks are exactly 1 inch square, used to align the front side to the backside of the sample pieces.

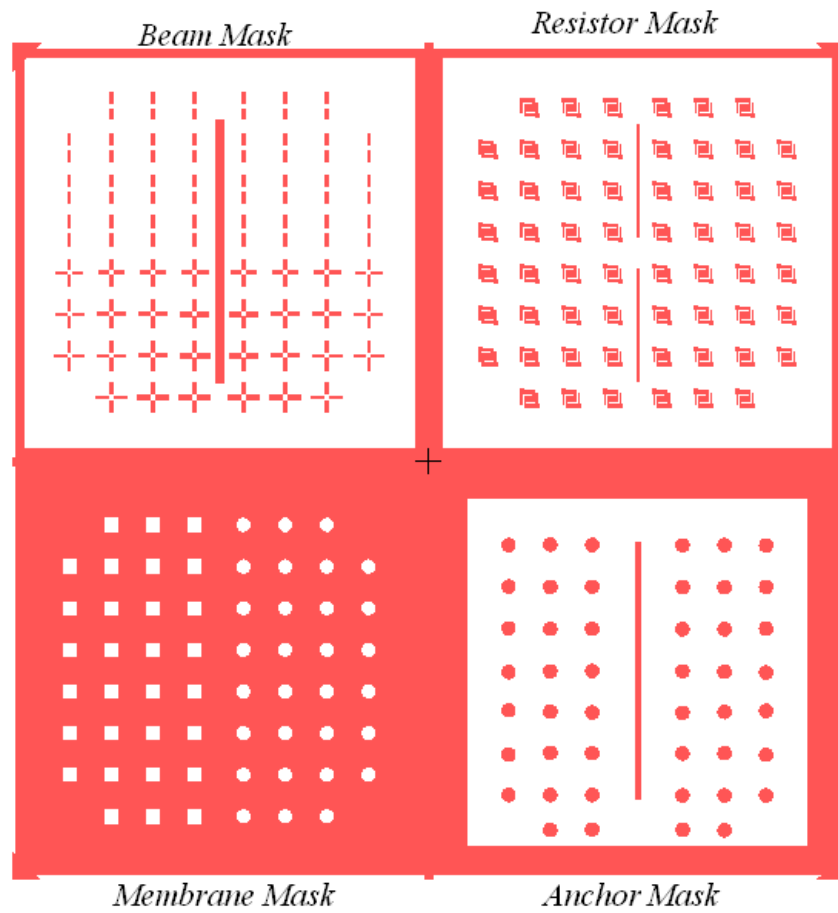


Figure 62. Complete mask.

Appendix C: Modal Analysis

This section contains further information concerning simulations. A modal analysis was simulated using the buckled membrane to understand the spring's resonant frequencies. Although research suggests that thermally actuating the membrane is slow (100Hz) compared to electrical switching speeds, future research efforts should consider the membrane's mode frequencies and mode shapes. The frequencies for the first four mode shapes are shown in Figure 63. The first mode occurs over 140 kHz, well over the predicted thermal switching speeds. The peaks displacement depends heavily on damping of the surrounding fluid. In this case, the pressure is assumed to be atmospheric, resulting in smoother peaks.

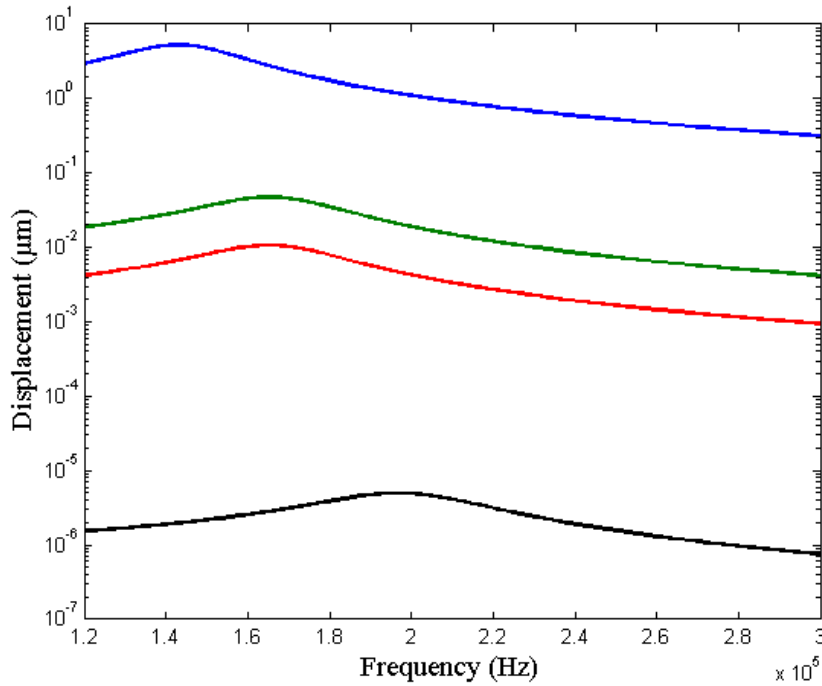


Figure 63. Membrane modal frequencies for the first four modes. Modes two and three are at the same frequency and represent the inverse of each other although their modal displacement is different.

Each of these modal frequencies corresponds to specific mode shapes which are shown next in Figure 64. Each mode corresponds to the modal frequencies listed in Figure 63. The blue line represents the first mode, the green and red lines indicate the second and third modes, and the black line indicates the last mode. Notice that the second two modes are mirrored images of each other and corresponds to the membrane having two simultaneous modes at a single frequency. Additionally, the displacements in the images are exaggerated to show the direction of modal displacement.

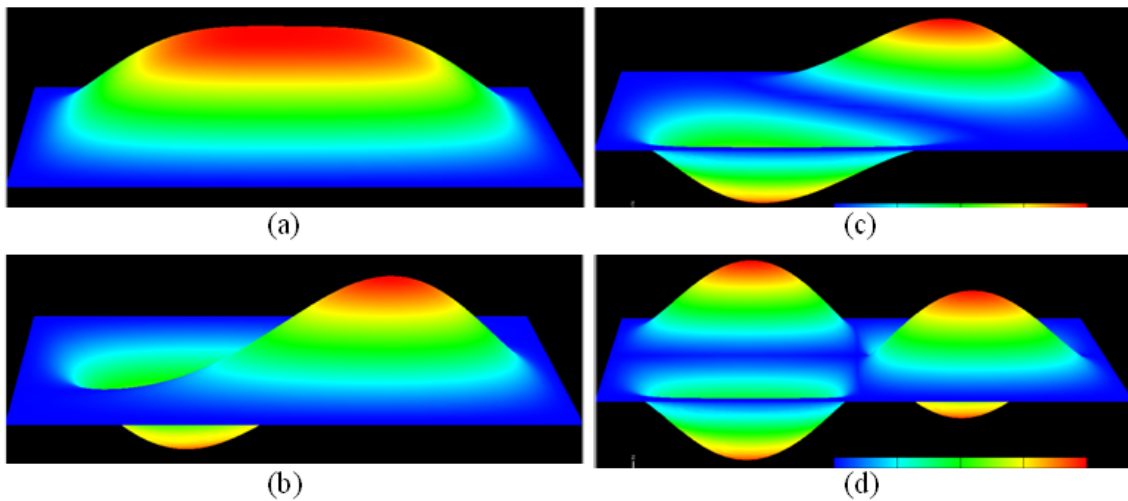


Figure 64. Mode shapes for the first four modes found using CoventorWare®.

Appendix D: Visual Bibliography

A visual bibliography is a useful tool for establishing a connection between references used in a research paper. Visual bibliographies can be organized by topic area, research groups, funding sources, or other relevant relationships. In this particular visual bibliography, we establish a connection between primary MEMS buckling authors. This allows us to see who is pursuing the most research in the area, and how other authors view his/her work.

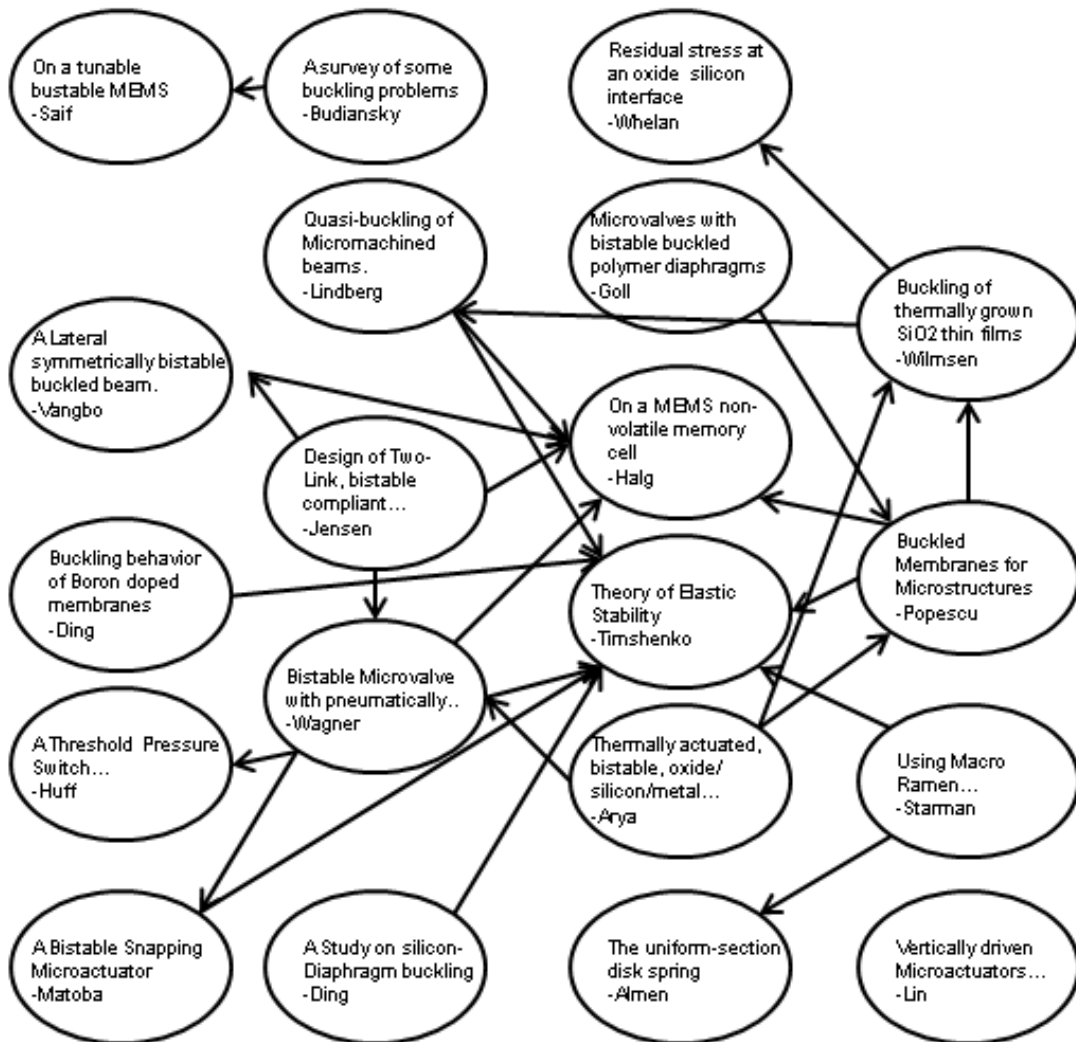


Figure 65. Visual bibliography. Articles are encircled with arrows indicating which authors cited each other.

Appendix E: Process Followers

This appendix contains the three process followers for the fabrication of the membrane, the resistors, and the cantilevers. The first process outlines the resistor fabrication.

Init.	Process Step	Notes	Date Time
	INSPECT SAMPLE: o Note any defects	<u>Start Date</u> <u>Start Time</u>	
	SETUP: o Start MJB3 to step 4 wait till suss power shows 275W o Start DUV system, needs 10 min to warm up.		
	SOLVENT CLEAN: o 20 sec acetone rinse o 20 sec methanol rinse o 20 sec isopropyl rinse o Dry with nitrogen at 500 rpm o Dry wafer with nitrogen on clean texwipes o 1 min 65°C hot plate bake o 1 min 95°C hot plate bake		
	APPLY SF11 o Dropper SF11 over sample o Ensure sample is completely covered to the edges o 4 sec 500 rpm o 30 sec 4000 rpm o 3 min 110°C hot plate bake		
	APPLY 1818 o Dropper 1818 over sample o Ensure sample is completely covered to the edges o 4 sec 500 rpm o 30 sec 4000 rpm o 3 min 110°C hot plate bake		
	EXPOSE 1818 o Finish setting up MJB3 o Clean Mask (ensure cap is on the spinner) o Put mask on the holder o Carefully raise stage to see height, adjust appropriately o Center sample within one inch window for alignment. Use the resistor mask. o 8 sec expose, may need longer depends on thickness. SU-8 manual lists the amount of energy necessary to fully expose.		
	DEVELOP o 45 sec spin at 500 rpm, spray with 351 (5/1 351/DI) developer. o 30 sec spin at 500 rpm and spray DI H ₂ O. o Rinse sample and dry with nitrogen.		
	EXPOSE SF11 o 200 sec flood expose, may need longer depends on thickness.		

	DEVELOP o Partially fill small container with SAL 101 developer. (enough to cover sample). o Submerge sample in developer for 1 minute. Slight agitation. o Rinse sample and dry with nitrogen.		
	EVAPORATE TI/AU o Need 500A of Ti and 3000A of Au deposited on top side of sample. o Follow backside etch process after evaporation and before release.		
	RELEASE o Fill beaker with ¼ inch of 1165 stripping agent. o 120°C heat on hot plate until liquid reaches 90°C, cover with foil. o 20 min sample soak in acetone. Slight agitation ok. NO ULTRASONIC, samples will break o Submerge sample in developer for 10 minutes. Slight agitation. o Rinse sample and dry with nitrogen.		
	Inspect resistors turned out as expected.	<u>Finish Date</u>	<u>Finish Time</u>

The next process follower is used to create the SU-8 beams.

Init	Process Step	Notes	Date Time
	INSPECT SAMPLE: o Note any defects	<u>Start Date</u>	<u>Start Time</u>
	SETUP: o Start MJB3 to step 4 wait till suss power shows 275W		
	SAMPLE PREPARATION: o 10 sec buffered oxide etch (BOE) use plastic dish and wear appropriate gloves o 3 min oxygen asher, remember to correct the RF reflectance.		
	SOLVENT CLEAN: o 20 sec acetone rinse o 20 sec methanol rinse o 20 sec isopropyl rinse o Dry with nitrogen at 500 rpm o Dry wafer with nitrogen on clean texwipes o 1 min 65°C hot plate bake o 1 min 95°C hot plate bake		
	APPLY 1818 o Dropper 1818 over sample o Ensure sample is completely covered to the edges o 4 sec 500 rpm o 30 sec 4000 rpm o 3 min 110°C hot plate bake		

	EXPOSE o Finish setting up MJB3 o Clean Mask (ensure cap is on the spinner) o Put mask on the holder o Carefully raise stage to see height, adjust appropriately o Center sample within one inch window for alignment. Use the anchor mask. o 8 sec expose, may need longer depends on thickness. SU-8 manual lists the amount of energy necessary to fully expose.		
	DEVELOP o 45 sec spin at 500 rpm, spray with 351 (5/1 351/DI) developer. o 30 sec spin at 500 rpm and spray DI H ₂ O. o Rinse sample and dry with nitrogen.		
	APPLY SU8 o Dropper SU8 over sample (do not let dropper touch edge of bottle) o Ensure sample is completely covered to the edges o 4 sec 500 rpm o 30 sec 2800 rpm gives 17microns approx (2000 rpm as backup) o Clean back of sample with acetone on a swab after sample finishes spinning o 3 min 65°C hot plate bake o 7 min 65°C hot plate bake o Inspect		
	EXPOSE o Align to marks below in 1818. They are difficult to see, but the center “landing strip” alignment marks help to get a good initial alignment. o 23 sec expose, may need longer depends on thickness. SU-8 manual lists the amount of energy necessary to fully expose. o 1 min 65°C hot plate bake o 3 min 95°C hot plate bake		
	DEVELOP o Partially fill small container with SU-8 developer. (enough to cover sample). o Submerge sample in developer for 4 minutes. Slight agitation. o Rinse sample and dry with nitrogen.		
	HARD BAKE o 3 min 65°C hot plate bake o 30 min 110°C hot plate bake		
	Inspect beams to ensure release from sacrificial photoresist. May need time in an acetone bath to finish releasing. Ensure beams are not warped and they are adhered to the surface of SOI.	Finish Date Finish Time	

The final process follower illustrates the process for fabricating the membrane.

Init	Process Step	Notes	Date Time
	INSPECT SAMPLE: o Note any defects	Start Date Start Time	
	SETUP: o Start MJB3 to step 4 wait till suss power shows 275W		

<p>SOLVENT CLEAN:</p> <ul style="list-style-type: none"> o 20 sec acetone rinse o 20 sec methanol rinse o 20 sec isopropyl rinse o Dry with nitrogen at 500 rpm o Dry wafer with nitrogen on clean texwipes o 1 min 65°C hot plate bake o 1 min 95°C hot plate bake 		
<p>Apply SU8</p> <ul style="list-style-type: none"> o Dropper SU8 over sample (do not let dropper touch edge of bottle) o Ensure sample is completely covered to the edges o 4 sec 500 rpm o 30 sec 2800 rpm gives 17microns approx (2000 rpm as backup) o Clean back of sample with acetone on a swab after sample finishes spinning o 3 min 65°C hot plate bake o 7 min 65°C hot plate bake o Inspect 		
<p>Expose</p> <ul style="list-style-type: none"> o Finish setting up MJB3 o Clean Mask (ensure cap is on the spinner) o Put mask on the holder o Carefully raise stage to see height, adjust appropriately o 23 sec expose, may need longer depends on thickness. SU-8 manual lists the amount of energy necessary to fully expose. o 1 min 65°C hot plate bake o 3 min 95°C hot plate bake 		
<p>Develop</p> <ul style="list-style-type: none"> o Partially fill small container with SU-8 developer. (enough to cover sample). o Submerge sample in developer for 4 minutes. Slight agitation. o Rinse sample and dry with nitrogen. 		
<p>Develop</p> <ul style="list-style-type: none"> o 3 min 65°C hot plate bake o 30 min 110°C hot plate bake 		
<p>Inspect finished etch holes under optical microscope.</p>	<p><u>Finish Date</u></p> <p><u>Finish Time</u></p>	

References

- [1] K. B. Lee, *Principles of Microelectromechanical Systems*, Hoboken, NJ: John Wiley & Sons, Inc. , 2011.
- [2] L. Robin, "I-Micronews," July 2013. [Online]. Available: http://www.i-micronews.com/upload/pdf/mems_juillet2013_AC.pdf. [Accessed 16 October 2013].
- [3] P. Clarke, "EE Times," UBM Tech, 7 July 2012. [Online]. Available: <http://www.eetimes.com>. [Accessed 16 October 2013].
- [4] "I-Micronews," Yole Development, 2013. [Online]. Available: <http://www.i-micronews.com>. [Accessed 16 October 2013].
- [5] L. A. Starman and R. A. Coutu, "Using Micro-Raman Spectroscopy to Assess MEMS Si/SiO₂ Membranes Exhibiting Negative Spring Constant Behavior," in *Experimental Mechanics*, 2012.
- [6] M. Handtmann, R. Aigner, A. Meckes and G. K. M. Wachutka, "Sensitivity Enhancement of MEMS Inertial Sensors Using Negative Springs and Active Control," *Sensors and Actuators*, Vols. 97-98, pp. 153-160, 2002.
- [7] K. Y. Park, C. W. Lee, H. S. Jang, Y. S. Oh and B. J. Ha, "Capacitive Sensing Type Surface Micromachined Silicon Accelerometer with a Stiffness Tuning Capability," in *Micro Electro Mechanical Systems*, 1998.
- [8] M. M. Z. Shahadat, T. Mizuno, Y. Ishino and M. Takasaki, "Active Horizontal Suspension System Using Negative Stiffness Control," in *Control Automation and Systems*, 2010.
- [9] J. Qiu, J. H. Lang and A. H. Slocum, "A Curved-Beam Bistable Mechanism," *Journal of Microelectromechanical Systems*, vol. 13, no. 2, pp. 137-145, 2004.
- [10] J. O. Almen and A. Laszlo, "The Uniform-Section Disk Spring," *The American Society of Mechanical Engineers*, vol. 58, pp. 305-314, 1936.
- [11] M. T. A. Saif, "On a Tunable Bistable MEMS-Theory and Experiment," *Journal of Microelectromechanical Systems*, vol. 9, no. 2, pp. 157-170, 2000.
- [12] J. P. McKelvey, *Solid State Physics*, Malabar: Krieger Publishing Company, 1993.

- [13] G. S. May and S. M. Sze, *Fundamentals of Semiconductor Fabrication*, Hoboken: John Wiley & Sons, 2004.
- [14] J. Bardeen and W. H. Brattain, "The Transistor, A Semi-Conductor Triode," *Physical Review*, vol. 74, pp. 230-231, 1948.
- [15] C. T. Leondes, *MEMS / NEMS Handbook Techniques and Applications*, New York City: Springer , 2006.
- [16] K. E. Peterson, "Silicon as a Mechanical Material," *Proceedings of the IEEE*, vol. 70, no. 5, pp. 420-457, 1982.
- [17] W. P. Eaton and J. H. Smith, "Micromachined Pressure Sensors; Review and Recent Developments," *Smart Mater*, vol. 6, no. 5, pp. 530-539, 1997.
- [18] L.-S. Fan, Y.-C. Tai and R. S. Muller, "Integrated Movable Micromechanical Structures for Sensors and Actuators," *IEEE Transactions on Electron Devices*, vol. 35, no. 6, pp. 724-730, 1988.
- [19] M. Mehregany, K. J. Gabriel and W. S. N. Trimmer, "Integrated Fabrication of Polysilicon Mechanisms," *IEEE Transactions on Electron Devices*, vol. 35, no. 6, pp. 719-723, 1988.
- [20] K. Pister, M. W. Judy and e. al., "Microfabricated Hinges," *Sensors and Actuators A*, vol. 33, pp. 249-256, 1992.
- [21] L. S. Fan, Y. C. Tai and R. S. Muller, "IC-Processed Electrostatic Micromotors," *Sensors and Actuators* , vol. 20, pp. 41-47, 1989.
- [22] G. M. Rebeiz and J. B. Muldavin, "RF MEMS Switches and Switch Circuits," *IEEE Microwave Magazine*, pp. 59-71, December 2001.
- [23] P. Bergstrom, T. Tamagawa and Polla, "Design and Fabrication of Micromechanical Logic Elements," in *Micro Electro Mechanical Systems*, Napa Valley, 1990.
- [24] O. Cugat, J. Delamare and G. Reyne, "Magnetic Micro-Actuators and Systems (MAGMAS)," *IEEE Transactions on Magnetics*, vol. 39, no. 5, pp. 3607-3612, 2003.
- [25] W. C. Tang, T.-C. H. Nguyen and R. T. Howe, "Laterally Driven Polysilicon Resonant Microstructures," *Sensors and Actuators*, vol. 20, pp. 25-32, 1989.
- [26] L. Que, J.-S. Park and Y. B. Gianchandani, "Bent-Beam Electrothermal Actuators--Part I: Single Beam and Cascaded Devices," *Journal of Microelectromechanical*

- Systems*, vol. 10, no. 2, pp. 247-254, 2001.
- [27] L. Lin and S.-H. Lin, "Vertically Driven Microactuators by Electrothermal Buckling Effects," *Sensors and Actuators A*, vol. 71, pp. 35-39, 1998.
- [28] S. Franssila, Introduction to Micro Fabrication, West Sussex: John Wiley & Sons Ltd, 2004.
- [29] S. M. Spearing, "Materials Issues in Microelectromechanical Systems (MEMS)," *Acta Materialia*, vol. 48, pp. 179-196, 2000.
- [30] J. M. Bustillo, R. T. Howe and R. S. Muller, "Surface Micromachining for Microelectromechanical Systems," *Proceedings of the IEEE*, vol. 86, no. 8, pp. 1552-1574, 1998.
- [31] G. T. A. Kovacs, N. I. Maluf and K. E. Peterson, "Bulk Micromachining of Silicon," *Proceedings of the IEEE*, vol. 86, no. 8, pp. 1536-1551, 1998.
- [32] H. V. Jansen, M. J. De Boer, S. Unnikrishnan, M. C. Louwerse and M. C. Elwenspoek, "Black Silicon Method X: A Review on High Speed and Selective Plasma Etching of Silicon with Profile Control: An In-depth Comparison between Bosch and Cryostat DRIE processes as a Roadmap to Next Generation Equipment," *Journal of Micromechanics and Microengineering*, vol. 19, pp. 1-42, 2009.
- [33] R. L. Mott, Applied Strength of Materials, Englewood Cliffs, New Jersey: Prentice-Hall Inc., 1996.
- [34] G. Kaltsas, A. Nassiopoulou, M. Siakavellas and E. Anastassakis, "Stress Effect on Suspended Polycrystalline Silicon Membranes Fabricated by Micromachining of Porous Silicon," *Sensors and Actuators*, vol. 68, no. 1-3, pp. 429-434, 1998.
- [35] T. Iida, T. Itoh, D. Noguchi and Y. Takano, "Residual Lattice Strain in Thin Silicon-On-Insulator Bonded Wafers: Thermal Behavior and Formation Mechanisms," *Journal of Applied Physics*, vol. 87, no. 2, pp. 675-681, 2000.
- [36] M. F. Doerner and W. D. Nix, "Stresses and Deformation Processes in Thin Films on Substrates," *Critical Reviews in Solid State and Materials Sciences*, vol. 268, no. 3, p. 225, 1988.
- [37] I. De Wolf, "Micro-Raman Spectroscopy to Study Local Mechanical Stress in Silicon Integrated Circuits," *Semiconductor Sci and Technol*, vol. 11, pp. 139-154, 1995.

- [38] S. R. Best, "Detection of Residual Stress in Multi-Crystalline Silicon Wafers Using Swept-Sine Frequency Response Data," Ph.D Dissertation, University of South Florida, Tampa, Florida, 2005.
- [39] Ultrasil Corporation , "Ultrasil," 2013. [Online]. Available: <http://www.ultrasil.com/>. [Accessed 4 September 2013].
- [40] R. T. Howe, B. E. Boser and A. P. Pisano, "Polysilicon Integrated Microsystems: Technologies and Applications," *Sensors and Actuators A: Physical*, vol. 56, no. 1-2, pp. 167-177, 1996.
- [41] C. W. Wilmsen, E. G. Thompson and G. H. Meissner, "Buckling of Thermally-Grown SiO₂ Thin Films," *IEEE Transactions on Electron Devices*, vol. 19, no. 1, p. 122, 1972.
- [42] P. Schwartz, "Wikipedia," 19 May 2005. [Online]. Available: <http://en.wikipedia.org/wiki/Buckling>. [Accessed 4 September 2013].
- [43] M. J. N. Priestley, *Seismic Design and Retrofit of Bridges*, John Wiley & Sons, 1996.
- [44] S. Park and D. Hah, "Pre-shaped Buckled-beam Actuators: Theory and Experiment," *Sensors and Actuators A*, vol. 148, pp. 186-192, 2008.
- [45] D. S. Popescu, S. J. Lammerink and M. Elwenspoek, "Buckled Membranes for Microstructures," in *IEEE Workshop on Micro Electro Mechanical Systems*, Oiso, 1994.
- [46] D. O. Brush and B. O. Almroth, *Buckling of Bars, Plates, and Shells*, McGraw-Hill inc, 1975.
- [47] X. Ding, W. H. Ko, Y. Niu and W. He, "A Study on Silicon-Diaphragm Buckling," in *Solid-State Sensors and Actuator Workshop*, Hilton Head Island, 1990.
- [48] M. A. Huff, A. D. Nikolich and M. A. Schmidt, "A Threshold Pressure Switch Utilizing Plastic Deformation of Silicon," in *Solid-State Sensors and Actuators*, San Francisco, 1991.
- [49] B. Budiansky and J. W. Hutchinson, "A Survey of Some Buckling Problems," *AIAA Journal*, vol. 4, no. 9, pp. 1505-1510, 1966.
- [50] W. Fang and J. A. Wickert, "Post Buckling of Micromachined Beams," *Journal of Micromechanics and Microengineering*, vol. 4, pp. 116-122, 1994.

- [51] Wyzant Resources, "Solid of Revolution-Finding Volume by Rotation," WyzAnt Tutoring , 2014. [Online]. Available: <http://www.wyzant.com>. [Accessed 23 January 2014].
- [52] S. P. Timoshenko and J. M. Gere, Theory of Elastic Stability, New York: McGraw-Hill, 1961.
- [53] B. D. Jensen, L. L. Howell and L. G. Salmon, "Design of Two-Link, In-Plane, Bistable Compliant Micro-Mechanisms," *Journal of Mechanical Design*, vol. 121, pp. 416-423, 1999.
- [54] I. G. Faoulds, R. W. Johnstone and M. Parameswaran, "A Pulse Width Modulation Controlled Bistable Microelectromechanical System," in *Canadian Conference on Electrical and Computer Engineering*, Saskatoon, 2005.
- [55] B. Hälg, "On a Micro-Electro-Mechanical Nonvolatile Memory Cell," in *IEEE Transactions on Electronic Devices*, 1990.
- [56] M. Vangbo and Y. Bäcklund, "A Lateral Symmetrically Bistable Buckled Beam," *Journal of Micromechanics and Microengineering*, vol. 8, no. 1, pp. 29-32, 1998.
- [57] H. Matoba, T. Ishikawa, C.-J. Kim and R. S. Muller, "A Bistable Snapping Microactuator," in *IEEE Workshop on Micro Electro Mechanical Systems*, Oiso, 1994.
- [58] G. Goll, W. Bacher, B. Bustgens and e. al., "Microvalves with Bistable Buckled Polymer Diaphragms," *Journal of Micromechanics and Microengineering*, vol. 6, pp. 77-79, 1996.
- [59] B. Wagner, H. J. Quenzer, T. Hoerschelmann, T. Lisec and M. Juerss, "Bistable Microvalve with Pneumatically coupled Membranes," in *Micro Electro Mechanical Systems*, San Diego, 1996.
- [60] B. Wagner, H. J. Quenzer, S. Hoerschelmann, T. Lisec and M. Juerss, "Micromachined Bistable Valves for Implantable Drug Delivery Systems," in *IEEE Engineering in Medicine and Biology Society*, Amsterdam, 1996.
- [61] Y. C. Wang and R. S. Lakes, "Extreme Stiffness systems due to negative stiffness elements," *American Journal of Physics*, vol. 72, no. 1, pp. 40-50, 2004.
- [62] J. E. Shigley and C. R. Mischke, Mechanical Engineering Design, McGraw-Hill, 1989.

- [63] R. W. Siorek, "Suspension Control Valve Using Cones SpringsDisk". United States of America Patent 4,325,468, 20 April 1982.
- [64] S. M. Lepi, Practical Guide to Finite Elements, New York: Marcel Dekker, 1998.
- [65] CoventorWare, "CoventorWare Analyzer Reverence," Coventor®, Inc., Cary, NC, 2010.
- [66] W. S. Janna, Engineering Heat Transfer, Boca Raton: CRC Press, 2009.
- [67] S. Bouwstra, P. Kemna and P. Legtenberg, "Thermal Excited Resonating Membrane Mass Flow Sensor," *Sensors and Actuators*, vol. 20, pp. 213-223, 1989.
- [68] M. Chiao and L. Lin, "Self-Buckling of Micromachined Beams Under Resistive Heating," *Journal of Microelectromechanical Systems*, vol. 9, no. 1, pp. 146-151, 2000.
- [69] R. A. Coutu and S. A. Ostrow, "Microelectromechanical Systems Resistive Heaters as Circuit Protection Devices," *IEEE Trans. Compon. Packag. Technol*, vol. 3, no. 12, pp. 2174-2179, 2013.
- [70] M. Pecht, handbook of Electronic Package Design, Boca Raton, FL: CRC Press, 1991.
- [71] M. Hoffmann, P. Kopka and E. Voges, "Bistable Micromechanical Fiber-Optic Switches on Silicon with Thermal Actuators," *Sensors and Actuators*, vol. 78, pp. 28-35, 1999.
- [72] A. Freidberger, P. Kreisl and e. al., "Micromechanical Fabrication of Robust, Low-Power Metal-Oxide Gas Sensors," *Sensors and Actuators B*, vol. 93, pp. 345-349, 2003.
- [73] K.-N. Lee, D.-S. Lee and e. al., "A High-Temperature MEMS Heater Using Suspended Silicon Structures," *Journal of Micromechanics and Microengineering*, vol. 19, pp. 1-8, 2009.
- [74] H. Lorenz, M. Laudon and P. Renaud, "Mechanical Characterization of a New High-Aspect-Ratio Near UV-Photoresist," *Microelectronic Engineering*, vol. 41, pp. 371-374, 1998.
- [75] H. Lorenz, M. Despont, N. Fahrni, N. LaBianca, P. Renaud and P. Vettiger, "SU-8: A Low-Cost Negative Resist for MEMS," *Journal of Micromechanics and*

Microengineering, vol. 7, pp. 121-124, 1997.

- [76] E. H. Conradie and D. F. Moore, "SU-8 Thick Photoresist Processing as a Functional Material for MEMS Applications," *Journal of Micromechanics and Microengineering*, vol. 12, pp. 368-374, 2002.
- [77] B. F. Toler, *Novel Test Fixture for Characterizing Microcontacts: Performance and Reliability*, Wright-Patterson Air Force Base, 2013.
- [78] Zygo, "3D Optical Surface Profilers," Zygo®, [Online]. Available: <http://www.zygo.com/?/met/profilers/>. [Accessed 4 November 2013].
- [79] J. Siegel, O. Lyutakov and e. al., "Properties of Gold Nanostructures Sputtered on Glass," *Nanoscale Research Letters*, vol. 6, 2011.
- [80] M. Zhang, Y. Efremov and e. al., "Size-Dependent Melting Point Depression of Nanostructures: Nanocalorimetric Measurements," *Physical Review B*, vol. 62, no. 15, pp. 549-557, 2000.
- [81] J. McMahon, "MRO Today," Minusk, [Online]. Available: <http://www.minusk.com/content>. [Accessed 3 February 2014].
- [82] J. Winterflood, T. Barber and D. Blair, "Using Euler Buckling Springs for Vibration Isolation," in *Classical and Quantum Gravity*, 2002.
- [83] R. Arya, M. M. Rashid, D. Howard and e. al., "Thermally Actuated, Bistable, Oxide/Silicon/Metal Membranes," *Journal of Micromechanics and Microengineering*, vol. 16, pp. 40-47, 2006.
- [84] J. O. Almen and A. Laszlo, "The Uniform-Section Disk Spring," *The American Society of Mechanical Engineers*, vol. 58, pp. 305-314, 1936.

REPORT DOCUMENTATION PAGE				<i>Form Approved</i> OMB No. 074-0188	
<p>The public reporting burden for this collection of information is estimated to average 1 hour per response, including the time for reviewing instructions, searching existing data sources, gathering and maintaining the data needed, and completing and reviewing the collection of information. Send comments regarding this burden estimate or any other aspect of the collection of information, including suggestions for reducing this burden to Department of Defense, Washington Headquarters Services, Directorate for Information Operations and Reports (0704-0188), 1215 Jefferson Davis Highway, Suite 1204, Arlington, VA 22202-4302. Respondents should be aware that notwithstanding any other provision of law, no person shall be subject to any penalty for failing to comply with a collection of information if it does not display a currently valid OMB control number.</p> <p>PLEASE DO NOT RETURN YOUR FORM TO THE ABOVE ADDRESS.</p>					
1. REPORT DATE (DD-MM-YYYY) 28-Mar-2014		2. REPORT TYPE Master's Thesis		3. DATES COVERED (From - To) Sept 2012 - March 2014	
4. TITLE AND SUBTITLE Selectively Tuning a Buckled Si/SiO ₂ Membrane MEMS through Joule Heating Actuation and Mechanical Restriction				5a. CONTRACT NUMBER	
				5b. GRANT NUMBER	
				5c. PROGRAM ELEMENT NUMBER	
6. AUTHOR(S) Ziegler, Kyle K, 2nd Lt, USAF				5d. PROJECT NUMBER	
				5e. TASK NUMBER	
				5f. WORK UNIT NUMBER	
7. PERFORMING ORGANIZATION NAMES(S) AND ADDRESS(S) Air Force Institute of Technology Graduate School of Engineering and Management (AFIT/EN) 2950 Hobson Way, Building 640 WPAFB OH 45433				8. PERFORMING ORGANIZATION REPORT NUMBER AFIT-ENG-14M-88	
9. SPONSORING/MONITORING AGENCY NAME(S) AND ADDRESS(ES) "Intentionally Left Blank"				10. SPONSOR/MONITOR'S ACRONYM(S)	
				11. SPONSOR/MONITOR'S REPORT NUMBER(S)	
12. DISTRIBUTION/AVAILABILITY STATEMENT Distribution Statement A. Approved for Public Release; Distribution Unlimited					
13. SUPPLEMENTARY NOTES This work is declared a work of the U.S. Government and is not subject to copyright protection in the United States.					
14. ABSTRACT This research followed previous work and attempted to modify the spring in two ways. First, a Ti/Au meander resistor was deposited atop the membrane in an effort to actuate the membrane and change the spring constant. Secondly, a series of overhanging cantilevers were attached to the bulk substrate surrounding the membrane in an effort to constrain the membrane buckling deflection to the negative stiffness region. Membrane buckling was investigated through Finite Element analysis (FEA) and analytical equations. Deflections were measured using an interferometric microscope (IFM) and force/deflection measurements were captured using a unique measurement scheme. The results concluded that by introducing a thermal stress, the membrane could be actuated with a corresponding 3x increase in spring constant. Additionally, the overhanging beams restricted the membrane deflection by up to 30%, but, because of a lack in beam stiffness, failed to restrict the membrane to the negative stiffness region. This research laid the ground work for future work in this area.					
15. SUBJECT TERMS 4-5 Keywords/phrases					
16. SECURITY CLASSIFICATION OF:			17. LIMITATION OF ABSTRACT UU	18. NUMBER OF PAGES 143	19a. NAME OF RESPONSIBLE PERSON Dr. Ronald A. Coutu, Jr., PhD
a. REPORT U	b. ABSTRACT U	c. THIS PAGE U			19b. TELEPHONE NUMBER (Include area code) (937) 255-3636, x 7230 (Ronald.coutu@afit.edu)